WHOLE BODY AND UPPER EXTREMITY ULTRA-HIGH FIELD MAGNETIC RESONANCE IMAGING: COIL DEVELOPMENT AND CLINICAL IMPLEMENTATION

by

Shailesh B. Raval

B.E., North Gujarat University, 2006

M.S., Worcester Polytechnic Institute, 2009

Submitted to the Graduate Faculty of

Swanson School of Engineering in partial fulfillment

of the requirements for the degree of

Doctor of Philosophy

University of Pittsburgh

2017

UNIVERSITY OF PITTSBURGH

SWANSON SCHOOL OF ENGINEERING

This dissertation was presented

by

Shailesh B. Raval

It was defended on

July 11th 2017

and approved by

Vijay S. Gorantla, M. D., Ph. D. Associate Professor, Department of Plastic Surgery

George D. Stetten, M.D., Ph.D., Professor, Department of Bioengineering

Howard J. Aizenstein, M.D., Ph.D., Professor, Departments of Psychiatry and Bioengineering

Dissertation Director: Tamer S. Ibrahim, Ph.D., Associate Professor, Departments of Bioengineering and Radiology

WHOLE BODY AND UPPER EXTREMITY ULTRA-HIGH FIELD MAGNETIC RESONANCE IMAGING: COIL DEVELOPMENT AND CLINICAL IMPLEMENTATION

Shailesh B. Raval, Ph.D.

University of Pittsburgh, 2017

Since Magnetic Resonance Imaging (MRI)'s introduction into the clinical imaging application arena, MRI has become one of the most promising non-invasive methods for evaluating and identifying body organs in normal and diseased conditions. In the last two decades, a few research groups have been working on addressing the challenges to Ultra-High Field (UHF) imaging (≥ 7 Tesla), such as magnetic field inhomogeneities and elevated Radiofrequency (RF) power absorption through technological developments. In recent years, imaging at 7 Tesla has shown an inherent ability to improve scan time and anatomical resolution.

To address the current challenges associated with UHF imaging, this thesis presents the development of innovative whole body and extremity RF coil systems for 7 Tesla imaging. For body imaging, the transmit (Tx) coil is based on the innovative Tic-Tac-Toe (TTT) design, which possesses a load insensitive characteristic in terms of magnetic and electric field distributions. 7 Tesla homogenous whole-body in-vivo imaging with and without a receive (Rx) only insert array is demonstrated showing excellent anatomical detail.

As a part of upper extremity imaging, we have developed a transverse electromagnetic (TEM) coil as a transmitter in conjunction with an eight channel receive only insert for 7 Tesla hand/forearm imaging. We have acquired a wide variety of different sequences and used post-

processing methods to extract specific anatomy from high resolution scans (i.e. nerve and vessels), which in turn has helped in exploring new clinical applications, such as arm transplantation, and has added knowledge to existing ones.

The developed RF coil systems and methodologies not only enhance the fundamental scientific knowledge of RF coil design approaches at high frequencies but they also add to the realm of clinical applications of UHF human imaging.

TABLE OF CONTENTS

LIST OF TABLES

LIST OF FIGURES

1.0 INTRODUCTION TO DISSERTATION

1.1 ULTRA-HIGH FIELD MRI

Since the advent of the use of Magnetic Resonance Imaging (MRI), there has been a constant push in the scientific community to develop and evaluate the diagnostic capabilities of higher field strengths [1-4]. Early ultrahigh field (UHF) developmental systems for human imaging include 8 tesla (T) at the Ohio State University in 1997 [5] and 7T at the University of Minnesota in 2000 [6], and each of these systems provided the opportunity for scientists and engineers to develop MR hardware and supplemental technologies. As 7T human imaging is currently on the cusp of clinical applications [7], there is an even greater push towards technological development as well as clinical application [8, 9].

MRI is a favored technique to evaluate soft tissues in various body organs in normal and diseased conditions [10, 11]. However, UHF MRI presents some challenges, such as like B_1^+ inhomogeneities, RF power absorption, and technological developments. In the last two decades, a few research groups (4T-9.4T) have been working on addressing the UHF imaging challenges [6, 12], ultimately discovering that UHF MRI could provide anatomical, functional and physiological information beyond just gains in higher resolution image quality (Signal-to-noise or SNR) [6]. In recent years, human head [6], prostate [13], cardiac [14], spine [15], kidney [16],

liver [17] and knee imaging [18] have been conducted by a handful of research groups at 7T and have demonstrated good potential in terms of technological development as well as addressing the clinical demands of identifying body organs in normal and diseased conditions. In addition, various clinical imaging procedures at 7T employ T1 or T2 weighted imaging with the fat suppression method and/or breath-hold techniques (application specific repetition time (TR) and echo time (TE)). This aids in improving the performance [13, 17, 19] of imaging on abdominal organs like the pancreas, kidney, liver and bile duct in terms of important parameters like scan time and motion artifacts.

Until now, all major research efforts into UHF imaging have been focused on imaging the brain [20-22], somewhat successfully compared to imaging of the human torso/body and extremities (except the knee) [18, 23, 24]. As efforts to use UHF imaging for abdominal imaging haven't been that successful yet, there lies a tremendous need for attention to UHF imaging of the body (kidney, liver, pancreatic) and extremity conditions [12]. Accordingly the goal of this dissertation is to develop a whole body and extremity radiofrequency (RF) system for ultra-high field (UHF) human magnetic resonance imaging (MRI). For body imaging, the transmit (Tx) coil will be based on the innovative tic-tac-toe (TTT) design [20, 25-27], which possesses a load insensitive characteristic in terms of magnetic and electric field distributions. The Tx coil will work in conjunction with a high density receive (Rx) only array that will boost SNR/CNR, increase spatial resolution and/or reduce scanning time. For the upper extremity imaging, we will develop a transverse electromagnetic (TEM) coil as a transmitter in conjunction with an eight channel Rx only insert for hand/forearm imaging. We will focus on optimizing the different sequences, not just the typical T1 and T2 weighted imaging protocols, using post-processing methods to extract

the specific anatomy from high resolution scans (i.e. nerve and vessels), which will help in exploring new clinical applications and adding knowledge to existing ones.

Due to its intricate electromagnetic field behavior at an ultra-high field, 7T MRI is still an investigational/research-only device. Our successful completion of the above mentioned goal (a successful whole body and upper extremity imaging systems) will expand the technological boundaries of UHF imaging. With acceptable SAR values and homogeneous B_1^+ fields, we will have a technology that can be used to detect finer anatomical details, early stage tumors and diseased conditions in the abdomen (e.g., first and second order distal arteries (compare to lower field strength)), cyst and solid tumors, non-contrast enhanced renal MR angiography, distal renal artery stenosis, and, in cases of extremity applications, various conditions like post-transplant evaluation, dystrophic lesions, hamartomas and rare neoplastic lesions, along with a variety of other pathological conditions [28]. Such a new system will not only enhance the fundamental scientific knowledge of an RF coil design approach at high frequency but will also add to the realm of clinical applications of UHF body and extremity imaging.

1.2 DISSERTATION OUTLINE

Chapter 1 presents the introduction and thesis outline. Chapter 2 outlines the challenges in using Ultra-high field MRI and motivations for developing it, the use of RF coils at UHF, the finite difference time domain (FDTD) method and the human model (simulation model).

Chapter 3 discusses the detailed in-vivo imaging of the whole body using a thirty-two channel Tx only coil with a sixteen channel receive only 7T body coil. First, it describes the detailed development of the numerical modelling and experimental coil design. Then it presents results of the benchtop evaluation of Scattering (S) parameters in simulation as well as experimentally. Next, a characterization of an RF, including noise correlation, acceleration factor, and SNR with and without a receive only array, are presented. Chapter 3 also details the coil performance established by B_1^+ mapping in simulation using the FDTD method as well as experimentally on a 7T MRI scanner. The phantom as well as in-vivo data are presented using a 7T Siemens Magnetom scanner.

Chapter 4 describes the development of a UHF RF coil for evaluating Upper Extremity Imaging applications. This Upper Extremity RF Coil is composed of a transverse electromagnetic transmit (TEM) coil and an eight channel receive-only array developed for 7T MR applications. This chapter lists the characterization of the RF coil system on bench measurements like scattering parameters evaluation and decoupling measurements. Coil performance using B_1^+ mapping is presented numerically as well as experimentally. Results of finite difference time domain simulations to evaluate the B_1^+ field distribution and SAR for the forearm region of the upper extremity are presented, as well as a comparison of the High Resolution 7T images 3T images.

Chapter 5 details the findings of a clinical feasibility study of the 7T upper extremity RF coil system, in which a wide range of sequences, including a T1 weighted (T1W) volumetric interpolate breath-hold exam (VIBE), T2 weighted (T2W) double-echo steady state (DESS), susceptibility weighted imaging (SWI), time-of-flight (TOF), diffusion tensor imaging (DTI), and

diffusion spectrum imaging (DSI), were optimized and incorporated using a radiofrequency (RF) transmit and receive only system for the 7T upper extremity (UE) imaging. In addition, results from a comparison of Siemen's optimized protocol/sequences on a 3T scanner and those at 7T are presented. DSI studio was utilized to analyze diffusion-weighted derived fractional anisotropy images to identify nerves. MIPAV (Medical Image Processing, Analysis, and Visualization) was used to extract the forearm vasculature.

Chapter 6 summarizes the findings and the significance of the work done in this dissertation. It also outlines the ongoing as well as future work direction.

1.3 COMPLETE LIST OF PUBLICATION

1.3.1 Peer-Reviewed Journal Proceedings

S. B. Raval, T. Zhao, N. Krishnamurthy, V. S. Gorantla, T. S. Ibrahim (2016), "Ultrahigh field radio frequency system for upper extremity imaging applications", NMR in Biomedicine 2016. 29: 1768-1779. Doi: 10.1002/nbm.3582.

S. B. Raval, C. Britton, T. Zhao, V. S. Gorantla, T. S. Ibrahim, "Ultra-high field upper extremity peripheral nerve and non-contrast enhanced vascular imaging." PLoS ONE 12(6): e0175629. https://doi.org/10.1371/journal.pone.0175629.

Y. Zhao, T. Zhao, **S. B. Raval.**, N. Krishnamurthy , H. Zheng, C. T. Harris, W. B. Handler, B. A. Chronik, T. S. Ibrahim (2015), "Dual optimization method of radiofrequency and quasistatic field simulations for reduction of eddy currents generated on 7T radiofrequency coil shielding." Magnetic Resonance in Medicine, 74: 1461 – 1469. Doi: 10.1002/mrm.25424.

1.3.2 Peer-Reviewed International Conferences Proceedings: * Oral Invited Presentations

***S. B. Raval**, T. Santini, S. Wood, N. Krishnamurthy, T. Zhao, T.S. Ibrahim, "In-Vivo (8x4) 32-Ch Tx-Only Body Array for UHF MRI, " Oral presentation in Proc. of The 23th International Society of Magnetic Resonance in Medicine Annual Meeting, Honolulu, Hawaii, April 2017.

***S. B. Raval,** T. Zhao, N. Krishnamurthy, T. S. Ibrahim, V. S. Gorantla, "Non-Contrast Enhanced 7 Tesla MR Imaging for Non-Invasive Monitoring of Chronic Rejection in Reconstructive Transplantation", in Proc. Of the 5th American Society for Reconstructive Transplantation, Chicago, Nov-2016.

***S. B. Raval,** T. Zhao, N. Krishnamurthy, T. S. Ibrahim, V. S. Gorantla, "Ultra-high Resolution Non-Contrast Vascular and Nerve Imaging for Graft Monitoring and Procedural Planning in Reconstructive Transplantation", in Proc. Of the 26th the Transplantation Society, Hong Kong, 2016.

***S. B. Raval,** T. Zhao, N. Krishnamurthy, T. S. Ibrahim, V. S. Gorantla, "Ultra-high Resolution Non-Contrast Vascular and Nerve Imaging for Graft Monitoring and Procedural Planning in Reconstructive Transplantation", in Proc. Of the Military Health System Research Symposium (MHSRS), Florida, 2016.

***S. B. Raval**, T. Zhao, N. Krishnamurthy, T. Santini, T. S. Ibrahim, V. S. Gorantla, "Ultra-high field upper extremity peripheral nerve and non-contrast vascular imaging at 7T tesla high resolution MRI", in Proc. Of the 12thInternational hand and Composite Tissue Allotransplantation Society Annual Meeting, Philadelphia, April 2015.

***S. B. Raval**, T. Zhao, Y. Zhao, V. S. Gorantla, T. S. Ibrahim, "Ultrahigh field(7T) magnetic resonance musculoskeletal imaging in upper extremity allotransplantation – first report in VCAMRI after upper extremity transplantation", in Proc. Of the 12thInternational hand and Composite Tissue Allotransplantation Society Annual Meeting, Philadelphia, April 2015.

***S. B. Raval**, T. Zhao, Y. Zhao, V. S. Gorantla, T. S. Ibrahim, "Ultrahigh field MRI after upper extremity transplantation"," in Proc. of The American Society of Plastic Surgery Annual Meeting, Boston, Nov 2015.

***S. B. Raval**, T. Zhao, N. Krishnamurthy, T. Santini, T. S. Ibrahim, V. S. Gorantla, "Ultra-high field upper extremity peripheral nerve and non-contrast vascular imaging at 7T tesla high resolution MRI", in Proc. of The American Society of Plastic Surgery Annual Meeting, Boston, Nov 2015.

***S. B. Raval**, T. Zhao, N. Krishnamurthy, T. Santini, T. S. Ibrahim, V. S. Gorantla, "RF System for Ultra-High Field Upper Extremity Imaging", in Proc. of The American Society of Plastic Surgery Annual Meeting, Boston, Nov 2015.

***S. B. Raval**, T. Zhao, N. Krishnamurthy, T. Santini, V. S. Gorantla, T. S. Ibrahim, "RF System for Ultra-High Field Upper Extremity Imaging", in 10th Biennial meeting at Center for Magnetic Resonance research, Minneapolis, Nov 2015.

S.B. Raval, T. Zhao, N. Krishnamurthy, Y. Zhao, S. Wood, K-T Bae, T.S. Ibrahim, "Initial Results: Ultra-High Field 32-ch Tx Body Array with Bright Centers" Podium presentation in Proc. of The 23rd International Society of Magnetic Resonance in Medicine Annual Meeting, Toronto, Canada, May 2015.

S.B. Raval, T. Zhao, N. Krishnamurthy, Y. Zhao, S. Wood, K-T Bae, T.S. Ibrahim, "Initial Results: Ultra-High Field 32-ch Tx Body Array with Bright Centers" Podium presentation in Proc. of The 23rd International Society of Magnetic Resonance in Medicine Annual Meeting, Toronto, Canada, May 2015.

S. B. Raval, T. Zhao, N. Krishnamurthy, T. Santini, V. S. Gorantla, T.S. Ibrahim, "Upper extremity neural and vascular imaging with UHF 7T MRI, " Podium presentation in Proc. of The 23rd International Society of Magnetic Resonance in Medicine Annual Meeting, Toronto, Canada, May 2015.

***S. B. Raval**, T. Santini, S. Wood, N. Krishnamurthy, T. Zhao, T.S. Ibrahim, "In-Vivo (8x4) 32-Ch Tx-Only Body Array for UHF MRI, " Oral presentation in Proc. of The 23th International Society of Magnetic Resonance in Medicine Annual Meeting, Honolulu, Hawaii, April 2017.

T. Santini, N. Krishnamurthy, S. Wood, **S. B. Raval**, Y. Zhao, A. Fischetti, M. Koo, A. Howard, and T. S. Ibrahim, "64 channel double-octagon Tx Head Coil for 7T Imaging" in Proc. of The 24th International Society of Magnetic Resonance in Medicine Annual Meeting, Honolulu, Hawaii, April 2017.

S. Wood, T. Santini, N. Krishnamurthy, **S. B. Raval**, and T. S. Ibrahim, "Evaluation of an Anthropomorphic Phantom with In-Vivo Using Quantitative MRI" in Proc. of The 24th International Society of Magnetic Resonance in Medicine Annual Meeting, Honolulu, Hawaii, April 2017.

T. Santini, J. H. Kim, S. Wood, N. Krishnamurthy, **S. B. Raval**, and T. S. Ibrahim, "A New RF Coil for Foot and Ankle Imaging at 7T MRI" in Proc. of The 24th International Society of Magnetic Resonance in Medicine Annual Meeting, Honolulu, Hawaii, April 2017.

T. S. Ibrahim, T. Santini, **S. B. Raval**, N. Krishnamurthy, S. wood, J. H. Kim, Y. Zhao, X. Wu, E. Yacoub, H. Howard, and T. Zhao, "A New RF Coil for Foot and Ankle Imaging at 7T MRI" in Proc. of The 24th International Society of Magnetic Resonance in Medicine Annual Meeting, Honolulu, Hawaii, April 2017.

V. E. Erbas, H. Sahin, S. Oksuz, L. Dong, M. R. Miller, G. Shojaati, G. Wollstein, K. C. Chan, I. Sigal, N. Kostereva, **S. B. Raval**, T. Ibrahim, J. L. Goldberg, L. Benowitz, J. S. Schuman, F. Zor, M. Solari, K. M. Washington, V. S. Gorantla, "A Preclinical Swine Model for Whole Eyeball Transplantation - Planning and Procedural Aspects" in Joint Meeting of American Association of plastic Surgeons & Plastic Surgery Research Council, Chicago, Nov 2016.

N. Krishnamurthy, Y. Zhao, J. Kim , **S. B. Raval**, T. Zhao and T. S. Ibrahim, "T2* Susceptibility Weighted and Echo- Planar Imaging at 7T using RF Shimming" in Proc. of The 23rd International Society of Magnetic Resonance in Medicine Annual Meeting, Toronto, Canada, May 2015.

S. Wood, N. Krishnamurthy, Y. Zhao, **S. B. Raval**, T. Zhao, J. A. Holmes, T. S. Ibrahim, "Anatomically Detailed Human Head Phantom for MR", in Proc. of The 22nd International Society of Magnetic Resonance in Medicine Annual Meeting, Milan, May 2014.

N. Krishnamurthy, Y. Zhao, J. Kim, **S. B. Raval**, T. Zhao and T. S. Ibrahim, "7T Multi-slab W hole-Head Homogenous and Low SAR T2 Acquisitions" Pittsburgh Imaging Community Retreat – Mellon Institute CMU, Pittsburgh, May 2014.

N. Krishnamurthy, Y. Zhao, R. Maccloud, T. Zhao, **S. B. Raval**, J. Kim, C. Rosano, H. Aizenstein, T. S. Ibrahim, "Segmentation of Small Veins Using 3D isotropic SW images at 7T" in Proc. of The 22nd International Society of Magnetic Resonance in Medicine Annual Meeting, Milan, May 2014.

N. Krishnamurthy, S. Wood, J. Kim, Y. Zhao, **S. B. Raval**, T. Zhao, T. S. Ibrahim, "Transmit Array Performance across Subjects at 7T MRI: Simulations and Experiments" in Proc. of The 22nd International Society of Magnetic Resonance in Medicine Annual Meeting, Milan, May 2014.

S. B. Raval, Y. Zhao, T. Zhao, N. Krishnamurthy, S. Wood and T. S. Ibrahim, "7T Tx Body Coil with Rx-Only Insert: Preliminary Results" in Proc. of The 21st International Society of Magnetic Resonance in Medicine Annual Meeting, Utah, May 2013.

Y. Zhao, T. Zhao, S. Wood, N. Krishnamurthy, **S. B. Raval**, J. Kim, T. S. Ibrahim, "3D SAR-Constrained Homogeneous B1+ Field at 7T" in Proc. of The 21st International Society of Magnetic Resonance in Medicine Annual Meeting, Utah, May 2013.

N. Krishnamurthy, **S. B. Raval**, Y. Zhao, S. Wood, T. Zhao, T. S. Ibrahim, “Experiment and Simulation Validation of the effect of 32 Channel Receive Array Inserts on Transmit B_1^+ and SAR at 7Tesla Parallel Transmit System” in Proc. of The 21st International Society of Magnetic Resonance in Medicine Annual Meeting, Utah, May 2013.

2.0 BACKGROUND

2.1 ULTRA-HIGH FIELD (UHF) MRI CHALLENGES AND MOTIVATION FOR USE

MRI, being a non-invasive modality, is the primary choice for addressing soft-tissue related challenges. UHF MRI has the inherent advantages of a higher static field (and therefore increased sensitivity), higher anatomical resolution, and reduced scan time, all of which can improve the throughput of clinical exams [29]. This higher static (B_o) field increase means a higher number of excited nuclei, which increases the SNR [30], chemical shift dispersion [31], susceptibility [32, 33], and blood oxygenation-dependent contrast [34], all of which increases the diagnostic capability of MRI and widens its research applications. However, translating clinical protocols from lower field imaging to UHF imaging faces many challenges [6, 12], including:

(i) B_1^+ field inhomogeneities: At 300MHz (7T), one electrical wavelength is approximately ~12cm in tissue. Since the physical size of the abdomen is 4-6 times larger than one electrical wavelength (~12cm), complex non-uniformities appear, resulting in bright and dark spots in the region of interest (ROI) [35, 36] in the images.

(ii) Higher Radiofrequency (RF) power requirements and SAR: 7T UHF MRI requires higher power when compared to clinical scanners (≤3T) [6].

(iii) RF penetration capability: The large heterogeneous abdominal anatomy leads to significant reduction in RF penetration, resulting in highly non-uniform images [35, 36].

(iv) Additional parameters:

a) Not only the organ/tissue's electromagnetic signatures, structure, and location inside the body, but also the coil design, geometry, and its position with respect to the subject could have a significant effect on tissue loading, B_1^+ field distribution, SAR and coil sensitivity [6, 12, 37-44].

b) In the case of extremity applications like transplant and various hand surgeries, surgeons are challenged to find the precise anatomical locations of abnormal soft tissue.

c) In certain conditions it is necessary to find how various tendons, ligaments, nerves, and muscles are interconnected to surrounding structures. These issues present significant challenge to protocol optimization when the B_1^+ field distribution inside the region of interest is not highly efficient.

Due to the intricate electromagnetic field behavior at ultra-high fields, 7T MRI has only been used as an investigational/research device so far. However, currently, efforts are being made to get FDA approval so that it may be used for clinical application. This study is timely, then, in that the RF coil systems presented in this dissertation will expand the technological boundaries of

UHF imaging, so as to not only enhance the fundamental scientific knowledge of RF coil design approach at high frequency, but also add to the realm of clinical applications of UHF body imaging.

2.2 RF COILS AT UHF

The first ever basic RF system, the coaxial cavity resonator, was built and tested by Pound, Torrey and Purcell [45, 46] after the end of World War II. In 1970, Ginsberg [47] experimented with a new Saddle coil design, where the current distribution was ideal, but the design was riddled with B_1^+ Inhomogeneity issues, a low filling factor, and a low upper frequency limit. In 1977, Schneider [48] introduced two slotted quarter wavelength tubes with a surround shield, achieving a higher sensitivity resonator. In 1979, Alderman and Grant [49] improved this same design by varying the length of elements for clinical spectroscopy applications. In 1980, Ackerman et al. introduced a small surface coil to image the spine, which had the advantage of higher SNR for smaller regions of interest. In 1984, Hayes introduced the Birdcage design [50], which allows for distributed capacitance and inductance. This feature allows increases in SNR and B_1^+ field homogeneity compared to the above mentioned saddle and slotted tube resonator designs. In 1997, Leifer [51] experimented with an elliptical BD coil to improve homogeneity and sensitivity further. In 1999, Bobroff and Mccarthy [52] proposed rectangular as well as elliptical slotted tube resonators as an alternative to noncylindrical BD coils, where inherent current pattern defines the performance of coils. Also, some of the other Birdcage designs (end capped birdcage design [53] in 1986 and half birdcage design [54] in 1990) added a physical ground plane to the coil. This helped to achieve a higher loading/filling factor [53, 54], which resulted in better imaging

outcomes. As a next step in improving RF coil performance, a dielectric resonators design was introduced in 1992, in which low conductivity dielectric material is used to make hollow cylinders. In the case of the birdcage design, the coil is surrounded by dielectric cylinders with a layer of a high dielectric constant material to improve the B_1^+ field homogeneity [55].

The first conceptual TEM resonator design with an open-circuited coaxial transmission line of varying length was proposed by Röschmann [56] in 1988. Simultaneously another patent was given to Bridges [57] for a design presenting TEM transmission elements arranged in a circular fashion and covered fully with a cylindrical copper shield. Then Vaughn et al. utilized sixteen TEM Roschmann resonators to build a TEM Coil [58]. Compared to other coils, the TEM coil is characterized by improved homogeneity, a higher Q factor, multiple frequency of operations and a minimal decrease in SNR. As a next step in improving the B_1^+ field distribution the authors in [59, 60] demonstrated the use of a distributive type of capacitance that makes it easier to separate the resonant modes and improve the B_1^+ field homogeneity over the region of interest. In 2009 Morich introduced a TEM design where the RF shield is part of coil itself, and SAR and B_1^+ uniformity can be adjusted by varying the length of TEM elements. Also, for this design the B_1^+ field uniformity is more like that for an unshielded BD [61].

Adriany et al., highlighting that with ultra-high field wavelength effects, there is a need to consider the coil current phase effects, created a design that consists of transmission line elements as basic building blocks. This lines act as a transceiver array at ultra-high fields. This design incorporates an RF shield into a resonant structure, lessening radiation issues and improving coil performance. Also, receive coil arrays can be added to these transmit arrays in close proximity

and still achieve good decoupling [62, 63]. Even after addressing radiation losses, the author mentioned that this design still had increased sample losses and difficulty in decoupling coil elements that needed to be managed [6, 64]. When comparing the novel adjustable transceiver coil to a fixed geometry transceiver array, clear gains in peripheral SNR, transmit efficiency, and, in particular, parallel imaging performance, were observed [65].

Other researchers have provided information about a few more distinctive design approaches. In 2006 Wang C. et al. performed a comparative study showing that the birdcage coil had the best unloaded B_1^+ field homogeneity, the TEM coil had the best loaded B_1^+ field homogeneity and the lowest radiation loss, while the micro-strip coil was better in SAR and SNR at 7T than the other two designs [66]. In 2015, Li et al demonstrated a rotating RF Coil array (RRFCA) with uniform image reconstruction for the homogeneous phantom and a significant reduction in scan time for a homogeneous phantom at 7T. However, when compared to a similar channel stationary coil array, the RRFCA can still reconstruct better images with higher quality at higher reduction factor. This means that UHF MRI can benefit from the proposed rotation-dependent sensitivity estimation algorithm and the acceleration ability of the RRFCA [67]. In 2015 [68] and 2016 [69] Raaijmakers et al. presented the application of a dipole antenna and a comparison with a loop array coil. They showed that in comparison with loop coils, dipole antennas have a higher receive sensitivity/transmit efficiency from a given depth onwards. Zhang et al. offer a feasibility study of a travelling wave system in body applications at 7T [70]. This study shows that traveling wave excitation still experiences inhomogeneity issues in whole body imaging at 7T but that parallel transmit approaches are potential solutions for solving the non-uniformity related issues in the deep region of the torso at 7T [70].

2.3 FINITE DIFFERENCE TIME DOMAIN (FDTD)

2.3.1 Motivation for FDTD Modelling

Moving from a low field to an ultra-high static (Bo) field, the ratio of the aligned nuclei in the human body becomes larger. This results in a higher SNR, which in turn results in a higher quality image. However on the technical side, the Larmor frequency rises linearly with an increasing Bo field, and the operational frequency for proton imaging rises to equal the Larmor frequency. In turn the RF wavelength becomes smaller than the electrical dimensions of the coil and structures like the abdomen become bigger than or comparable in size to the operating wavelength. For example, at 7T, the physical size of the abdomen is 4-6 times larger than one electrical wavelength (~12cm) at 297.2MHz, as compared to with a lower field (≤3T), where the biological subject is relatively smaller, electrically. A circuit analysis cannot predict these coil currents behavior. As the human body contains various body organs, including the abdomen, which are of a highly inhomogeneous structure with lossy materials, strong electromagnetic interactions are expected between the RF coil structure, the excitation source(s) and the various tissues. At Ultra-high fields, this produces non-uniform images with bright and dark spots inside the human body. Also, the interactions between the RF coil structure, excitation source(s), and various tissues can generate unwanted local RF hot spots inside the various abdominal organs. This creates the necessity for approaches like full wave electromagnetic methods for analyzing the UHF MRI coil problem.

2.3.2 FDTD Background

For medical applications, electromagnetic simulations are extensively used in both academia and private industry. For example, full wave methods are typically used for modelling microwave hyperthermia [71-73] in tumor applications to calculate the SAR of various tissues in communication (antenna, phones, power transmission lines) applications [74, 75]. Most of the MRI systems in the market are either 1.5T or lower field systems, so there has been no immediate need for full wave numerical approaches. As a result, circuit-based approximations are appropriate for numerically modelling the RF coils. However, with the introduction of ultra-high fields (4T [76, 77], 7T [6], 8T [78]) in recent times, the need for full-wave methods has become much more urgent (as explained in section 2.3.1) in order to simulate, design and evaluate the RF coils using an anatomically detailed human model. It is also predicted that RF coil design, optimization, and evaluation will depend heavily on numerical approaches [79-81].

The FDTD method has been used in calculating electromagnetic field interaction between human biological tissues and radiating objects such as surface MRI RF coils [82, 83]. Significant effort has been devoted to modeling the electrical characteristics of RF whole body and upper extremity coils, which is discussed in detail in chapters 3-5.

Jin et al [84] utilized the fast Fourier transform method to evaluate the electromagnetic fields inside a birdcage coil in conjunction with a human head model. [85, 86] present the details of FDTD modelling of a birdcage coil loaded with a human head model. These studies mention that RF coil functions as an azimuthal transmission line at all the frequencies of interest [60, 84-

88]. For example, RF evaluation was done by determining the coil current distribution without the head being present using the method of moments [86]. Method of moments was utilized to predict the currents in the coil without the presence of human head model or utilized voltage sources instead of lumped capacitors with varied sinusoidal magnitude [85]. In turn, the coil currents distribution on the birdcage elements are required to have the following sinusoidal distribution which results in a TEM mode of operation:

$$I_i = I_{max} Cos \frac{(i-1)*\Pi}{N} \quad (1.1)$$

where *Ii* is the current in the *i*th element, *Imax* is the maximum current and *N* is the number of current elements.

Since there is electromagnetic coupling between the head model and coil, these assumptions are not completely valid [89, 90]. At 1.5T, these resulting inaccuracies in field distribution calculations may not be too significant but it is much more prone to be invalid at higher static Bo frequencies. Even when the coil is empty, there are many cases where the ideal current distribution is not present [90, 91]. When neglecting the effect of the head model on the coil, current distribution can be a major source of error; the most accurate simulations present coil and object model as a single system [86]. It is considered a difficult problem [86]; FDTD modelling work is considered in more detail in the chapters of this dissertation.

2.3.3 FDTD Method

In 1966 [92] Kane Yee introduced Finite time difference time domain methods to provide a direct solution to Maxwell's time dependent curl equations. This technique replaces the spatial

and time domain derivatives of Maxwell's equations with finite difference approximations [93]. A second order accurate central difference approximations is used in place of the differential operators of the curl equations [94]. Maxwell's equations [95] for isotropic, source free and homogeneous media are given as:

$$\nabla x\vec{E} = -\frac{\partial \vec{B}}{\partial t} - \sigma_m \vec{H}, \quad (\overrightarrow{B} = \mu\overrightarrow{H}, \overrightarrow{M} = \vec{M}_{source} + \sigma^* \overrightarrow{H}) \tag{1.2}$$

$$\nabla x\vec{H} = \frac{\partial \vec{D}}{\partial t} + \sigma_e \vec{E}, \quad (\overrightarrow{D} = \varepsilon\overrightarrow{E}, \ \vec{J} = \vec{J}_{source} + \sigma\overrightarrow{E}) \tag{1.3}$$

$$\nabla x\vec{D} = \rho_e \tag{1.4}$$

$$\nabla x\vec{B} = \rho_m \tag{1.5}$$

Where *E (V/m*) is electric field, H (A/m) is magnetic field, D(C/m2) is electric field density, B (w/m2) is magnetic flux density, and J (A/m2) is electric current density. M (V/m2) is equivalent magnetic current density. σ*m (Ω/m) and* σ*e (S/m)* are the magnetic and electric conductivities, respectively. The dielectric parameters, permeability and permittivity are given by μ (*H/m)* and ε (*F/m)*, while ρ*e (C/m*3) and ρ*e (Wb/m*3) are the electric and magnetic charge densities, respectively. These rectangular coordinates in three-dimensional structures are as:

$$\mu\frac{\partial H_x}{\partial t} = \frac{\partial E_y}{\partial z} - \frac{\partial E_z}{\partial y} - (M_{source_x} + \sigma * H_x) \tag{1.6}$$

$$\mu\frac{\partial H_y}{\partial t} = \frac{\partial E_z}{\partial x} - \frac{\partial E_x}{\partial z} - (M_{source_y} + \sigma * H_y) \tag{1.7}$$

$$\mu \frac{\partial H_z}{\partial t} = \frac{\partial E_x}{\partial y} - \frac{\partial E_y}{\partial x} - (M_{source_z} + \sigma * H_z) \quad (1.8)$$

$$\varepsilon \frac{\partial E_x}{\partial t} = \frac{\partial H_z}{\partial y} - \frac{\partial H_y}{\partial z} - (J_{source_x} + \sigma E_x) \quad (1.9)$$

$$\varepsilon \frac{\partial E_y}{\partial t} = \frac{\partial H_x}{\partial z} - \frac{\partial H_z}{\partial x} - (J_{source_y} + \sigma E_y) \quad (2.0)$$

$$\varepsilon \frac{\partial E_z}{\partial t} = \frac{\partial H_y}{\partial x} - \frac{\partial H_x}{\partial y} - (J_{source_z} + \sigma E_z) \quad (2.1)$$

Where H and E are both in the x, y and z directions**.** The space and time points for any function v were introduced by Yee [55] with Δx, Δy and Δz components, with the time component being Δt. I, j, k, and m are integers. Central difference expressions obtained using Taylor's theorem for the space for the x direction and the time derivatives for function v are shown below:

$$(i\Delta x, i\Delta y, k\Delta z, n\Delta t)\frac{\partial v}{\partial x} = \frac{v^n(i+1/2,j,k) - v^n(i-1/2,j,k)}{\Delta x} + O((\Delta x)^2) \quad (2.2)$$

$$(i\Delta x, i\Delta y, k\Delta z, m\Delta t)\frac{\partial v}{\partial x} = \frac{v^{m+1/2}(i,j,k) - v^{m+1/2}(i,j,k)}{\Delta t} + O((\Delta t)^2) \quad (2.3)$$

In order to achieve second order accuracy, the error terms $O((\Delta x)^2)$ and $O((\Delta t)^2)$ can be dropped, so the FDTD equations become:

$$E_x^{n+1}\left(i+\frac{1}{2},j,k\right)=\left(\frac{2\varepsilon-\sigma\Delta t}{2\varepsilon+\sigma\Delta t}\right)E_x^{n}\left(i+\frac{1}{2},j,k\right)+\left(\frac{2\Delta t}{2\varepsilon+\sigma\Delta t}\right)\frac{H_z^{n+\frac{1}{2}}(i+\frac{1}{2},j+\frac{1}{2},k)-H_z^{n+\frac{1}{2}}(i+\frac{1}{2},j-\frac{1}{2},k)}{\Delta y}-\frac{H_y^{n+\frac{1}{2}}(i+\frac{1}{2},j,k+\frac{1}{2})-H_y^{n+\frac{1}{2}}(i+\frac{1}{2},j,k-\frac{1}{2})}{\Delta z}-J_{source\_x}^{n+\frac{1}{2}}\left(i+\frac{1}{2},j,k\right) \quad (2.4)$$

$$E_y^{n+1}\left(i,j+\frac{1}{2},k\right)=\left(\frac{2\varepsilon-\sigma\Delta t}{2\varepsilon+\sigma\Delta t}\right)E_y^{n}\left(i,j+\frac{1}{2},k\right)+\left(\frac{2\Delta t}{2\varepsilon+\sigma\Delta t}\right)\frac{H_x^{n+\frac{1}{2}}(i,j+\frac{1}{2},k+\frac{1}{2})-H_x^{n+\frac{1}{2}}(i,j+\frac{1}{2},k-\frac{1}{2})}{\Delta z}-\frac{H_z^{n+\frac{1}{2}}(i+\frac{1}{2},j+\frac{1}{2},k)-H_y^{n+\frac{1}{2}}(i-\frac{1}{2},j+\frac{1}{2},k)}{\Delta x}-J_{source\_y}^{n+\frac{1}{2}}\left(i,j+\frac{1}{2},k\right) \quad (2.5)$$

$$E_z^{n+1}\left(i,j,k+\frac{1}{2}\right)=\left(\frac{2\varepsilon-\sigma\Delta t}{2\varepsilon+\sigma\Delta t}\right)E_z^{n}\left(i,j,k+\frac{1}{2}\right)+\left(\frac{2\Delta t}{2\varepsilon+\sigma\Delta t}\right)\frac{H_y^{n+\frac{1}{2}}(i+\frac{1}{2},j,k+\frac{1}{2})-H_y^{n+\frac{1}{2}}(i-\frac{1}{2},j,k+\frac{1}{2})}{\Delta z}-\frac{H_x^{n+\frac{1}{2}}(i,j+\frac{1}{2},k+\frac{1}{2})-H_x^{n+\frac{1}{2}}(i,j-\frac{1}{2},k+\frac{1}{2})}{\Delta x}-J_{source\_y}^{n+\frac{1}{2}}\left(i,j,k+\frac{1}{2}\right) \quad (2.6)$$

$$H_x^{n+\frac{1}{2}}\left(i,j+\frac{1}{2},k+\frac{1}{2}\right)=\left(\frac{2\mu-\sigma*\Delta t}{2\mu+\sigma*\Delta t}\right)H_x^{n-\frac{1}{2}}\left(i,j+\frac{1}{2},k+\frac{1}{2}\right)+\left(\frac{2\Delta t}{2\mu+\sigma*\Delta t}\right)\frac{E_y^n(i,j+\frac{1}{2},k+1)-E_y^n(i,j+\frac{1}{2},k)}{\Delta z}-\frac{E_z^n(i,j+1,k+\frac{1}{2})-E_z^n(i,j,k+\frac{1}{2})}{\Delta y}-M_{source\_x}^n\left(i,j+\frac{1}{2},k+\frac{1}{2}\right) \quad (2.7)$$

$$H_y^{n+\frac{1}{2}}\left(i+\frac{1}{2},j,k+\frac{1}{2}\right)=\left(\frac{2\mu-\sigma*\Delta t}{2\mu+\sigma*\Delta t}\right)H_y^{n-\frac{1}{2}}\left(i+\frac{1}{2},j,k+\frac{1}{2}\right)+\left(\frac{2\Delta t}{2\mu+\sigma*\Delta t}\right)\frac{E_z^n(i+1,j+\frac{1}{2},k+\frac{1}{2})-E_z^n(i,j+\frac{1}{2},k+\frac{1}{2})}{\Delta x}-\frac{E_x^n(i+\frac{1}{2},j,k+1)-E_x^n(i+\frac{1}{2},j,k)}{\Delta z}-M_{source\_y}^n\left(i+\frac{1}{2},j,k+\frac{1}{2}\right) \quad (2.8)$$

$$H_z^{n+\frac{1}{2}}\left(i+\frac{1}{2},j+\frac{1}{2},k\right)=\left(\frac{2\mu-\sigma*\Delta t}{2\mu+\sigma*\Delta t}\right)H_z^{n-\frac{1}{2}}\left(i+\frac{1}{2},j+\frac{1}{2},k\right)+\left(\frac{2\Delta t}{2\mu+\sigma*\Delta t}\right)\frac{E_x^n(i+\frac{1}{2},j+1,k)-E_x^n(i+\frac{1}{2},j,k)}{\Delta y}-\frac{E_y^n(i+1,j+\frac{1}{2},k)-E_y^n(i,j+\frac{1}{2},k)}{\Delta x}-M_{source\_z}^n\left(i+\frac{1}{2},j+\frac{1}{2},k\right) \quad (2.9)$$

For electric field components, the surrounding fields are magnetic field components. And for magnetic components, the surrounding fields are electric field components. Based on the minimum wavelength of the problem, a spatial step is chosen (good choice is λmin/20). The criteria for selecting the time step Δt is based on Courant-Friedrichs stability criterion [96]. It is based on the time and space eigenvalue problem of Maxwell's time-dependent equations.

$$\Delta t \leq \frac{1}{Vmax\sqrt{\frac{1}{\Delta x^2+\Delta y^2+\Delta z^2}}} \tag{2.10}$$

Where, Vmax = $1/\sqrt{\mu\varepsilon}$ is the maximum wave speed inside the medium.

A 3D Yee cell is shown in below, with electric and magnetic field vector components with an (I, j, k) position.

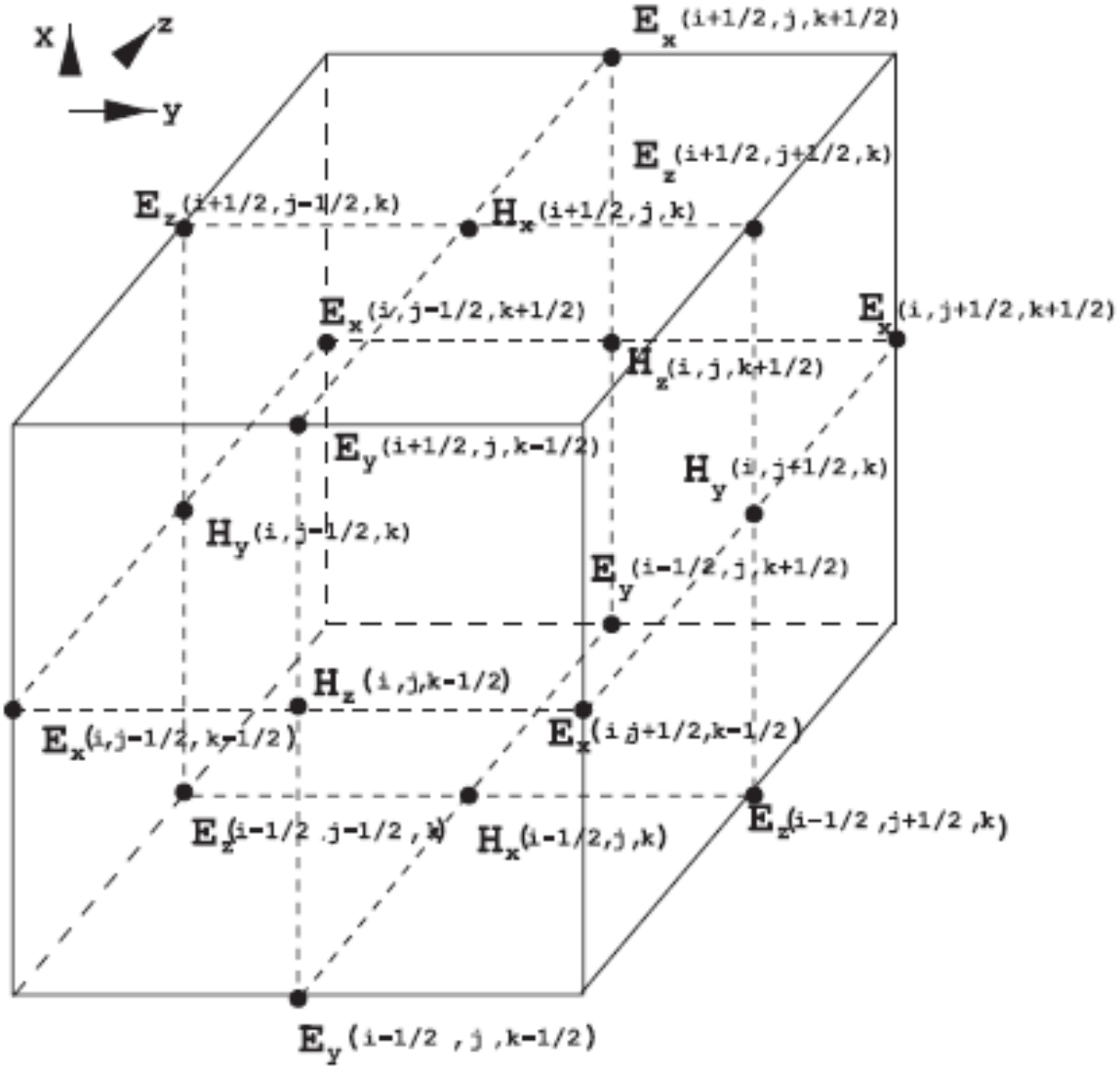

Fig 2.1 A 3D YEE cell.

Also, the spatial step is directly proportional to the minimum wavelength of the problem (maximum size of 1/10 of a wavelength). This is only where accuracy is surpassed by wavelength, the domain is multiple wavelengths and each element in the domain can be represented by at least single spatial step. In case of lossless, spatial step ($\Delta x = \Delta y = \Delta z$) is:

$$\Delta x = \frac{\lambda_{min}}{20} = \frac{f}{20\sqrt{\mu_{max}\varepsilon_{max}}} \tag{2.11}$$

Where f (Hz) is the frequency of operation. λ (m) is the minimum wavelength. μ (max) and σ (max) are the maximum relative permeability and permittivity, respectively.

Figure 2.1 shows the Electric and magnetic field components of the Yee cell. At the center of every edge on the block, electric field values are sampled. The electric field vector directions are the same as the directions of these edges. At the center of each block face, the magnetic field value is sampled. The magnetic field vector directions are perpendicular to each of these block faces.

2.3.4 The Human Model

The 1mm duke male model from a visible human [97] project (age: 34, height: 1.77m, weight: 72.4kg, bmi: 23.1 kg/m^2) was used in this dissertation with a converted resolution of 1.58x1.58x1.58mm3. It includes 77 various tissue types. Coil positioning with respect to the model was kept as close as possible to a real experimental setup.

3.0 DESIGN, DEVELOPMENT AND EVALUATION OF WHOLE BODY RADIOFREQUENCY TRANSMIT ONLY AND RECEIVE ONLY INSERT ARRAY AT 7T.

3.1 INTRODUCTION

Since its introduction, researchers have been pushing for clinical applications of 7T in various realms of the human body. The National Cancer Society's (NCI) 2008-2012 report presented detailed statistics on abdominal organs (liver, kidney, bladder, prostate, colon and others) with cancer [98, 99]. The kidney, pancreas, liver and bile duct are the major abdominal organs where cancer related deaths have been reported [98] [99]. MRI, which is growing as a diagnostic and research tool, is the primary non-invasive method, especially for addressing soft tissue related challenges [10, 11] as mentioned earlier. UHF MRI has distinct advantages over lower field MRI, including a higher SNR [6], higher anatomical resolution and reduced exam time when compared to the existing/commercial clinical scanners (≤3T) in hospitals. However, UHF MRI still experiences challenges [12] such as inhomogeneities in the B_1^+ field (the circularly polarized component of the transverse magnetic field that excites the spins) and higher RF power deposition (local and global SAR), that require the need for RF development. Until now, all of the major

efforts have been focused on imaging the brain [20-22] with somewhat successful results, with little research being devoted to the imaging of the human torso/body and extremities (except the knee [18, 23, 24]). This leaves a tremendous need for attention towards the body (kidney, liver, pancreatic) and extremity conditions [12].

Few research groups have developed body coils at 3T and 7T. Especially given the technical difficulty and challenges presented at high field (3T) and ultra-high fields (7T and higher), there are few research groups who have attempted various distinctive body coil designs at 3T and 7T that demonstrate the potential for clinical imaging. Specifically, Vernickel et al [44] show an eight-channel 3T transmit/receive body coil design at 3T; Wu et al [100] discussed the performance of various RF coil designs, including a birdcage, single-ring stripline, and multi-ring stripline array; and Tian et al [101] present seven different TEM array configurations and compare them with a high pass birdcage coil and two loop array configurations for optimal body coils. When compared with the birdcage coil, all designs improved the RF field homogeneity, with 3D arrays performing better than 2D arrays for the same type of array elements. TEM arrays provided better B_1^+ homogeneity, and less peak 10gram SAR than loop arrays.

At 7T, Raaijmakers et al [68, 69] presented the application of a dipole antenna and compares it with a loop array coil in body imaging. When compared to loop coils, dipole antennas were shown to have higher receive sensitivity/transmit efficiency from a given depth onwards. As the Larmor frequency increased, the transition depth decreased. For a single loop coil, the B_1^+ over $\sqrt{SAR_{max}}$ ratio was more favorable than that of single dipole antennas, for any depth and for any frequency. However, when operating in an array, this relationship is not straightforward and

a loop coil with geometric overlap generates higher SAR levels. Vaughan et al [12, 21] showed the application of whole body imaging using a multichannel TEM transceiver coil at 7T UHF MRI, where homogeneity and signal intensity was improved with B_1^+ shimming for imaging local regions of interest. Abraham et al [102] demonstrated homogenous whole-slice (demonstrated in three axial, sagittal, and coronal slices) and 3D localized (demonstrated in the heart) excitations. Orzada et al [103] showed application of TIAMO to reduce inhomogeneity in abdominal/body imaging application. Hezel et al [104] showed the potential for clinical imaging while listing technical challenges like B0 variations, T2* dephasing, and necessity of a larger chemical shift to carry out successful abdominal fat/water imaging at 7T UHF. Snyder et al [105] compared eight- and sixteen-channel transceive stripline/TEM body arrays at 7T (297 MHz) both in simulation and experiment. Zhang et al [70] demonstrated the application of a travelling wave system and compared it to a TEM body coil at 7T.

As mentioned above, the complex electromagnetic field behavior at ultra-high fields (7T and beyond) creates many practical challenges [12] like B_1^+ field inhomogeneities, where the wavelength of interest becomes shorter or comparable to the region being imaged. In the case of the abdomen, the wavelength is 4-6 times shorter (approx. 12cm) than the body at 300MHz. This creates non-uniform wave behavior in ROI, resulting in bright and dark spots (constructive/destructive interference). Another practical challenge of UHF imaging is the significantly high RF power requirement, and therefore SAR, when compared to that at lower field strength [6]. Another significant issue is the lack of RF penetration inside the body tissue [35, 36]. Therefore, not only the tissues' electromagnetic signature and their location inside the body, but also the coil design, geometry, and position with respect to the subject can have a significant effect

on tissue loading, B_1^+ field distribution, SAR, RF power requirements and coil sensitivity [12, 21, 37-44].

Diverse RF probe designs as well as other MRI approaches have been tested as MR research has transitioned from low field to high field MRI applications. Moving fundamentally from lumped element (R, L, and C) and transmission line theories to full wave Maxwellian electromagnetic theory, the Tic Tac Toe (TTT) coil [26] presented here is a distinctive design to be used for 7T UHF body imaging in combination with a decoupled receive-only-insert to reduce noise, and thus provide excellent SNR [106]. This TTT design has never been applied in body imaging before. However, there are few research groups that have published work regarding UHF MRI in different parts of the human body [12, 14-17, 19].

This work demonstrates an in-house developed and numerically simulated 32CH RF Tx body coil design. Specifically, a thirty-two channel, 8 X 2 X 2 cross-pole [107-109] 7T RF array for the body region is presented in this study. While it has the capability of independently driven excitation sources, in this work, we used different phases and identical amplitudes to create a pseudo circularly polarized field. Experimental and numerical studies were performed and quantitatively analyzed to evaluate the RF body coil. The developed RF array inherently shows high couplings (S13 = ~-3 to -4dB and S12 = -8 to -9dB) between the excitation elements. Thus, B_1^+ field intensity supplied (by the system) power is typically lower than the traditional body RF coils; however, the array exhibits more homogeneous and consistent B_1^+ field distributions in the body [25].

TTT RF coil designs are inherently highly coupled, having the higher RF transmission properties associated with highly coupled coils, which property enables them to negate the aforementioned loading effects (ultra-high field electromagnetic effects). This helps overcome the loading dependency [20, 25, 26], which means no tuning, matching or RF shimming from subject to subject is required. The complex interaction (loading) between the biological tissue and the coil has been problematic due to the variations in electromagnetic properties as well as geometrical properties [37-39, 42, 43]. The higher RF transmission properties (highly coupled coils) of this coil design, make it load-insensitive [20, 25, 26]. This helps in implementing a circularly polarized field or other shimming methodologies without the need for measuring the transmission field (B_1^+).

Our aim is to create a TTT coil in combination with a multi-channel receive-only insert array for whole body (various abdominal organs) imaging at 7T UHF MRI. FDTD calculations of the coil properties will be presented. T1 weighted sequences with and without the receive-only insert array will be presented.

3.2 MATERIALS AND METHOD

3.2.1 FDTD Modelling

As the operational wavelength comes close to the RF coil dimensions and electrical size of the load, full wave analysis becomes important to find out the interaction between body and RF

coil, which in turn helps in designing a more uniform RF coil with lower and consistent local and global SAR [110, 111]. Figure 3.1A shows a detailed coil model with a spherical body phantom model. Figure 1B shows the excitation ports. Figure 3.1C shows the human model within the coil model. A detailed simulation method mentioned in Ibrahim et al [112, 113] was followed; the TTT Tx coil is simulated as shown in Figures 3.1A, 3.1C with the model (spherical body phantom model/visible human model) as a single system [39, 40] using the FDTD method. First, the coil geometry, including the shield, coil excitation ports, coil elements, and tuning/matching rods, was accurately modeled including the spherical body phantom model/visible human model using a mesh created by MATLAB (MATHWORKS, MA). This resulted in a three dimensional grid structure of 331x311x228 cells in the case of the coil with spherical body phantom model and 296x296x746 cells in the case of the coil with the visible human model, as shown in Figure 3.1A, and 3.1C, respectively.

Constitutive electromagnetic properties such as electric conductivity (σ), dielectric constant (ε), magnetic conductivity, were assigned to each element, such as acrylic, phantom material, the biological tissues air, at the resonance frequency of 7T UHF MRI (297.2 MHz) as per the Yee cell [92]. The copper elements and shields were modeled as perfect electrical conductors (PEC), with the tangential E field component set to zero. A three dimensional grid model with spatial resolution of 1/16 of an inch (1.58mm) and temporal resolution of $6 \times 10^{(-12)}$ sec were used to meet the Courants stability criteria. The computational domain was surrounded by 32 layers of perfectly matched layers to reduce the effects of the reflected electromagnetic field (to mimic the experimental environment) as per Beringer [114, 115]. Once the required copper geometry was created, it was fed into in-house developed second order accurate central difference

time domain equations (Maxwell's equations), which calculated the E field and H field on the 3D Yee cell, at spatial intervals of (Δ/2) and temporal interval of (Δt/2) in a leapfrog manner. The value of $H_{(x,y,z)}(/E_{(x,y,z)})$ at a particular position can be calculated from its previous value of $E_{(x,y,z)}(/H_{(x,y,z)})$ at the adjacent grid location. As the outcome of the simulation, we not only could calculate the currents on the coil and the reflection coefficient (S11), but also the B_1^+ (magnetic field) distribution and SAR.

The original 1mm Duke male model [116] (age: 34, height: 1.74 m, weight: 70 kg, 77 different types of tissues, body mass index (bmi): 23.1 kg/m2) was rescaled to a resolution of 1.58x1.58x1.58 mm^3. It was located inside the RF coil to resemble the experimental environment in-vivo.

Here, the deposited energy in tissue is given by the product of induced current density and induced electric field E ($P = J*E = \sigma E^2$). In addition, peak SAR (W/kg) was calculated using the following equation and was determined for 10 gram pixel average:

$$SAR_{(i,j,k)} = \frac{1}{2}\left\{\frac{\sigma_{(i,j,k)}\left(E^2_{x(i,j,k)}+E^2_{y(i,j,k)}+E^2_{z(i,j,k)}\right)}{\rho_{(i,j,k)}}\right\} \quad \textbf{(1.1)}$$

Where Ex, Ey and Ez are the E field magnitude in the tissue in V/m, sigma (σ) is the conductivity in siemens/m and rho (ρ) is the density of tissues in kg/m3 in the sample; i, j, and k represent locations in the Cartesian coordinate System.

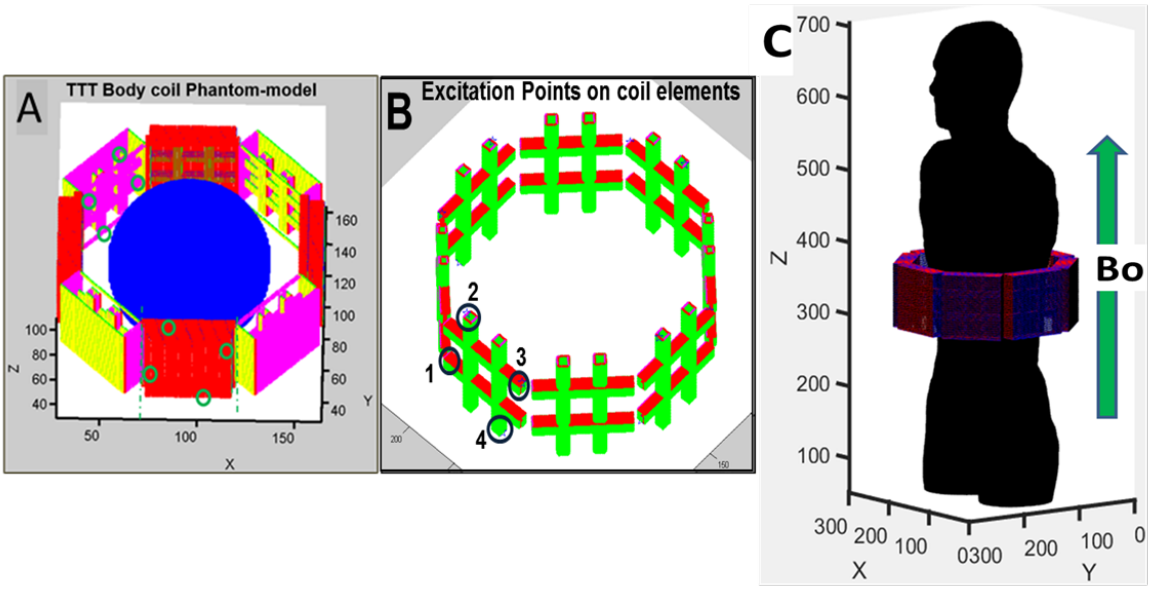

Figure 3.1 Coil simulation models (with phantom and human body model). A. FDTD model of 32CH TTT Tx body coil with spherical body phantom model (ports shown by green circles); B. thirty-two channel TTT Tx body coil showing the locations of the excitation ports (for simplification, only four port locations are shown since the remaining sides of the coil have a similar configuration); C. FDTD model of thirty-two channel TTT Tx body coil with the anatomically detailed Duke human model.

3.2.2 Transmit and Receive RF Array Design

3.2.2.1 Thirty-Two Channel Transmit Array Coil: A thirty-two channel Tx body coil containing eight decoupled sets of highly couple 4-channel arrays was constructed in-house, described as a TTT of coaxial transverse electromagnetic (TEM) elements. Each set is put in a 2

x 2 arrangement, forming a tic-tac-toe configuration (Figure 1B). These square struts have inner copper rods inside the outer strut covered with copper sheet (thickness = 8 um). The inner and outer struts are separated by a dielectric sleeve (Teflon filling), as shown by the arrows in the schematics in Figure 3.2A. In association with a conductive cylinder, this creates a transmission line, with the struts as inner conductors and the cavity walls as outer conductor. Also, the inner struts are electrically connected to the RF shield while the outer struts are electrically isolated from end shield plates by a small gap (0.5 inch).

The inner struts have a gap in the center, and they can be adjusted by pulling them in and out of the cavity resonator, ultimately changing the capacitance between the inner and outer conductor in order to tune the 2 x 2 side to 297.2 MHz. The inner rod is electrically connected to the surrounding RF copper shield. The outer struts are electrically isolated from the inner struts and the RF shield. Each conjoined place where two coil sides come in contact is covered with adhesive copper tape to decrease the radiation loss and increase RF efficiency [117] (green dotted line in Figures 1A, 2B). All the lengths of the 32 inner rods were numerically calculated. The actual rods were then manually inserted and adjusted to achieve precise tuning and matching on each 2 x 2 coil side. All thirty-two coil elements were tuned and matched to 297.2 MHz and the S matrix was measured using a vector network analyzer (HP, USA).

The schematics of each of the coil sides are shown in Figure 3.2A, including all four excitation sources marked with yellow circles. The coil design parameters are listed in Table 3.1. Figure 3.2B shows how eight of the coils form an octagon-shaped thirty-two channel TTT RF body (Figure 3.1A, 3.1B, 3.2B) coil [118]. All eight coil sides were put together in the octagon shape

using two circular rings (front and back). Each circular ring was further divided into a semi-circle arrangement. As shown in Figure 3.2B, the whole body coil can open and close using two latches (Black latches) on either side in the front or back. Since each coil side has an excitation port in the same location, when put together they form four levels with eight excitation ports on each level, L1 to L4, as shown in Figure 3.2B. Figure 3.2C shows the phase-only arrangement on all four levels. Each level has 8 excitation ports, with a 45° phase difference between each adjacent two ports, starting from 0° to 360° in a clockwise direction. There is a 180° difference between each level, as shown in Figure 3.2C. All the workbench measurements were performed using a calibrated vector network analyzer (Agilent E5062A, USA) together with a multiport S parameter test set (87050EA, Agilent, CA USA) for all eight sides/panels, as described in a later section. Eight transmit channels from a pTx plug were connected to eight 1:4 Wilkinson power dividers (splitter) and constant phase shifters in order to produce a pseudo circularly polarized (CP) mode. All 32 transmit channels were arranged in a quadrature excitation fashion on all four levels of the transmit array. Looking in the Bo direction, the phases of the voltages were rotating clockwise, with increments of 45° on each level and 180° difference between different levels, as shown in Figure 2C. There are four Z levels (L) in the coil, as shown in Figure 3.2B. Referred to as L1 to L4, each level contains eight Tx channels.

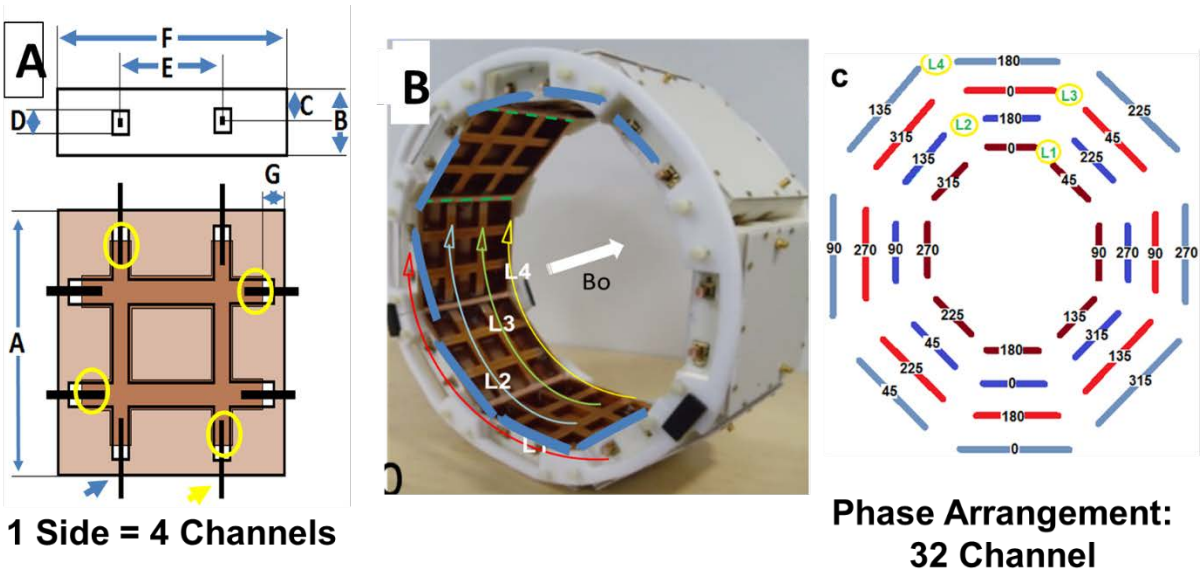

Figure 3.2 Transmit only array RF system. A. Single side showing coil design parameters and different coil ports; B. Constructed 32CH TTT body coil showing all four levels L1 to L4 in the Bo direction, and potential receive insert location (blue dotted lines); C. Phase arrangement between the coil ports.

Table 3.1 Transmit Coil Design Parameters

Coil design parameters for one single side	
Element height	1.5 inch
Center of strut to endcap	1 inch
Strut cross-section width	0.5 inch
Strut cross-section length	0.5 inch
Shield to copper	0.125 inch
Strut length	5.25 inch
Strut width	5.25 inch
Center gap width	2 inch

3.2.2.2 Sixteen Channel Receive Only Array: A sixteen channel receive only array was developed to fit inside the Tx coil on a flexible acrylic frame (McMaster Carr, Elmhurst, IL) with flexible Teflon sheeting (McMaster Carr, Elmhurst, IL) that can bend at the middle of each element, as shown in Figure 3.3. Each element is 10x10 cm^2 in size. Here, the coil array contains two rows of eight loop Rx only coils, as shown in Figure 3.3. The coil array contains sixteen inductively decoupled surface loops (orthogonal to Bo direction) evenly distributed. A network analyzer was used to measure the performance of the Rx only coil. Overlapping distance was adjusted manually (Figure 3.3) to reduce the crosstalk induced by neighboring loops, whereas the preamplifier decoupling method was used to tackle the mutual inductance (adding -15 dB additional isolation) caused by next neighboring/non-adjacent loops [44]. The Rx coil is positioned in between the subject and Tx coil (Figure 3.3B). Each loop contains two passive detuning circuits, which are used to decouple the receive loops during transmit operation, making it basically an L-C tuned circuit with bidirectional PIN diodes that turns ON and OFF as a function of radio frequency. In summary, the TTT Tx coil can operate as a transmit and receive coil, whereas the receive-only-insert can only acquire the signal from the ROI being imaged. The noise correlation measurement was evaluated to precisely measure the decoupling performance, as discussed a later in section. Detuning of the Tx coils during the receive mode was guaranteed by the L-C tank circuits, which act as a band stop filter on all 4 sides for each panel. The Tx detuning was measured by checking the S parameters (S11, S12) using active bias applied through the power supply.

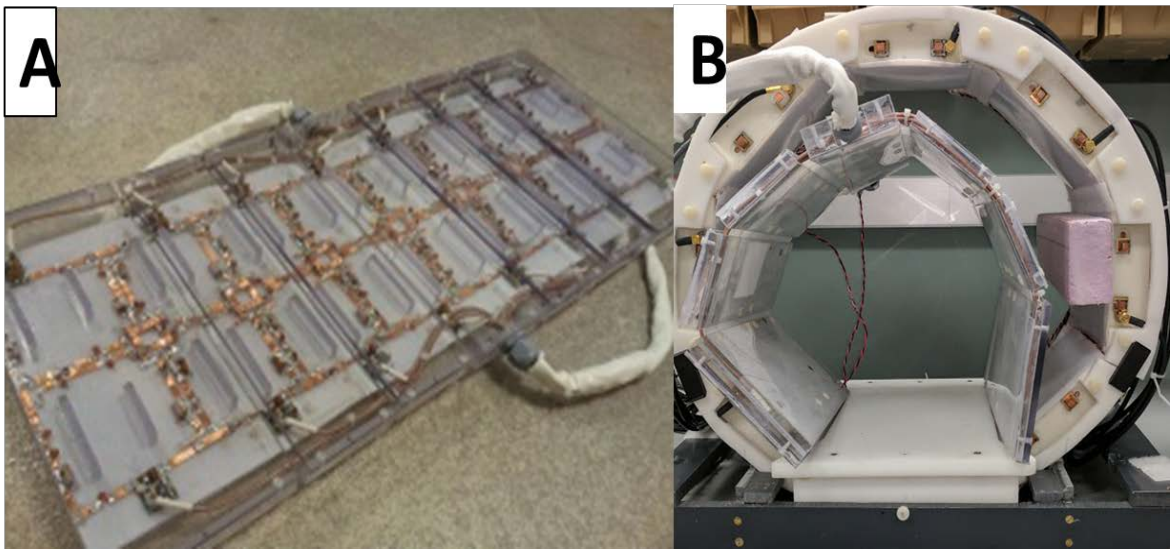

Figure 3.3 A. Sixteen channel receive only insert array; B. TTT transmit only coil and receive only insert coil system.

3.2.2.3 MR Imaging Experiments: All MR imaging studies were performed on a 7T human scanner (Magnetom: Siemens Medical Systems, Erlangen, Germany) approved by the institutional Internal Review Board. Four normal healthy volunteers were recruited and scanned.

3.2.2.4 MR Sequence Parameters: A 2D B_1^+ field map was acquired with a modified turbo flash (TFL) sequence [119]. *B_1^+ 2D Turbo flash Sequence:* Slice Thickness: 3mm, TR/TE: 13300/3.13, No. of Avg: 1, No. of phase encoding steps: 96, Pixel bandwidth: 491, FA: 83, TA: 00.56 min, FoV: 300*300, Resolution: 0.320 pixels per mm, Voxels size: 3.1x3.1x16.50 mm.

G factor: TR/TE: 10/2 ms, FA: 10^o, Acquisition Matrix: 128 x 128, FOV: 332 x 332, Voxel size: 2.6 x 2.6 x 2.6 mm^3, Slice thickness: 2.59 mm.

T1 VIBE: TR/TE: 5/1.48 ms, FA: 26.5^o, Pixel bandwidth: 488, FOV: 226x330 mm^2, Acquisition matrix: 176 x 256, Voxel size: 1.3 x 1.3 x 3 mm^3 and slice thickness: 3 mm.

3.2.2.5 Experimental and simulation calculations: Intensity values (calculated and experimentally measured values) were analyzed using MRIcron [120]. Mean B_1^+, B_1^+ in uT/V, and B_1^+ in uT /1W input powers in the experiment and simulations were calculated/measured. Total voltage was also calculated/measured in order to achieve 180° flip angle with 1 ms pulse width. In-vivo and simulated B_1^+ slices of the body and the spherical body phantom were loaded into ImageJ [121], then mean B_1^+ intensities were measured in each slice in the region of interest (liver tissue).

<u>For simulations and experiments:</u>

$$\text{Mean } B_1{}^+ = \frac{Area * mean}{Area} \qquad \textbf{(1.2)}$$

To have 180° flip angle with 1 ms pulse width:

$$\alpha = \gamma * B_1 * t_p \qquad \textbf{(1.3)}$$

$$\pi \quad = 267.513E6 * {B_1}^+ * \frac{1}{1000}$$

$${B_1}^+ = 11.744\mu T$$

In order to calculate the B_1^+ field in the $\mu T/V$ in simulations, *Vsim* is obtained from FFT pulse amplitude at 297 MHz, as calculated by FDTD simulation.

Scaling to $\mu T/$:

$${B_1}^+ = \frac{\text{Mean } {B_1}^+ * \mu_0}{Vsim * \sqrt{2}} \quad \textbf{(1.4)}$$

In order to calculate B_1^+ in $\mu T/V$ in the 7T experiments, voltage per PTX channel was given by the equation below:

$$Voltage\ per\ channel = System\ Voltage * \frac{FA}{180} * \frac{1000}{Duration}$$

(1.5)

Since there are eight transmit channels in our PTX configuration,

$$Total\ Voltage = Voltage\ per\ channel\ * 2\sqrt{2}$$

(1.6)

The above calculated total voltage can achieve a resultant FA based on mean B_1^+ intensity. In order to calculate the total voltage required to achieve 180° (11.7 uT):

$$V\,exp = Total\ Voltage\ *\ 180\ /\ Resultant\ FA$$

(1.7)

Scaling to $\mu T/V$:

$$B_1{}^{+} = \frac{\text{Mean } B_1{}^{+} * \mu_0}{Vexp * \sqrt{2}} \quad \textbf{(1.8)}$$

For simulation and experiments:

1W input power represents 10V input as shown below:

$$1W = \frac{V^2}{2Z} \rightarrow V = \sqrt{100} = 10V \quad \textbf{(1.9)}$$

3.2.2.6 Geometry (G) Factor: A G factor map (G-map) was acquired to evaluate the feasibility of parallel MRI in a rectangular phantom similar to the shape of the human abdomen/body. A 3D Gradient echo sequence was utilized with an acceleration factor (R) from 1 to 4 in the anterior to posterior (AP) direction in a transverse plane, right to left in the coronal plane and head to feet in the sagittal plane. The G-map was calculated using the following equation:

$$G - Map_{(x,y,z)} = \frac{SNR_{(x,y,z)R=1}}{\sqrt{R} * SNR_{(s,y,z)(R=1,2,3,4)}} \quad \textbf{(1.10)}$$

where SNR (x,y,z) is the SNR map of the MR images; and x, y, and z represent locations in the Cartesian coordinate system.

3.3 RESULTS

3.3.1 RF Coil Evaluation

3.3.1.1 Scattering Parameters: The S parameters were measured on the spherical body phantom using a vector network analyzer (Agilent, USA) and numerically calculated using an in-house FDTD package. The S11 mean of all array channels was experimentally measured approximately ~ -14dB in experiment (A/B/D/E) and ~18dB in simulation (G/H/J/K). Also, the TTT coil sides were highly coupled between opposite elements, as seen in the Figure 3.4C/F/I/L. Figure 3.4 shows the simulated compared to bench measured S parameters for a single coil side (2x2 as seen in Figure 3.2A) out of the eight coil sides. The results show good agreement between the experimental and simulated data.

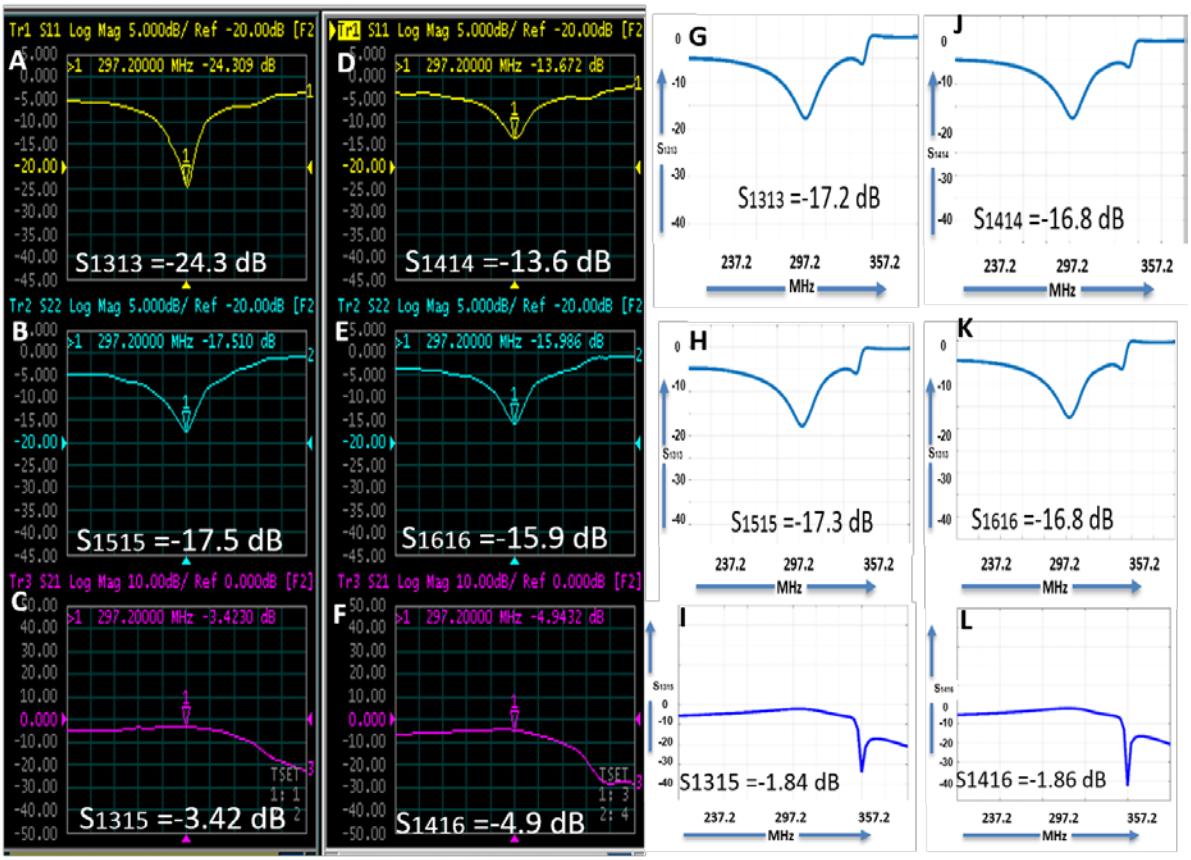

Figure 3.4 Experiments and Simulation scattering parameter comparison. A/B/D/E (Experiment) and G/H/J/K (Simulation): Reflection coefficient of Port 13, 14, 15 and 16, respectively; C/F (Experiment) and I/L (Simulation): Transmission coefficient of Port 13/15 and 14/16, respectively.

3.3.1.2 Coupling Matrix for One Coil Side: All thirty-two ports of the Tx coil were tuned and matched to 50 ohms. When loaded with different human subjects, these scattering matrix values changed very insignificantly due to the inherent highly coupled behavior. A coupling matrix for a single element out of all eight elements is presented in Figure 3.5 (TX coil).

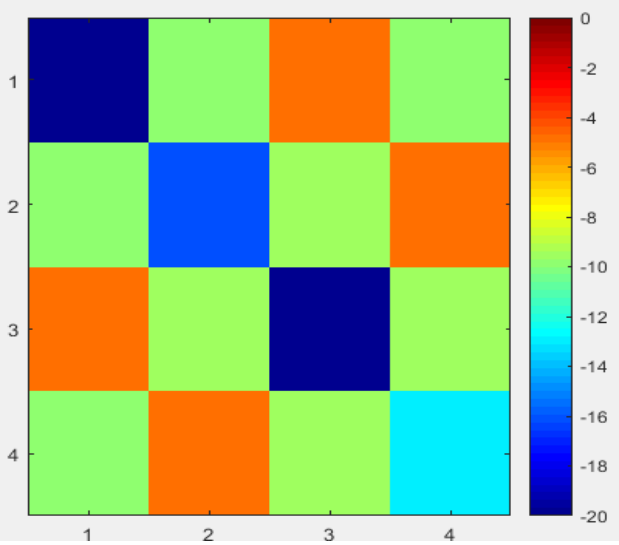

Figure 3.5 Coupling Matrix for a single coil side (2x2) out of the 8 sides.

3.3.1.3 B_1^+ Field Distribution: Spherical Body Phantom: Figure 3.6 shows the B_1^+ field maps obtained from experiment and simulation shown in slices across the spherical body phantom. Three slices were taken at three different locations, as shown in group 1, 2, 3 and 4, being sagittal, axial and coronal, respectively, in Figure 3.6. The numerical and experimental results are in good agreement, as shown below. The relative intensity values are marked on the spherical body phantom simulations as well as the experiments at comparative locations where the intensity was scaled from 0 to 1. The four locations are marked with yellow arrows in Figure 3.6. The relative intensity values of 0.50, 0.96, 1 and 0.42 for experiments show excellent agreement with the simulation numerical values of 0.48, 0.92, 1 and 0.51, as shown in Figure 3.6.

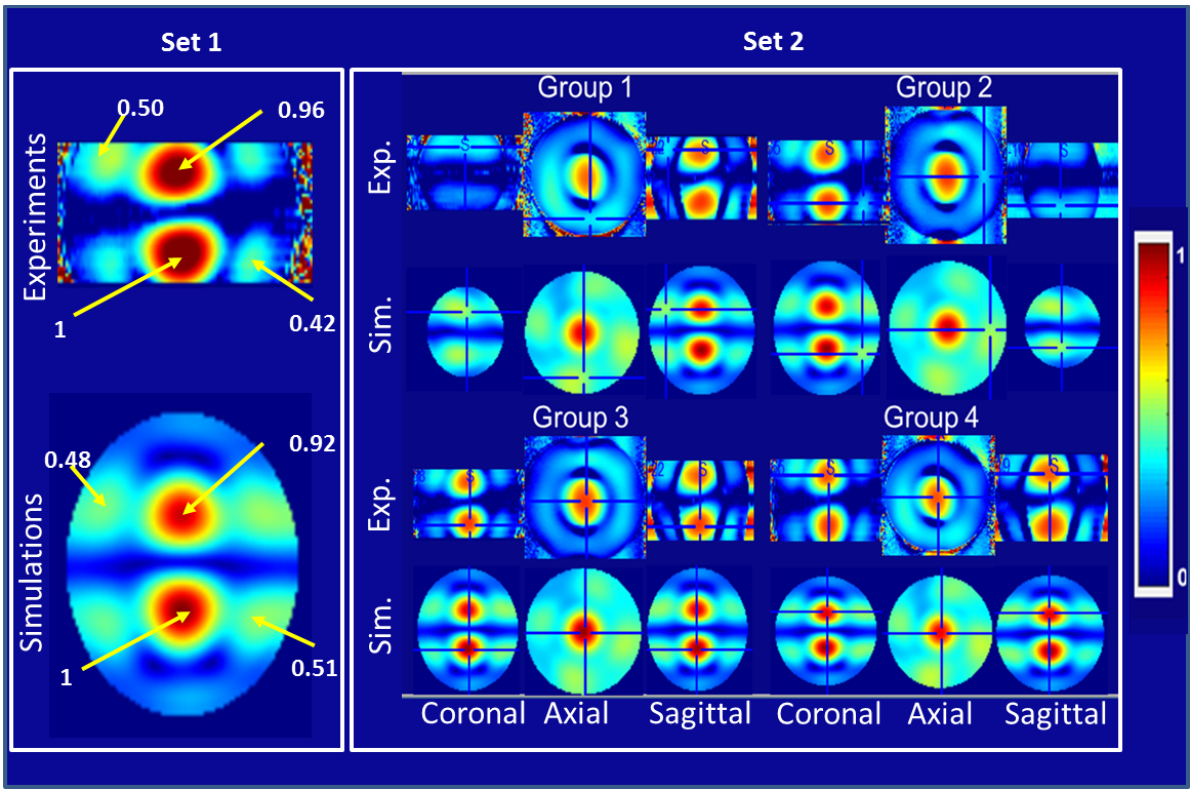

Figure 3.6 Experimental vs Simulation B_1^+ field comparison of spherical body phantom. Set 1 shows the relative intensity values on phantom simulations as well as experiments at comparative locations. This figure shows four slice locations as Group 1, 2, 3 and 4, with each group showing three slices sagittal, axial, and coronal. (Note, the body spherical phantom is Model: 2135650, Weight: 25lbs, Content: NiCl2 * H20, H20, GE Electric Company- Dielectric Corp, USA).

3.3.1.4 Human Body B_1^+ Field Distribution: As per the equations given in the Material and Methods section, the following are the calculations for Mean B_1^+, B_1^+ in $\mu T/V$, and then results scaled to 1W input power. This section also calculates the total voltage required to flip 180 degrees in the case of simulation and experiments. As mentioned earlier, ImageJ was used to find out the Mean B_1^+ for each slice, then equation 1.1 was used to calculate the resultant mean B_1^+ field intensity using equation 1.2.

For the experimental measurements, equation 1.5 indicates that voltage per Tx channel (total of 8 channels) is calculated as follows:

$$Voltage\ per\ channel = System\ Voltage * \frac{FA}{180} * \frac{1000}{Duration}$$

$$Voltage\ per\ channel = System\ Voltage * \frac{90}{180} * \frac{1000}{500}$$

= 152 V where the System Voltage is 152V.

$$Total\ Voltage = Voltage\ per\ channel\ * 2\sqrt{2}$$

= 428.6 V

The above calculated total voltage can achieve a mean flip angle in the liver region = 35.5°. In order to calculate the total voltage required to achieve 180° (11.74 μT), equation 1.7 is used as:

428.6 => 35.5

Vexp? => 180

Vexp = 2173 V

Scaling to $\mu T/V$, the mean B_1^+ field intensity in the liver = 11.74/Vexp = 0.0054 $\mu T/V$.

Scaling to 1W input power, the mean B_1^+ field intensity in the liver = 0.0054*10 = 0.054 μT per 1W input.

For the simulations**:**

Scaling to $\mu T/V$, the mean B_1^+ field intensity in the liver = 0.0074 $\mu T/V$.

Scaling to 1W input power, the mean B_1^+ field intensity in the liver = 0.0074*10 = 0.074 μT per 1W input.

The total voltage required to achieve a mean flip angle of 180° (11.74 μT) = 11.74/0.0074 = 1587V

The resultant difference between the simulation and experimental voltage = 36.9%. Part of this loss can be accounted for as the RF chain includes connections from the coil/PTX plug (from table header to the beginning of the splitters), splitters, and TR switches, resulting in a measured plug loss of 11%. Second, from the beginning of the splitter all the way to the excitation ports of the coil, the loss was measured to be 12%. The rest of the loss (13.9%) can be attributed to the TR switches as well as the coil losses.

Figure 3.7 shows the simulated B_1^+ field distributions in the axial, sagittal, and coronal slices. Figure 3.8 shows the in-vivo B_1^+ field distribution in the whole body, covering the liver from beginning to end. The calculated COV from mean and standard deviation is 31% in the simulations. The experimental COV is 28%.

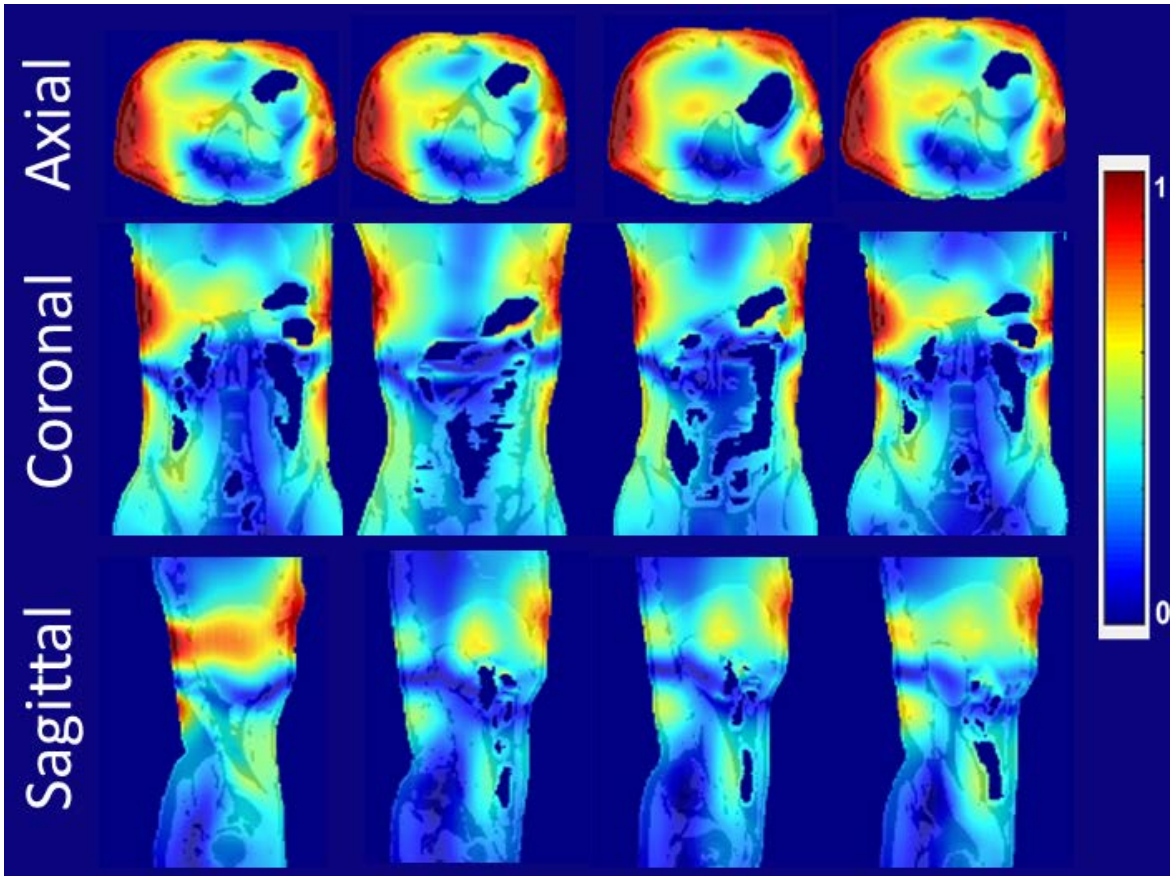

Figure 3.7 Simulated B_1^+ field distributions. Four slices are shown in axial, sagittal and coronal views. Segmentation of the liver location is also shown.

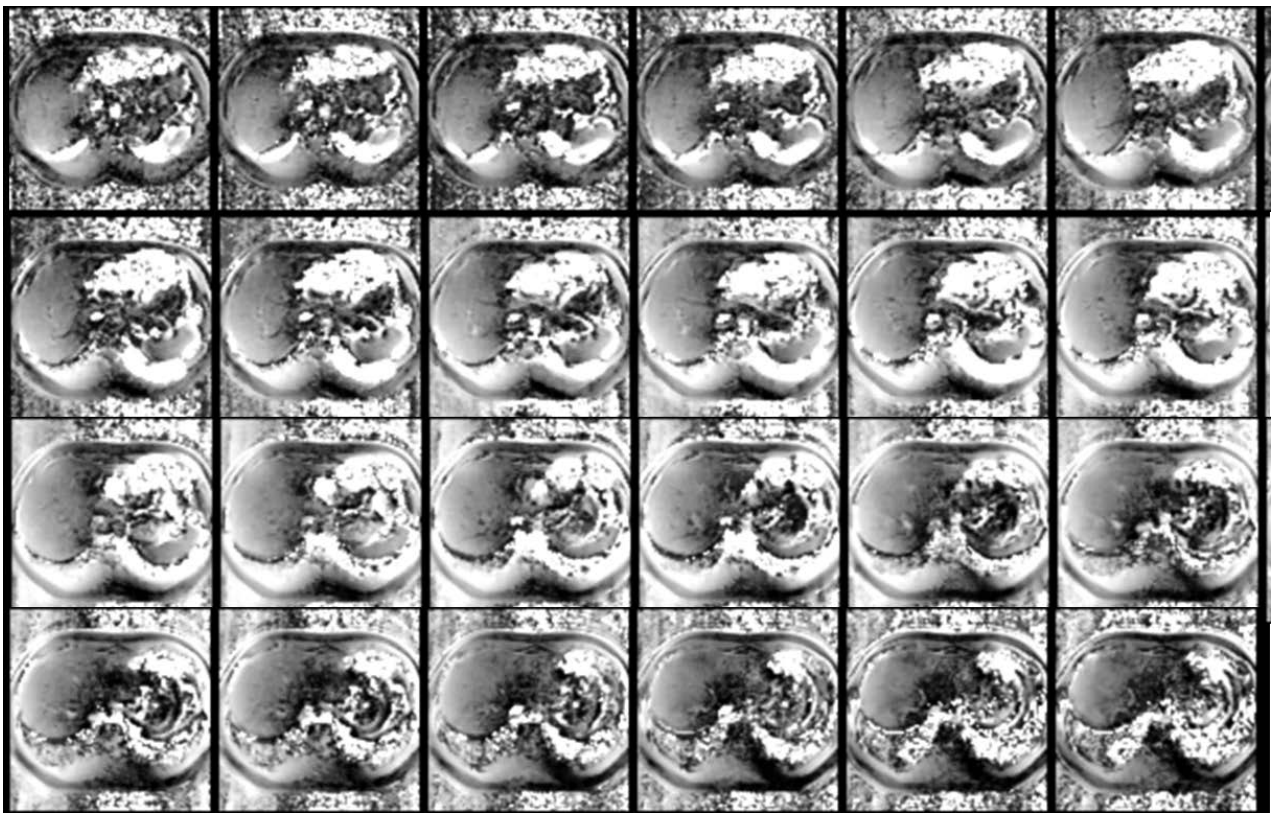

Figure 3.8 In-vivo B_1^+ field distribution for the transmit-only coil.

3.3.1.5 SAR: As per IEC guidelines, numerical calculations were carried out using an in-house FDTD method (6, 33). For 1W input power, the calculated average SAR was to be 0.0049 W/Kg/10g, with peak SAR at 0.11 W/Kg/10g and a total absorbed power of 22%. The average SAR per mean 2 μT was (0.11009/0.0049236) * (0.074) = 1.65 W/kg/10gm. Figure 3.9 shows the SAR the axial, coronal, and sagittal view in the liver and the whole body, respectively.

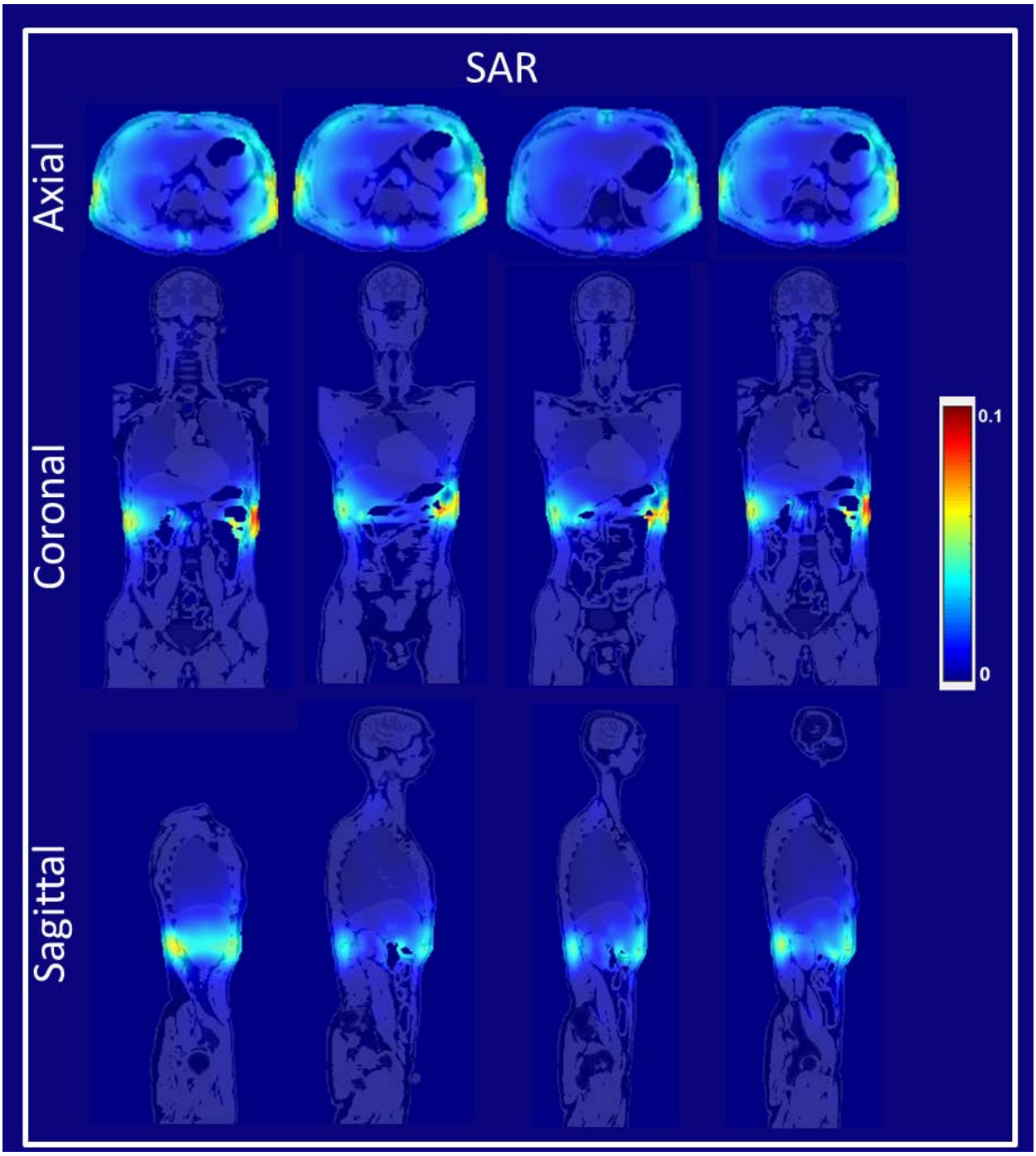

Figure 3.9 Simulated SAR is shown in four slices in the sagittal, coronal, and axial view. Note: It is overlaid with segmented anatomical structure.

3.3.1.6 Noise Correlation for Receive Only Array: All sixteen channels were tuned and matched to a minimum of -15dB reflection coefficient and -14 dB transmission coefficient. The receive array noise correlation was also measured, shown in Figure 3.10; these results show that good inductive decupling and preamplifier decoupling was reached.

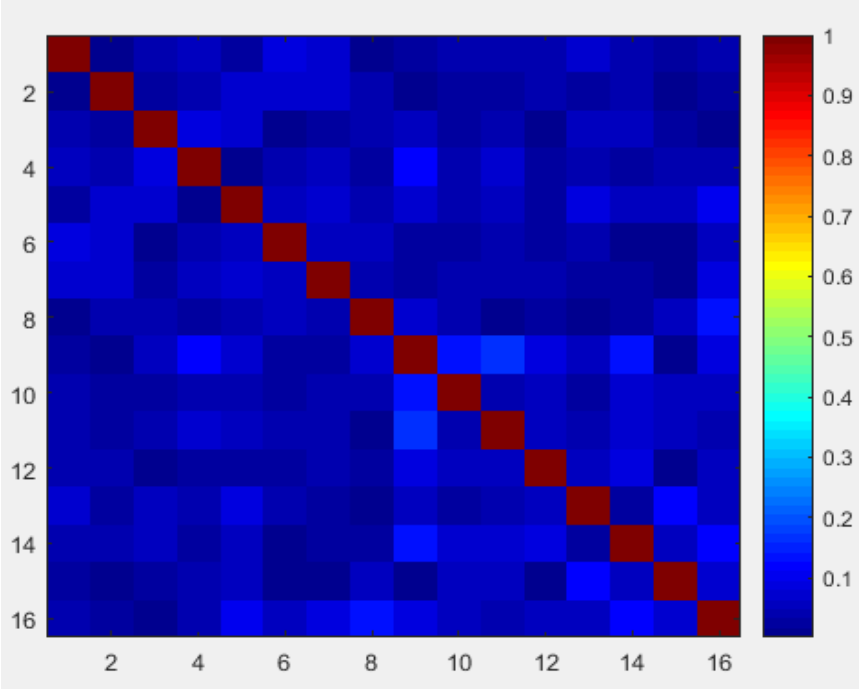

Figure 3.10 Sixteen-channel receive-only array noise correlation.

3.3.1.7 Geometry factor: The G-factor map demonstrates the feasibility of parallel MR imaging as well as depicts the image quality for respective acceleration factors (R). Figure 3.11 shows the three different acceleration factors R= 2, 3 and 4 with transverse (anterior-posterior), coronal (right-left) and sagittal (head-foot) marked on the left side. The mean G-factor increased in all three planes as the R increased.

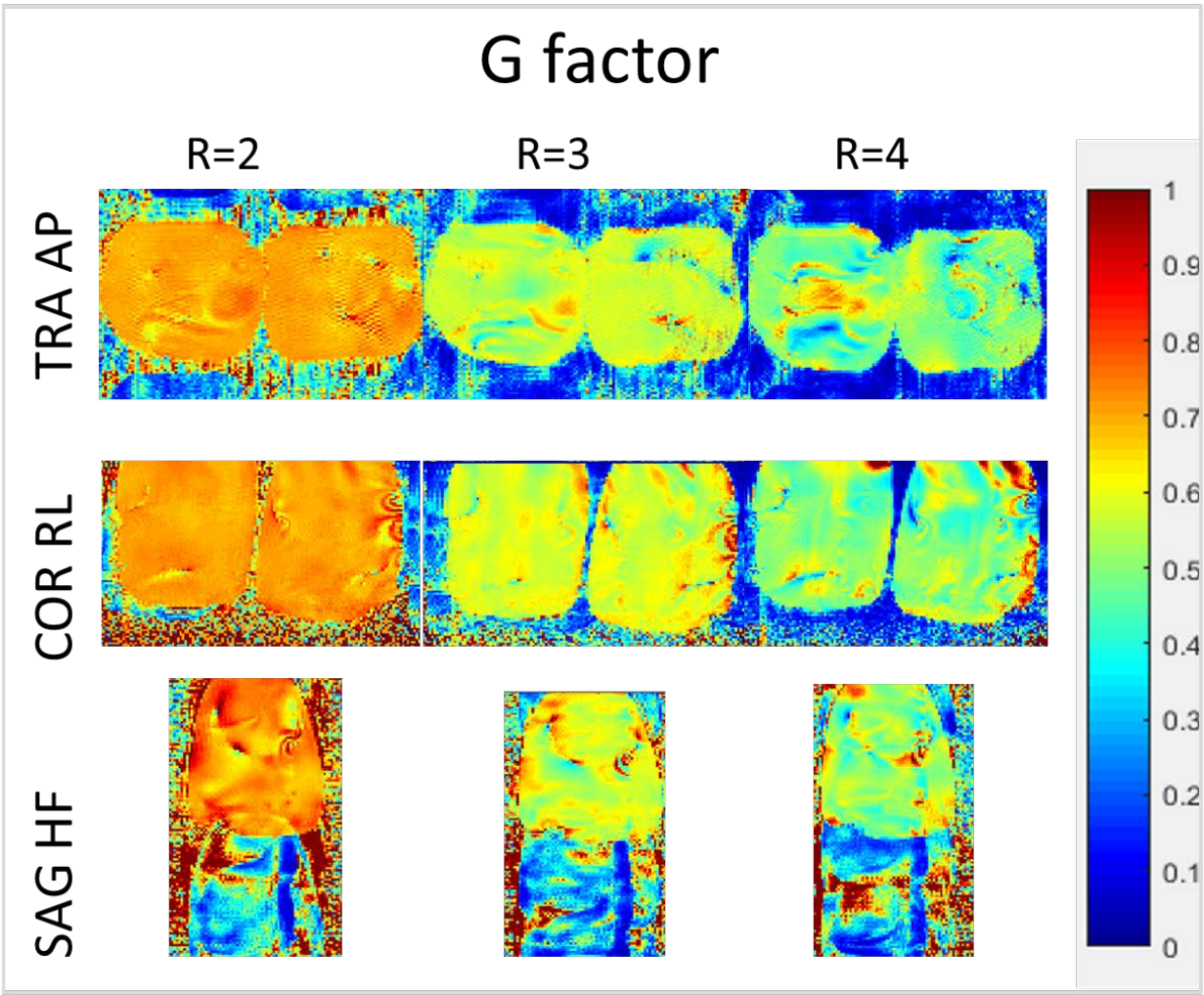

Figure 3.11 Experimental G-factor map in Sagittal (HF), Coronal (RL), and Transverse (AP) planes. The maps were calculated using a 3D gradient echo sequence with varying acceleration factors (R).

3.3.1.8 In-vivo Imaging: Signal to Noise Ratio with and without Receive Array: A T1 VIBE sequence was used to measure the SNR with and without a receive array. The SNR was measured in all the slices starting from the beginning of the liver to the end of liver in the abdomen. The SNR was ~3 to 3.5-fold higher compared to without an Rx receive array in the abdomen as well as the liver, as shown in Figure 3.12 and 3.13. This shows a significant improvement due to the sixteen-channel Rx receive array in the high resolution T1 VIBE (Figure 3.14, and 3.15). A significant SNR increase was observed around the periphery of the abdomen, as well as good RF penetration as shown in Figure 3.14 and 3.15. The in-vivo experimental data show promising results in the liver (portal vein and its branches, inferior vena cava and it's branching veins), and kidney (first and second order renal artery) of the human body, overcoming the severe RF penetration issues and undesired signal voids normally encountered with body imaging at UHF (7T).

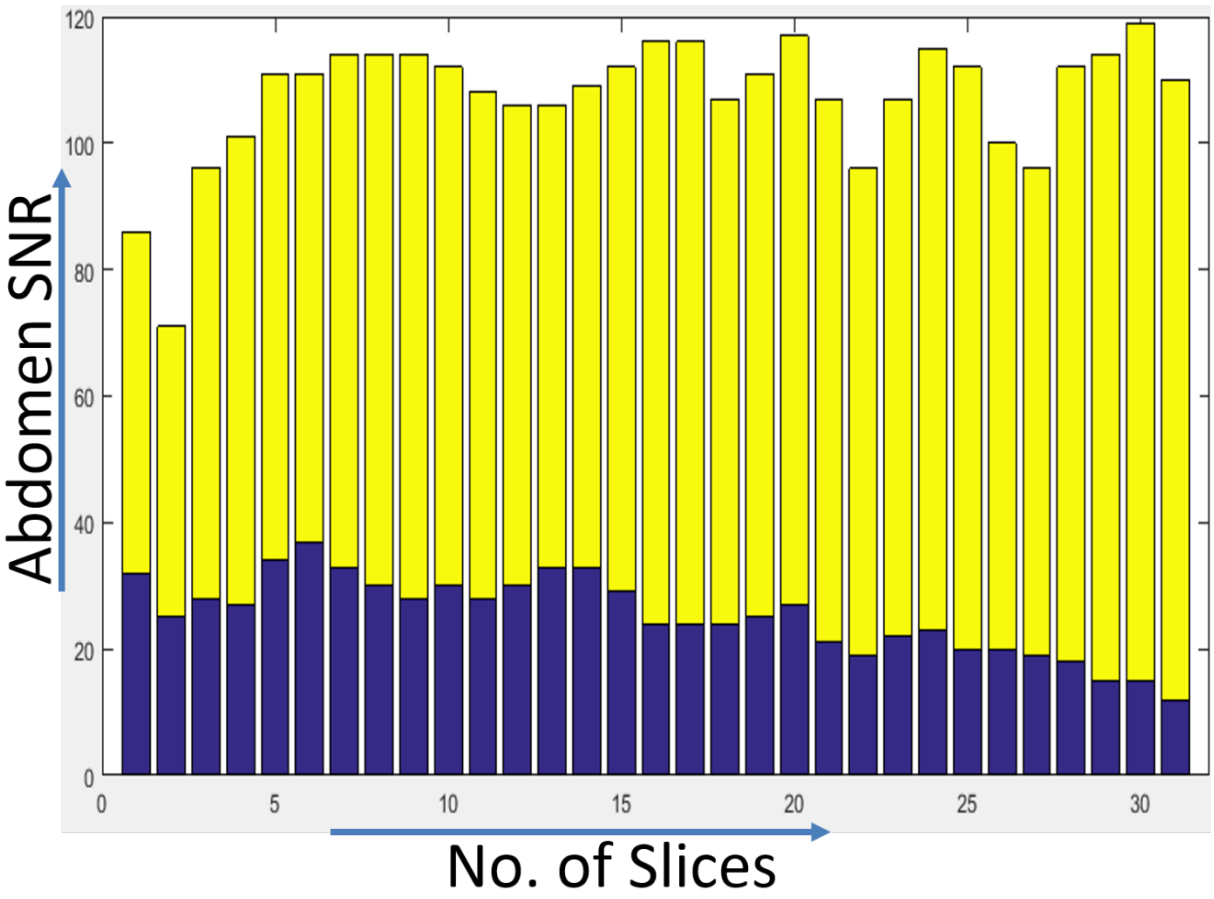

Figure 3.12 SNR in the abdomen with T1 Vibe scans with (yellow bars) and without (blue bars) receive-only array.

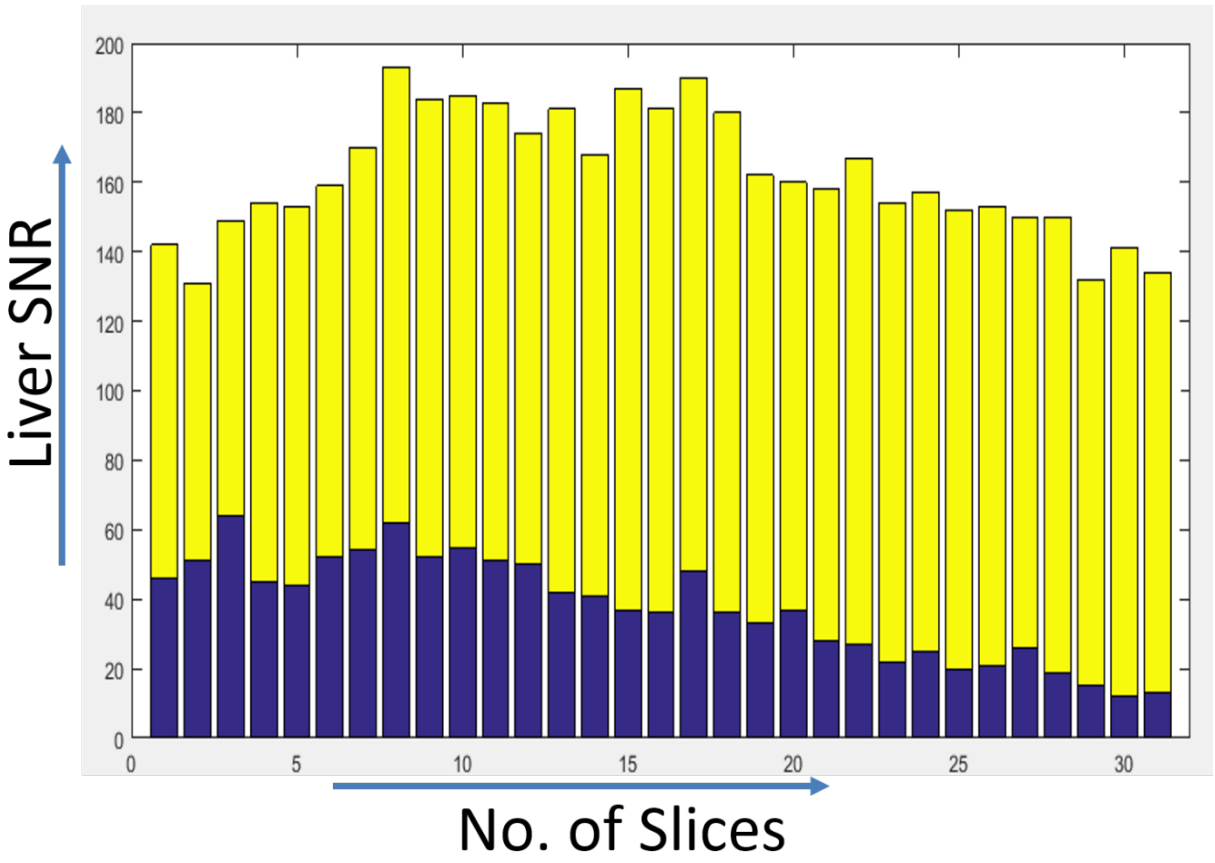

Figure 3.13 SNR in the liver with T1 Vibe scans with (yellow bars) and without (blue bars) receive-only array.

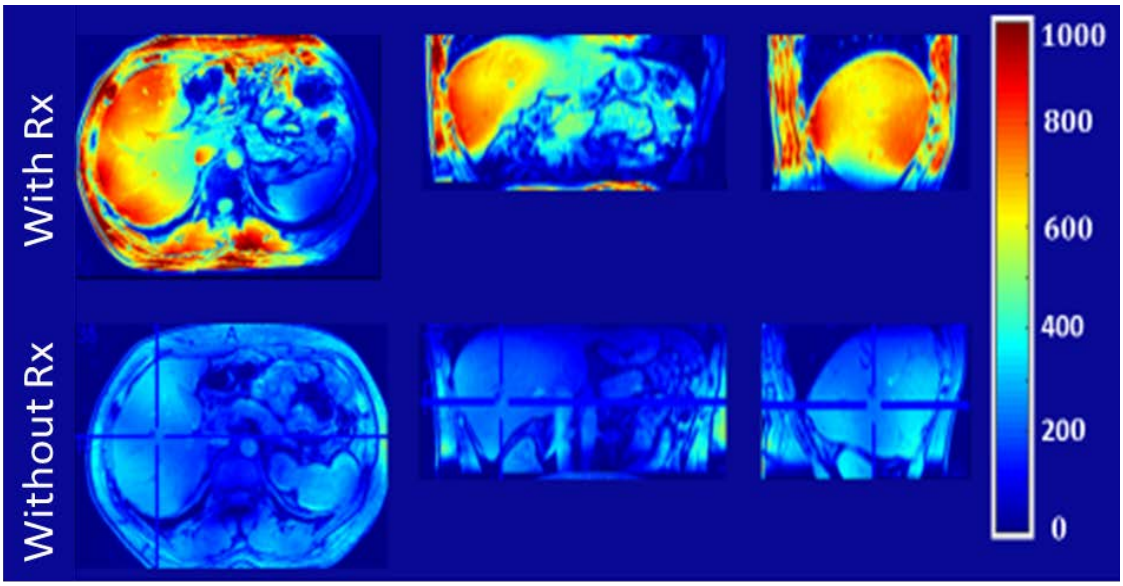

Figure 3.14 Whole-body T1 Vibe image (single slice) showing SNR obtained using the 32-ch TTT Tx with and without 16-ch Rx whole body coil. The scans were obtained with and without receive only coil.

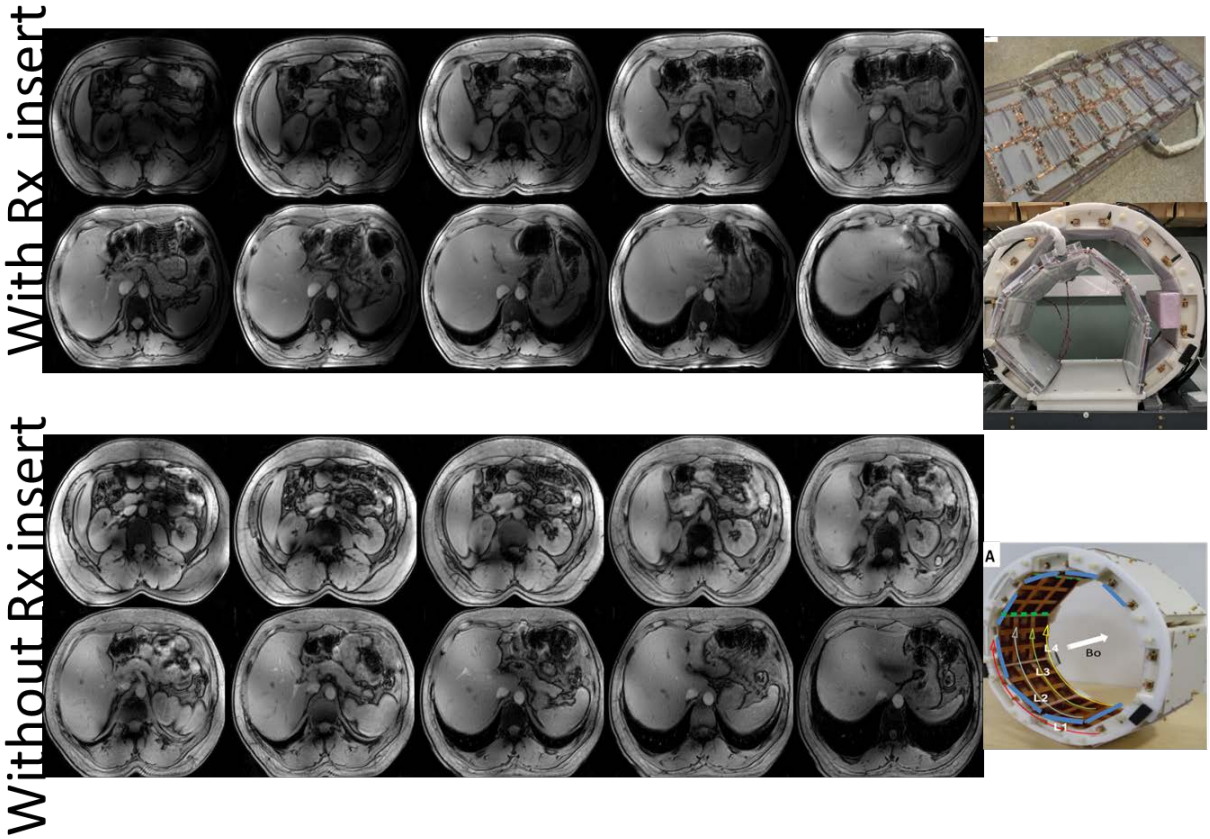

Figure 3.15 Whole-body T1 Vibe images (Complete liver covering slices from beginning to end) obtained using the thirty-two channel TTT Tx whole body coil. The scans were obtained with and without (using the body coil as receive coil) receive only coil which is shown on right side.

3.4 DISCUSSION

A newly developed Tx coil with receive-only array was presented at 7T MRI. The numerically calculated S parameters were matched to experimentally measured values for both the reflection and the transmission coefficients. This was necessary in terms of evaluating the electromagnetic fields during the RF coil development, as shown in Figure 3.4. Figure 3.5 shows a good transmit coupling matrix for the Tx-only coil. Figure 3.6 shows the numerical and experimental results at relative intensity values to be in good agreement. Figure 3.7 and 3.8 show simulation B_1^+ field distributions and in-vivo B_1^+ field distributions in the whole body, covering the liver from beginning to end, where COV is 31% in simulation and 28% in experiment. The calculated total voltage to achieve 180° FA was 1587 V in the simulations and 2173.4 V in the experiments, with a difference of 36.9%, where 11% is from plug loss, 12% is measured from beginning of the splitter after the plug to the coil excitation port, with a resultant 13.9% being the difference between the simulations and experiments. Figure 3.9 shows the SAR in the axial, coronal, and sagittal view in the whole body.

Figure 3.10 shows that the Rx receive-only array noise correlation demonstrated good inductive and preamplifier decoupling. The G-factor map presented in Figure 3.11 shows the feasibility of parallel MR imaging while showing that image quality decreases for R=3 and 4. In-vivo imaging of the liver/abdomen showed ~ 3 to 3.5 fold increase in SNR gain when comparing Rx to without Rx as shown in Figure 3.12 and 3.13 at 7T. In Figure 3.14 SNR increases are

demonstrated clearly in the whole body slices plotted using MRIcron [120]. The physical size of the abdomen is 4-6 times larger than one electrical wavelength (~12 cm) at 300MHz, which usually creates complex non-uniform wave behavior in ROI, but this was addressed using a circularly polarized phase only scheme as demonstrated in Figure 3.14 and 3.15. Also, the volunteer in-vivo images in Figure 3.14 and 3.15 show the reproducibility and robustness of a Tx-Rx coil. If needed, the developed Tx array can also be used in a pTx mode, where amplitudes and phases can be optimized in order to further improve B_1^+ field homogeneity and/or SAR. The in-vivo images show excellent anatomical detail in the liver and abdomen where the receive coil is located, as shown in Figure 3.14 and 3.15. Also, the stomach region doesn't benefit from a receive coil as much as the liver because the receive coil only covers a limited region, not the entire area, as shown in Figure 3.15.

The TTT Tx coil has an inductance where the coil geometry and its corresponding dimensions define the total inductance which might not be low enough to tune the Tx coil to 297.2MHz (7T UHF MRI). There are a few parameters that can help to tune the coil to the frequency of interest (297.2MHz), such as adding a capacitor to increase the capacitance and changing the copper rod thickness or coil channel dimensions to increase the inductance. Those changes would shift the frequency to the desired frequency of interest (297.2 MHz) at 7T UHF MRI. One of the advantages of the design presented here is that the coil element size can be increased or decreased such that it can be either circular as presented or elliptical for future configurations. In both cases, it can be tuned to 297.2 MHz without any difficulty. A highly coupled coil reduces the load dependency, which in turn doesn't require adjustment of tuning or matching or shimming per subject either in single or parallel Tx mode, resulting in optimum

performance. Also, rigorous full wave simulation helps in choosing the correct coil array dimensions since the resonant frequency is defined by the geometrical inductance of coil.

This full wave simulations are also important since it helps in predicting the electromagnetic fields during the coil development and evaluation. One of the future challenge is to produce a higher B_1^+ field towards the center of the abdomen using either the existing circularly polarized strategy or other optimized shimming configuration. Also, a higher RF power can be used to increase B_1^+ field while keeping the SAR under acceptable FDA limits since SAR is the only parameter which puts a limit on how much power can be applied. Tian et al [101] reports peak 10gm SAR values well within IEC limits, listing various TEM configurations in addition to loop array and birdcage design. Dieringer et al mentioned that averaged partial body RF exposure was less than 1.4 W/kg (IEC: 4W/kg, 1st level) in [122]. Alon et al [123] and Vaughan [124] also reported average SAR values less than 2W/kg for the whole body, the limitation set by the IEC. Also, high density coil designs like a 64- or 128-channel array would provide a higher degree of B_1^+ manipulation. This would help in lowering B_1^+ areas and optimizing the ROI, which leads us to the next step of focusing on exploring a high density Tx-Rx coil (as mentioned earlier) and the use of RF shimming for obtaining better uniformity in whole body imaging. In spite of existing B1+ field inhomogeneity challenges, the proposed coil design has shown to be highly beneficial in attaining good RF penetration in various parts of the abdomen and torso.

3.5 CONCLUSION

In this study, an RF array system with a thirty-two channel Tx-only TTT array was combined with a sixteen channel Rx-only array for whole body MRI at 7T. This study also includes a B_1^+ profile in a spherical body phantom simulation as well as in an experiment that shows excellent correlation using a thirty-two channel Tx only configuration, which shows the accuracy of FDTD prediction. Noise correlation showed good isolation and the G-factor map demonstrated the feasibility of parallel imaging. Also, 7T in-vivo imaging with and without the Rx only insert array showed increases in SNR by 3 to ~3.5 (compared with Tx-only coil utilized as a transceiver). 3D T1 VIBE images were acquired successfully with excellent anatomical detail. Future work will include study of a higher density Tx only array, Rx only array, distinctive RF shimming strategy, and clinical evaluation using various pulse sequences to get high spatial/temporal resolution in-vivo images at 7T UHF MRI.

4.0 DESIGN AND DEVELOPMENT OF ULTRA-HIGH FIELD RADIOFREQUENCY COIL DEVELOPMENT FOR EVALUATING UPPER EXTREMITY IMAGING APPLICATIONS

4.1 INTRODUCTION

As we discussed in the background chapter, MRI is a favored imaging modality for soft tissue imaging (with or without contrast) for a wide range of upper extremity pathologies including diagnosis and monitoring of several medical conditions. These include acute trauma and sports-related injuries; occult fractures; peripheral neuropathy [125]; sporadic inclusion body myositis [126]; inflammatory (muscle) myopathies [127]; nerve entrapment syndromes [128]; soft tissue dystrophic lesions and avascular necrosis [129]; and cartilage [130], tendon, and joint conditions (oedema, synovitis, dactilytis, and enthesis) [131]. Most upper extremity MR procedures are currently performed at field strengths of 1.5T and/or 3T. Compared to the Food and Drug Administration (FDA) currently approved clinical systems at1.5T and 3T, systems at 7T can enhance some of the upper extremity clinical applications. These include i) sequential monitoring of regeneration after peripheral nerve (PN) repair [132, 133] which is critical for evaluation of re-

innervation and in planning treatment strategies, and ii) monitoring outcomes after vascular interventions [134] without the need for contrast agents.

At this point, MRI imaging at ultra-high fields (UHF ≥7T) remains an investigational modality. Higher field strengths could theoretically augment resolution but the primary challenges of UHF imaging include problems similar to encountered at 3T, but at a more intensified level. These include inhomogeneities in the B_1^+ field (circularly polarized component of transverse magnetic field that excites the spins) distribution, elevated radiofrequency (RF) power deposition affecting local and global SAR, and chemical shift and other tissue contrast issues. All these aspects affect image quality and require specific improvements to UHF hardware design and imaging protocols [6, 27, 37, 135, 136]. Optimization of UHF upper extremity technology and pulse sequences can improve the role and relevance of 7T MRI in imaging of soft tissue (muscle, vessel, nerve, cartilage, ligament and tendon), bone (trabecular and bone marrow characteristics) anatomy, and contextual structures [137]. To date, prior and ongoing clinical focus on UHF imaging has been in brain applications as opposed to human torso and extremities (except the knee [18, 138, 139]).

In this work, we describe a design for an upper extremity RF system composed of a transverse electromagnetic (TEM) resonator Tx coil in conjunction with an eight-channel receive-only insert array. We comprehensively evaluate the performance of the proposed RF coil system with experimentally measured and numerically calculated B_1^+ maps as well as SAR. We investigate a wide variety of imaging sequences including: T1 VIBE (T1 weighted volumetric interpolate breath-hold exam), T2 DESS (T2 weighted double-echo steady state), T2* SWI

(susceptibility weighted imaging), TOF (time-of-flight) and DTI (diffusion tensor imaging) on a 7T human MRI scanner. We also compare images obtained at 7T (using the designed RF coil system) and at 3T (using a commercially available eight-channel extremity coil).

4.2 MATERIALS AND METHODS

The Tx-only and receive-only approach offers the following distinct advantages:

1. The TEM coil design acts as a multi-conductor transmit coil. With a distributive type of capacitance, it is easier to separate the resonant modes and adjust the B_1^+ field distribution for better homogeneity over the region of interest [59, 60].
2. The high-density eight-channel receive-only array can provide excellent SNR, and CNR. In addition, the receive coil can be tuned and matched such that it can be used for forearm, elbow, wrist and finger imaging.

4.2.1 Transmit Coil Design

Given the low filling factor of the arm/hand, a shielded design of an actively detuned TEM resonator [56, 60] was adapted using 8 struts arranged along a concentric circle, as shown in Figures 4.1A and 4.1B. The inner and outer struts were separated by a dielectric sleeve (Teflon filling) as shown by arrows in Figures 4.1A and 4.1B. In conjunction with a conductive cylinder, this created a transmission line mechanism with the struts as inner conductors and the cavity wall

as the outer conductor (inner/outer diameter of the cavity = 7.5/10.0 inch). The inner struts were electrically connected to the front and back end shield plates while the outer struts were electrically isolated by a small gap (0.5 inch) from the end shield plates. The coil (Figure. 4.1C) was tuned by pulling/pushing the inner struts in and out of the cavity resonator. This ultimately changes the capacitance between the inner and outer struts and therefore tunes the coil's mode of interest to 297.2 MHz. The system utilized an in-house made quad-hybrid for producing quadrature excitation. Other design parameters are shown in Table 4.1.

Table 4.1 TEM UHF Transmit Coil Design Parameters (See Figure. 4.1)

Design Parameter	Dimension
Outer strut diameter (Dos)	0.5 inch
Inner strut diameter (d)	0.25 inch
Teflon filler outer diameter (Dd)	~0.5 inch
Distance from the center of the coil to the center of the outer strut (Lc)	3.75 inch
Length of inner strut inside the cavity (Los)	~ 3-4 inch
Relative dielectric constant of Teflon (ε_r)	2.1
Distance from center of the outer strut to the outer conductor shield	1.25 inch

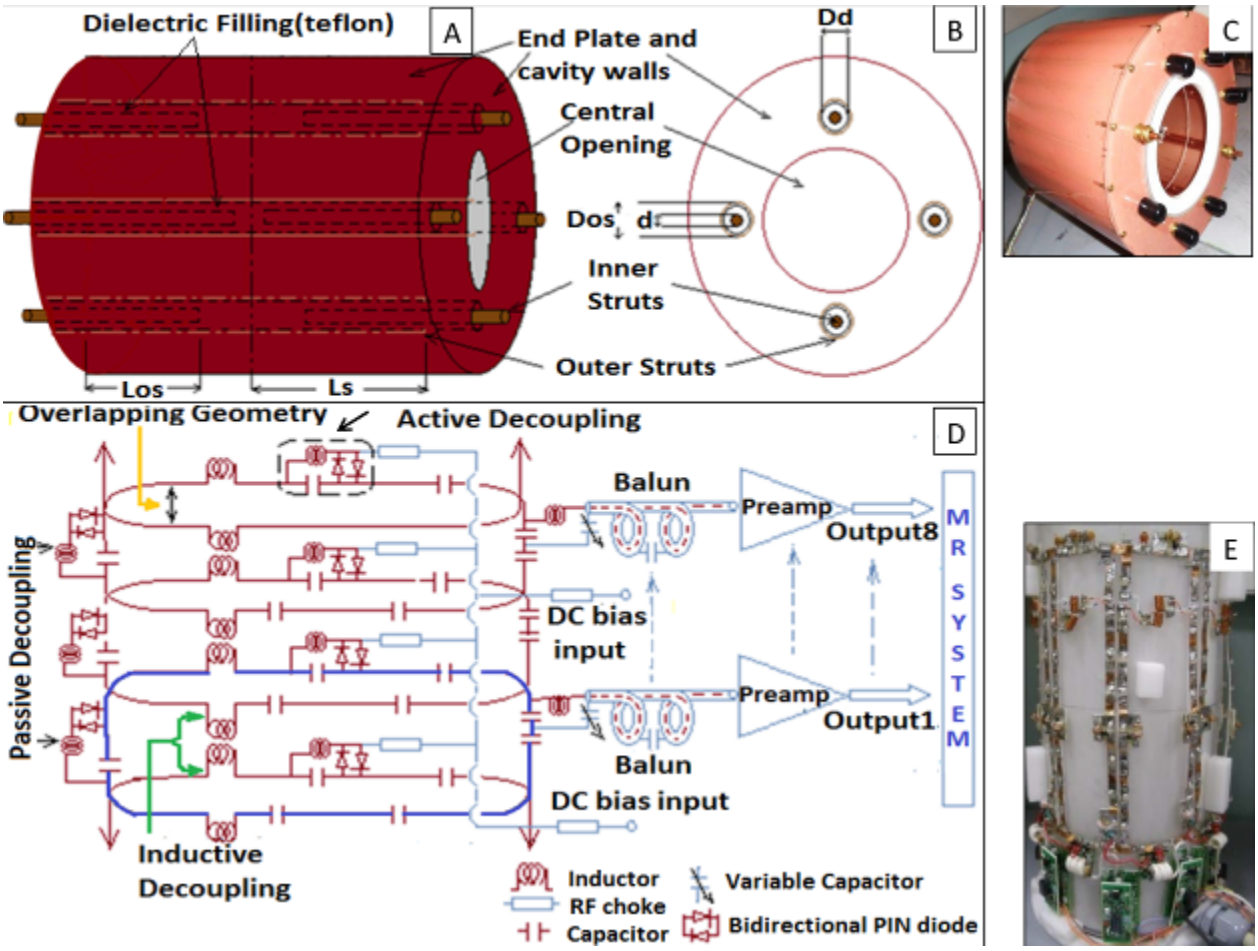

Figure 4.1 Transmit coil design and receive only coil array

A: 8-element TEM resonator (four struts are shown for simplicity); B: Front plate of resonator (looking right to left); C: Picture of constructed transmit coil; D: Receive array circuit diagram showing single element (blue loop), overlapping geometry between adjacent loops (yellow arrow), inductive decoupling for no-adjacent neighbors (green arrows), passive decoupling for each loop element (two black arrows on left side), and continuation of rest of the loop elements (maroon arrows); and E: Picture of the eight-channel receive array.

4.2.2 Transmit Active Decoupling Method

As previously described [58, 140], the TEM elements were detuned by forward biasing with 100mA at 10V (as they are shunted to the outer conductor). During transmit mode, the coil functioned by reverse biasing PIN diodes (MA4P7446F-1091T, MA-COM, MA) with 30V. The selection of the PIN diode was based on stray capacitance, switching speed, and heat capacity (25W power dissipation). RF chokes of 5.8uH (J. W. Miller, CA, and Vishay, CT) were used to block the RF signal in the DC path, and5000pF American Technical Ceramics (ATC) capacitors were used for blocking DC in the RF path.

4.2.3 Receive Coil Design

In order to improve the SNR over the ROI (forearm and hand), eight inductively decoupled [141] surface loops (18 X 7 cm^2) were distributed evenly on an acrylic former (McMaster Carr, Elmhurst, IL). A 5-mm wide copper foil with evenly distributed circumferential capacitors (ATC, Huntington Station, NY, USA; and Passive plus, Huntington, NY, USA) was utilized to achieve tuning at 297.2 MHz (Figures. 4.1D, 4.1E). Figure 4.1D depicts a circuit diagram of three out of the eight loops, showing the overlapping geometry (yellow arrow), active (dotted rectangular marking) and passive (two black arrows) decouplers, balun and arrangement of the preamplifiers. Figure 4.1E shows the eight-channel receive array configuration.

4.2.4 Receive Decoupling Method

Neighboring elements were decoupled using overlapping (yellow arrow in Figure. 4.1D) distance to minimize mutual inductance. The sole use of this technique however restricts the geometrical layout of the array and is ineffective in minimizing coupling on the next nearest neighboring array. Therefore, inductive decoupling (as shown in Figures. 4.1D (green arrow) and 4.1E) and low impedance pre-amplifier decoupling through the use of a 'tank circuit' [141] were implemented to reduce coupling caused by non-adjacent loops. In addition to a passive decoupling circuit, each loop contains an active decoupling circuit (shown with black arrow in Figure. 4.1D) which turns ON (during transmit operation) using DC bias voltage from rhe MR system. This functionality is important for a combined transmit-receive system since the Tx coil's emitted electromagnetic waves could create significant voltage on the receive loops, damaging the receive preamplifiers (if the active decouplers do not properly function).

4.2.5 Finite Difference Time Domain Modeling

The growing demand for UHF technologies necessitates the use (in terms of design as well as evaluation) of full wave rather than low-frequency, lumped-circuit approaches. As the operational wavelength becomes closer to the RF coil dimensions and electrical size of the load, full wave analysis becomes essential in predicating the electromagnetic interactions between the tissues and RF coil [40]. In this work, the TEM volume resonator and the anatomically detailed human hand model were modeled as a single system (Figures 4.2A and 4.2B show a 3D view of the coil struts and side view of the human arm model, respectively) using the finite difference time

domain (FDTD) method. Our in-house FDTD package involved the modeling of the excitation sources using a transmission line model, which allows for accurate calculations of the coupling and the input impedance [37, 142]. MATLAB was used to create the grid of the resonator geometry. A 3D computational grid composed of 188x188x270 Yee cells [92] with spatial resolution of 1.58mm (dx=dy=dz) and temporal resolution of 3 $x10^{(-12)}$ sec (used to meet the Courants stability criteria [143]) was developed. The computational domain was surrounded by 32 perfectly matched layers (PML) placed on the top and bottom of the coil model and 12 PMLs surrounding the coil model (as shown in Figure. 4.2C) in order to absorb the electromagnetic waves radiated by the coil [114, 115]. The original 1mm Duke male model [144] (age: 34, height: 1.74 m, weight: 70 kg, body mass index (bmi): 23.1 kg/m^2) was rescaled to a resolution of 1.58x1.58x1.58 mm^3.

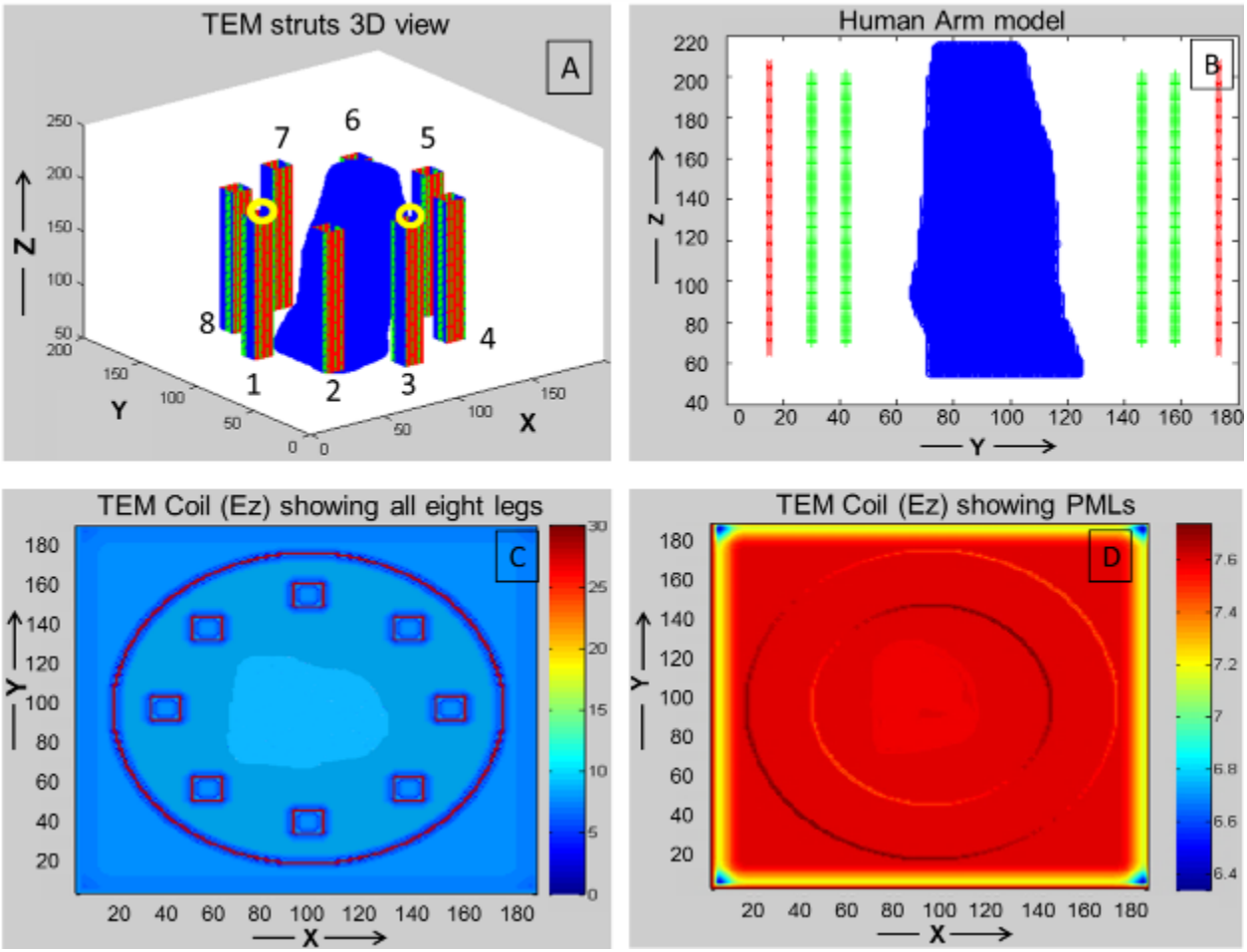

Figure 4.2 Coil and arm model as single system

A: FDTD model of TEM coil (excitation ports shown by yellow circles); B: Side view (YZ slice) with human arm model positioned inside TEM structure (showing struts in green, and shield in red); and C: Top view (XY slice) showing all 8 elements of the coil and locations of the PMLs.

4.2.6 RF Power and Specific Absorption Rate (SAR)

At UHF frequency, the most important safety concerns are local SARs and/or localized temperature rises. The RF power supplied to the coil can be approximately calculated as the sum of the radiated power (that escaping the coil without getting absorbed in tissue), the absorbed power (in tissue), the power lost through coupling and the power dissipated in the coil and RF shield [145]. Since tissue dissipation and RF heating concerns are associated with the power absorbed in tissue, we investigate the power absorbed in the human model. The total power absorbed is scaled to obtain a mean (in the ROI) and continuous B_1^+ field intensity of 1.957 μT, which is the field strength required to produce a flip angle of $\pi/2$ with a 3-ms rectangular RF pulse. The linearity of Maxwell's equation helps in calculating the absorbed power as Feed Voltage $\propto$ E $\propto$ H; and therefore, the absorbed Power $\propto E^2 \propto B_1^{+2}$, where E and H are the electric and magnetic field intensities, and $\propto$ indicates linear dependence. Therefore the absorbed power in a tissue of a given density from the Tx RF coil is described as SAR. In FDTD, the SAR as calculated utilizing our in-house FDTD package is:

$$SAR_{(i,j,k)} = \frac{1}{2}\frac{\sigma_{(i,j,k)}(E^2{}_{x(i,j,k)} + E^2{}_{y(i,j,k)} + E^2{}_{z(i,j,k)})}{\rho_{(i,j,k)}} \quad \textbf{(4.1)}$$

Where $\rho_{(i,j,k)}$ is tissue mass density (unit: kg/m^3), and σ(i,j,k) is tissue conductivity (unit: S/m) at the (i, j, k) location. Ex, Ey, and Ez (V/m) are the magnitudes of the electric field components in the x, y, and z directions, respectively. By summing the SAR from all tissues, an indication of the total power deposition can be obtained. SAR is presented in the unit W/kg per 10 gm of tissue by

continuously averaging a finite number of FDTD cells, which results in achieving an approximate average SAR value over any 10 gm of tissue.

4.2.7 Experimental Imaging Protocols

All the workbench measurements were performed using a calibrated vector network analyzer (Agilent E5062A ENA series, CA, USA) together with a multi-port S parameter test set (87050EA, Agilent, CA, USA). All MR experiments were performed on 3T and 7T whole body human scanners (Siemens Healthcare, Erlangen, Germany). All imaging experiments were collected on three healthy volunteers recruited under a university approved Institutional Review Board (IRB). All the pulse sequences parameters are listed in Table 4.2. Noise correlation measurements were acquired by setting RF amplitude to 0 V with TR = 2000, TE = 0.15, Number of acquisition = 1, Acquisition duration= 204 ms, Vector size =2048, and bandwidth = 10 KHz. Accelerated images were acquired for AF = 0, 1, 2 and 4 for the T1W VIBE sequence.

Table 4.2 7T musculoskeletal imaging protocols used to acquire MR images (see Figures. 4.4, 4.5, 4.7 to 4.9)

ISO Sequences	Orientation	FOV	TR/TE (ms)	Slices
T2 DESS	Coronal	105x 160mm (294x 448)	18/5.2	238
T1 VIBE	Coronal	95 x 160mm (304x512)	12/4.5	288
T2 SWI	Axial	105 x 160mm (336x512)	23/15	128
DTI (Dir:64, b=0,1300)	Axial	700 x 620mm (490x434)	7000/83	65
TOF	A/S/C	85 x 208mm (236x640)	12/4.5	-
B_1^+ map Seq.	Axial	140 x 140mm (64 x 64)	2000/2.5	88

SNR was measured and is listed in the Results Section. At 7T, the above described RF coil system was used; at 3T, a dedicated eight-channel knee coil (Siemens, Erlangen, Germany) was used. Within both systems, the coils were positioned in the center of the magnet bore during the scan. The subjects were placed in a prone position with a pillow for additional comfort.

4.3 RESULTS

4.3.1 Coil Evaluation

4.3.1.1 Transmit Coil

i) Bench Measurements: The S-parameters were measured and are shown in Figure. 4.3. The measured reflection coefficients (S11, S22) were greater than or equal to -23 dB under the loaded (forearm) condition and -20dB for the muscle phantom with a conductivity of 0.8 S/m and relative permittivity of 79 (measured using the DAK SPEAEG system Zurich). Figure 4.3A shows excellent agreement between the FDTD calculated scattering parameters (S11, S22 and S12) and those measured utilizing the network analyzer. The transmission coefficient (Isolation, S12) was ≤ -18 dB (<3%), as shown in Figure 4.3A. The Q factor unloaded to loaded ratio of the TEM volume resonator was 240/90.

ii) Bench Measurements: The tuning/matching of the Tx coil was minimally affected by the receive loops after turning on the active decoupling (see Figure. 4.3B for Ports 1 and 2).

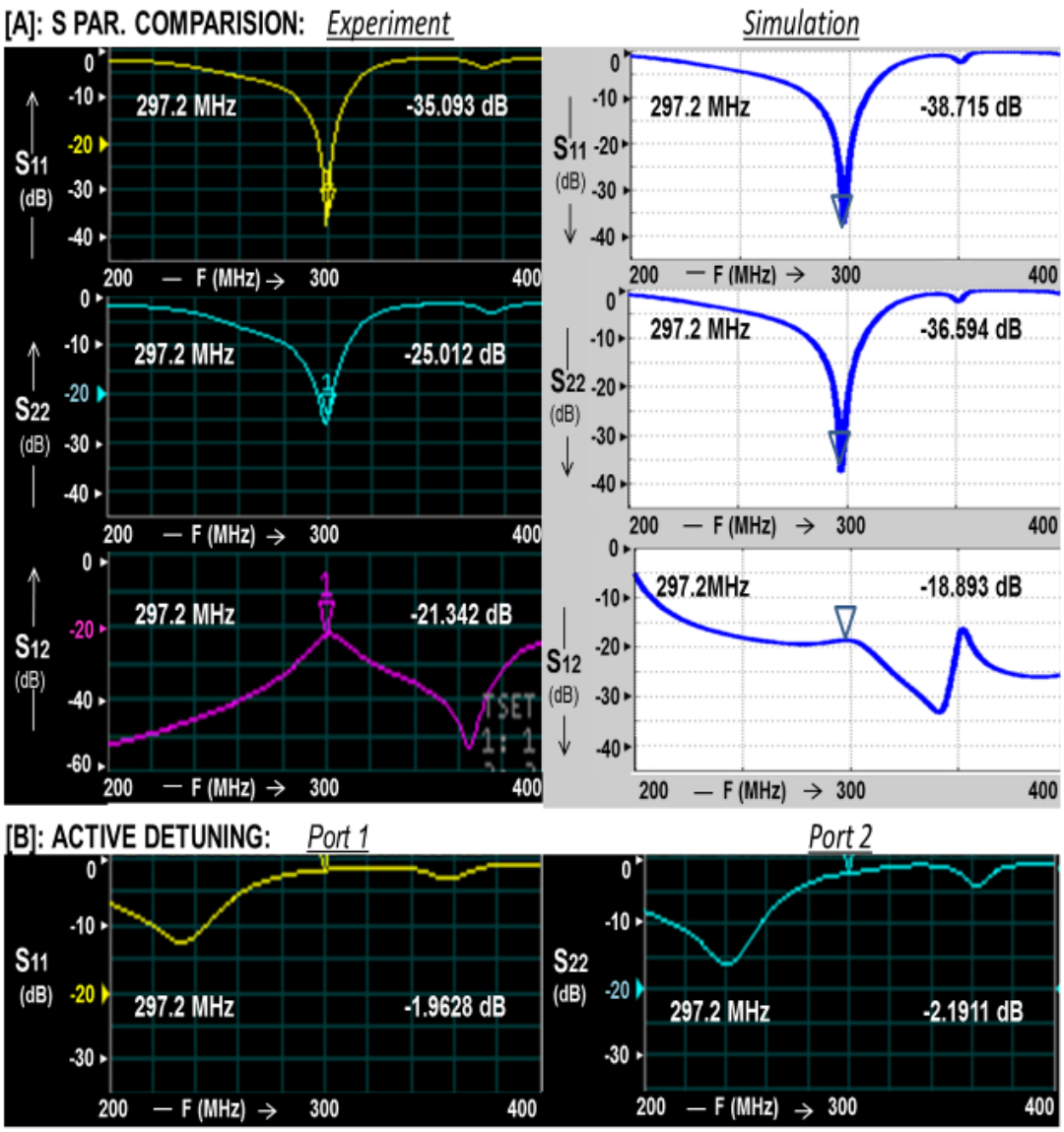

Figure 4.3 S parameter comparisons.

A: Correlation between the FDTD calculated scattering parameters (S11, S22 and S12) and those measured utilizing the network analyzer for the TEM coil; and B: TEM active Detuning (with DC ON) for S11 and S22.

iii) Imaging Measurements: Measured B_1^+ maps demonstrate very good agreement with the simulated B_1^+ field distribution, as shown in Figure 4.4. The B_1^+ field coverage and homogeneity are excellent, except near the drive ports (towards wrist). Homogenous T2W DESS images shown in axial, coronal and sagittal planes covering the whole volume of the forearm are demonstrated in Figure. 4.5.

iv) Simulations: The FDA [146] and International European Commission (IEC) [147] have formulated safety limits based on SAR. In extremities, the IEC 60601-2-33 states that MRI systems must limit locally deposited RF power to under 20 W/kg/10g under combined mode of tissue without cranial exposure [147]. For 3ms square RF pulse, a B_1^+ field intensity of 1.97μT is required to generate 90° excitation. Based on a continuous 1.97μT (averaged over the volume of the arm inside the TEM coil), the average SAR is 2.02 W/Kg and peak SAR is 8.98 W/Kg/10g. As expected with smaller (when compared to the human head at 7T) electrical size loads, the simulated SAR (Figure. 4.4) shows higher SAR intensities near the periphery [41].

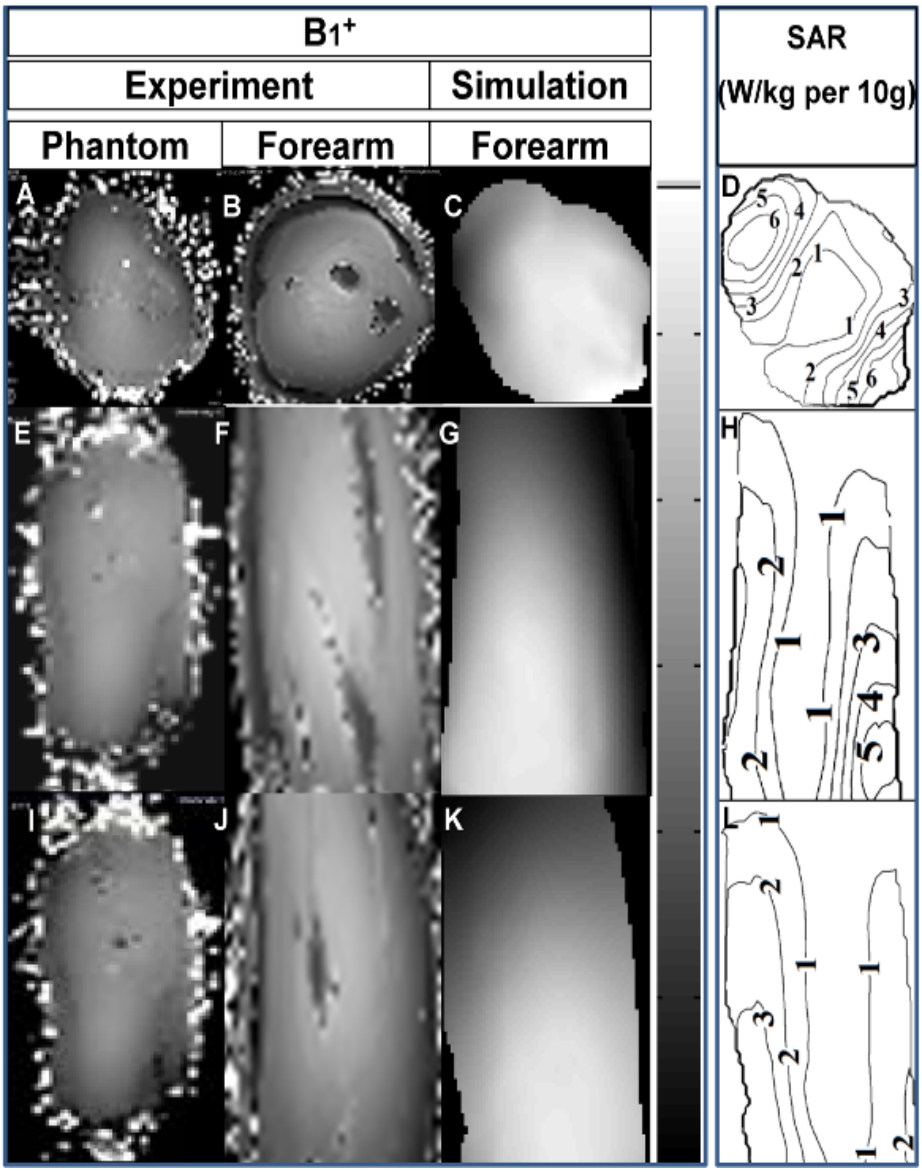

Figure 4.4 B_1^+ field and SAR map.

7T experimental B_1^+ field maps for a muscle phantom (A: axial, E: sagittal and I: coronal) and human subject (B: axial, F: sagittal and J: coronal). Simulated B_1^+ maps (C: axial, G: sagittal and K: coronal) and SAR (W/kg per 10g; D: axial, H: sagittal and L: coronal) obtained using anatomically detailed human arm.

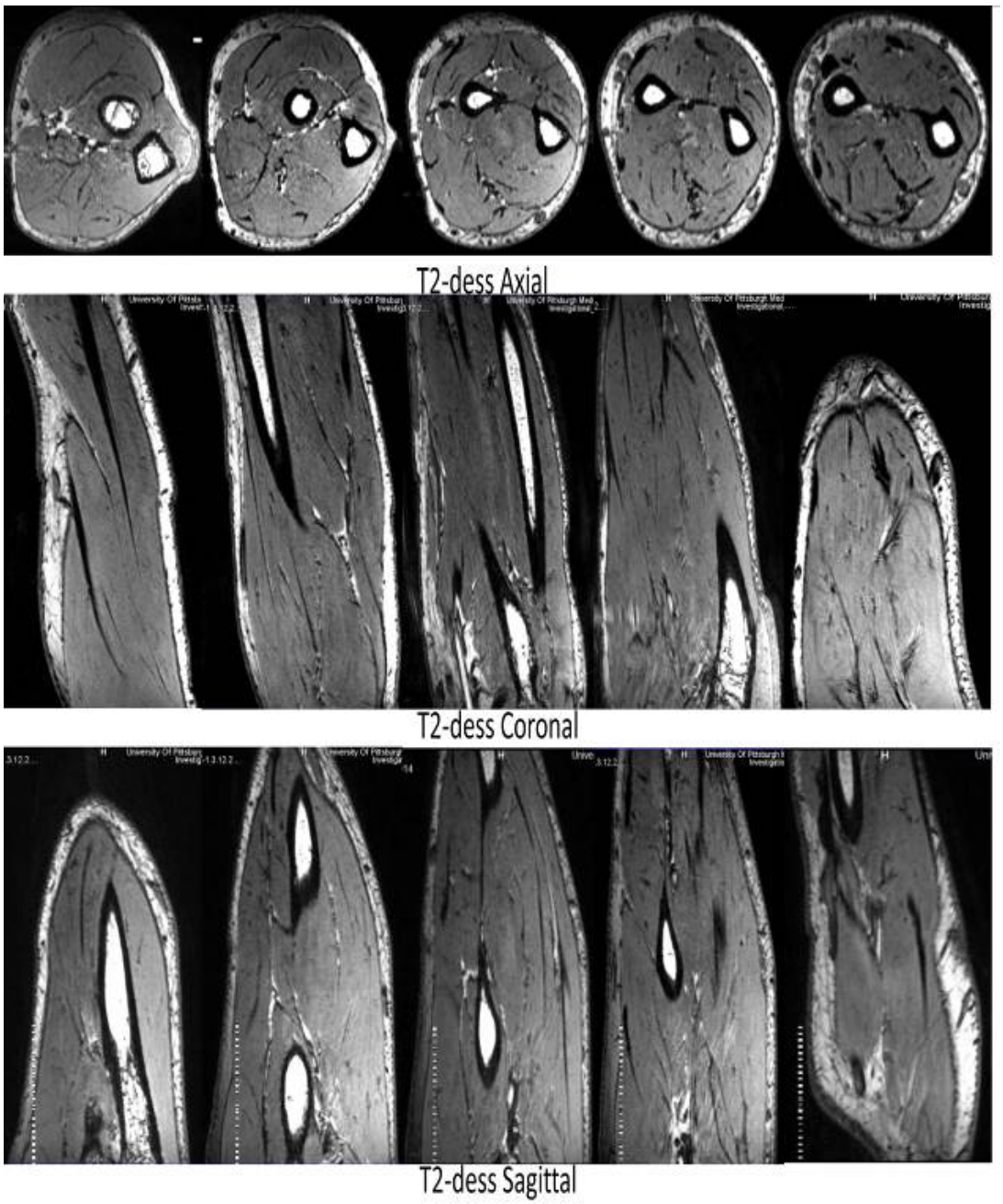

Figure 4.5 7T T2 DESS over the complete volume of the forearm in axial (elbow to wrist), coronal and sagittal planes.

4.3.1.2 Receive Array

i) Bench measurements: All eight receive channels had a minimum reflection coefficient of -15dB (as shown in Figures. 4.6A and 4.6B for Rx Channels 2 and 4) and transmission coefficient (between adjacent neighbors and next to adjacent neighbors) ≤ -13 dB (< 5 %, as shown in Figure. 4.6C). These isolation measurements were carried out inside the resonator while decoupling the Tx coil using active DC bias.

ii) Bench measurements: Active decoupling was measured to be ≤ -18 dB using a decoupled flux probe and switching the power supply mode (E530712, Hewlett-Packard (HP) universal power source, USA). Also, an active detuning circuit was turned ON using DC bias and measured on a network analyzer, as shown in Figure. 4.6D (Rx Channel 4 with DC ON).

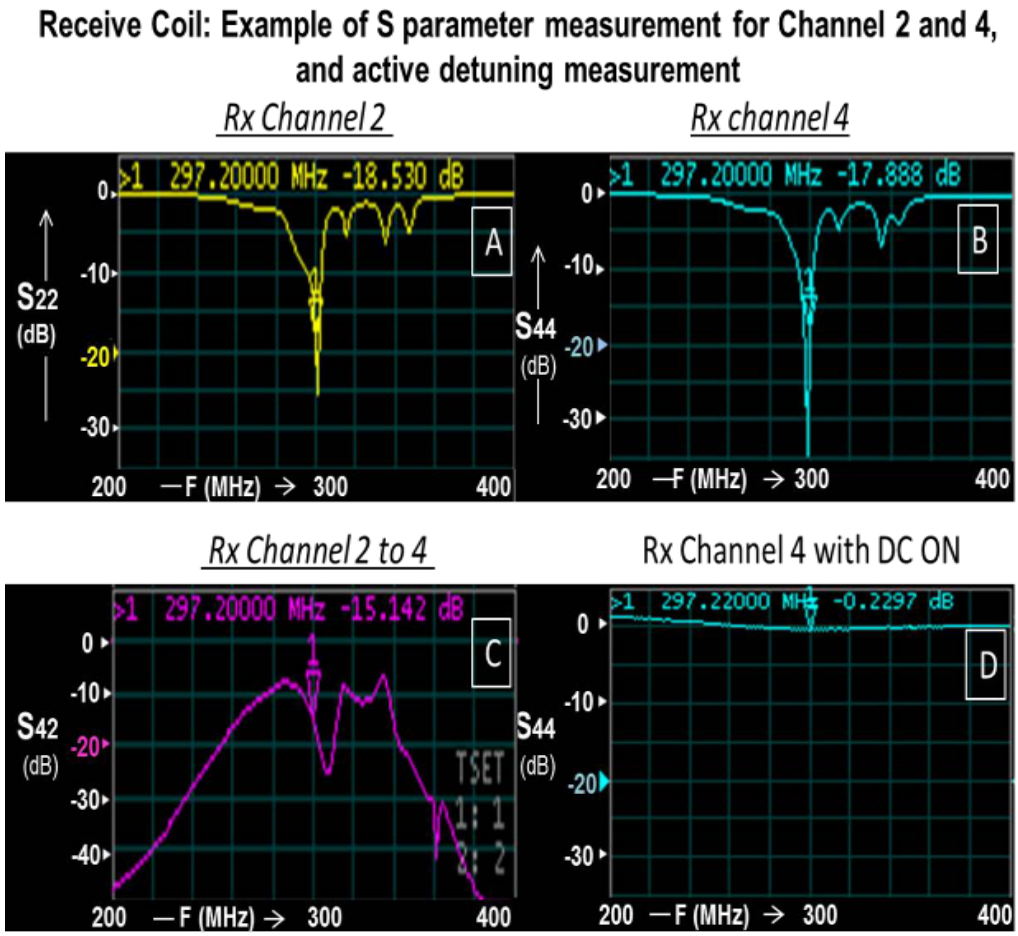

Figure 4.6. Receive coil measurements.

A: S22 measurement (Channel 2 of 8); B: S44 measurement (Channel 4 of 8); C: S42 (isolation) measurement (Channels 2 and 4); and D: Active Detuning (with DC ON) for Channel 4.

iii) Imaging Measurements: Figure. 4.7A shows a typical noise correlation matrix for the receive-only array acquired using the 7T system. The average off-diagonal correlation is -20.5dB and only higher coupling (-9.7dB) was found between opposite elements 3 and 6.

iv) Imaging Measurements: Figure. 4.7B shows measured SNR for five slices throughout the forearm for each acceleration factor (AF = 0, 1, 2, and 4). The average SNR (mean of five slices) falls down to one third for AF = 4 (SNR = 23) compared to AF = 0 (SNR = 66) where the SNRs for AF = 1 and AF = 2 were 56 and 41, respectively. For AF = 0, 1, and 2, the quality goes from excellent to good (based on clear delineation of various anatomical structures) but picture becomes substantially blurry for AF = 4, as shown in Figure. 4.7C.

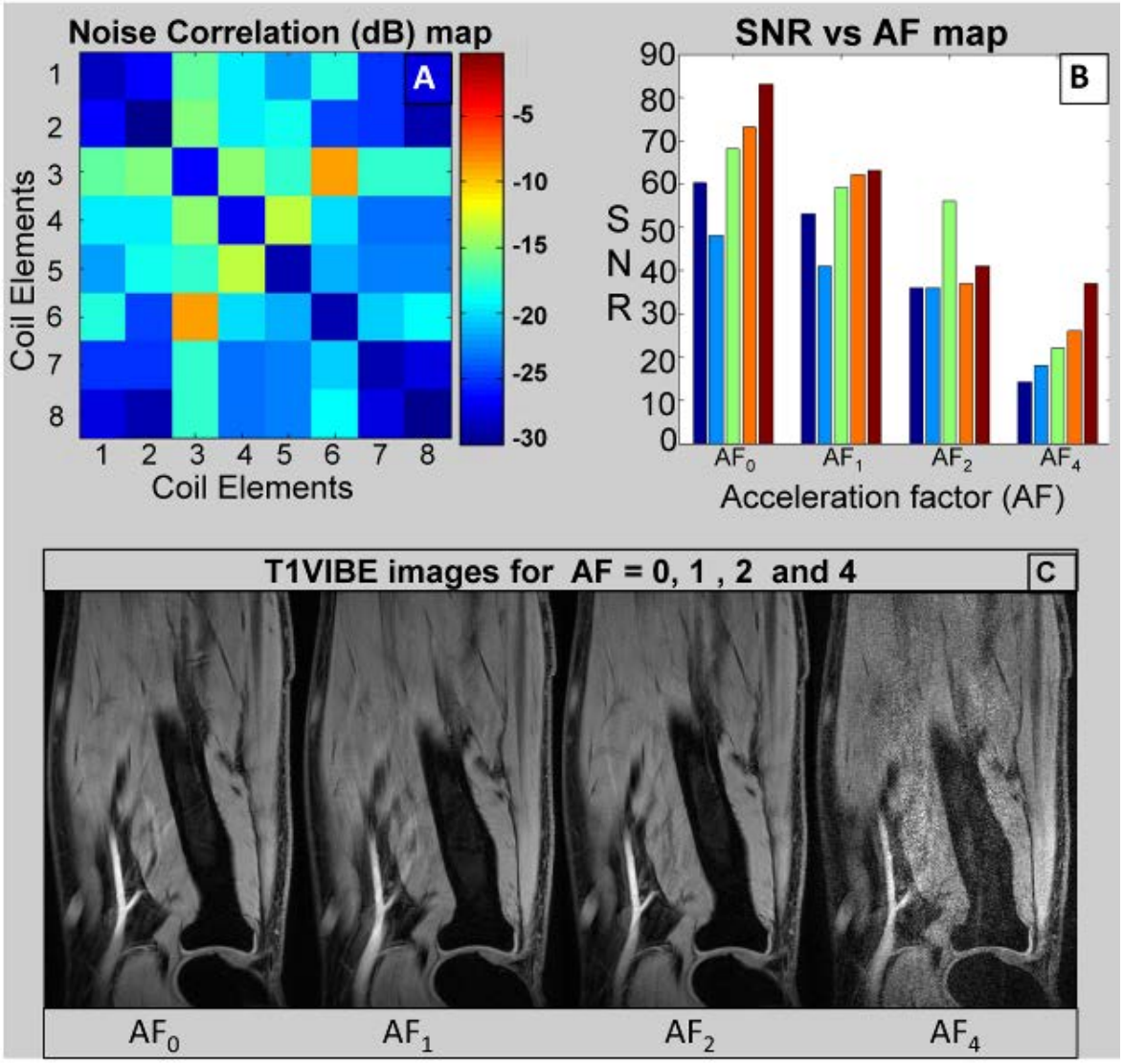

Figure 4.7 Noise Correlation, SNR vs AF, T1 VIBE images for AF=0, 1, 2, and 4. A: Noise correlation matrix for receive-only array; B: SNR vs acceleration factor (AF) map, each set (five bars) represents five slices throughout the forearm volume; and C: Respective images (center slice) for AF as shown in B.

4.3.2 In-vivo Imaging

Figure. 4.8 presents a comparison of 3T vs 7T for three sequences (T1 VIBE, T2 DESS and T2* SWI). The 3T and 7T protocols were optimized for the same scanning time, comparing i) higher resolution 3T vs 7T Protocol (the protocol was optimized for best 7T quality/resolution and the same scans were acquired for 3T) ii) lower resolution 3T vs 7T protocol (the protocol was optimized for best 3T quality/resolution and the same scans were acquired at 7T).

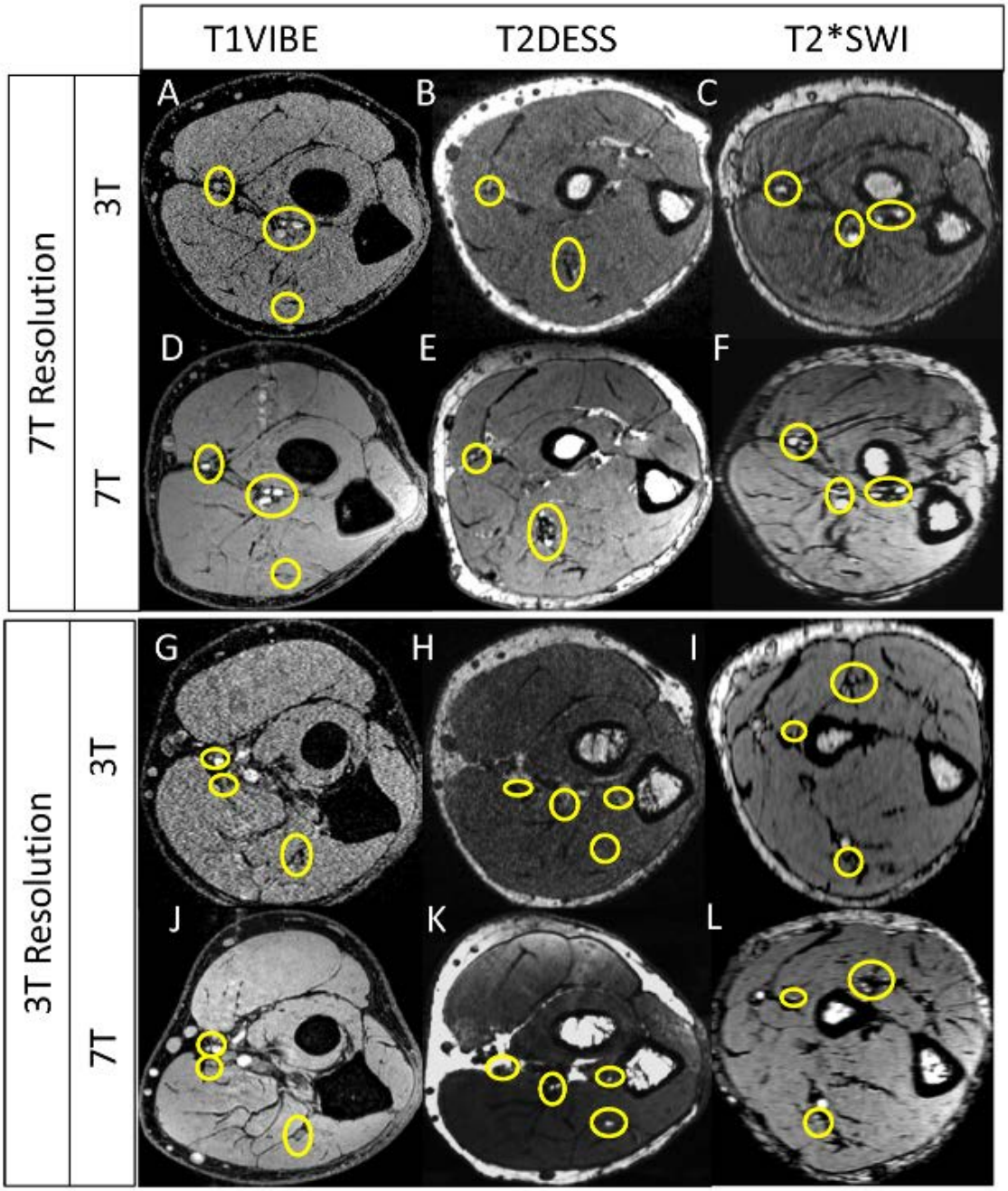

Figure 4.8 3T vs. 7T imaging.

Protocols are described in Table 4.2. The circles show nerve and small vessel finding in 3T vs 7T.

4.3.2.1 T1 VIBE: Figures. 4.9A1-5 demonstrate high resolution on T1 VIBE images, identifying various anatomical structures as follows:

A1: forearm (vessel wall delineation (arrow), brachial artery bifurcation and its branches);

A2: micro-vasculature; radial and median nerves and their branches;

A3: forearm superficial radial nerve;

A4: supracondylar joint anatomy with osseocartilagenous detail; and

A5: median and radial nerves (arrows) and arterial sections (radial artery) with vessel wall delineation.

4.3.2.2 T2 DESS: High resolution T2 3D gradient echo imaging is carried out by DESS sequence. Figures. 4.9B1 and 4.9B2 show excellent high intensity signal separating nerves and exquisite contrast for viewing cartilage and synovial fluid, with excellent cartilage delineation and joint structures. B1 specifically shows the axial view of trochlear cartilage and trabecular bone structure and ulnar nerve (arrow). B2 shows synovial and cartilagenous delineation of the radiohumeral joint with trabecular detail (arrow).

4.3.2.3 T2* SWI (typically not used in upper extremity imaging): Figure. 4.9C shows improved contrast that is complementary to the conventional spin-density, T1, and T2 imaging methods [9]. Figure. 4.9C1 shows a T1 VIBE image displaying an axial section with vascular branching detail. Figure. 4.9C2 shows the corresponding SWI image with marked enhancement of the vascular patterns of the brachial and radial arteries and muscular perforators.

4.3.2.4 Diffusion Tensor Imaging (DTI): Figures. 4.9D1 and 4.9D2 represent T1 VIBE (D1) and FA color coded map (D2) slices in the forearm identifying the radial (RN) and median nerve (MN) locations (yellow circles). Figure. 4.9D3 presents a 3D view of both corresponding nerves (stretched yellow arrows). Also, Figure. 4.9D4 shows the fiber tractrography for the median and radial nerve after post-processing using DSI studio [148].

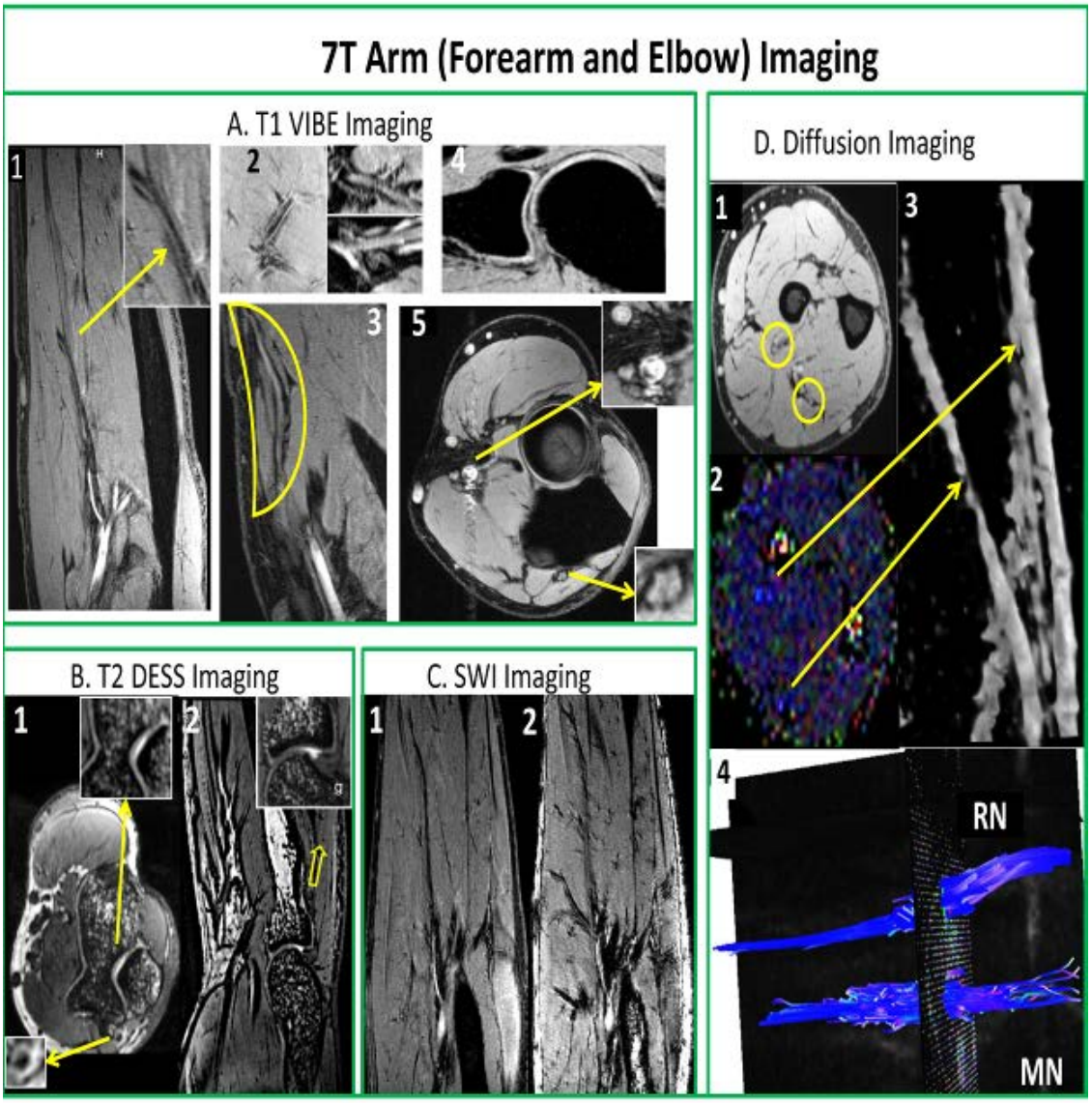

Figure 4.9 7T Arm (Forearm and Elbow) imaging.

Table 4.3 7T and 3T protocols (See Figure. 4.8)

MRI System: **Imaging:** **Parameters**	**7T** **TR/TE** **Fov/Acquisition Matrix** **Scan time/Slices**	**3T** **TR/TE** **Fov/Acquisition Matrix** **Scan time/Slices**
T1VIBE: 7T-Resolution	12/4.49 ms 95 x 160 mm^2/277 x 512 5:34 min/288	12/5.21 ms 95 x 160 mm^2/277 x 512 5:34 min/288
T1VIBE: 3T-Resolution	12/4.47 ms 93 x 100 mm^2/273 x 320 4:36 min/288	12/5.14 ms 95 x 159 mm^2/191 x 352 4:01 min/288
T2 DESS: 7T-Resolution	18/5.22 ms 105 x 160 mm^2/270 x 448 4:43 min/288	18/5.22 ms 105 x 160 mm^2/270 x 448 4:43 min/288
T2 DESS: 3T-Resolution	18/5.22 ms 91 x 140 mm^2/193 x 320 3:36 min/176	18/5.22 ms 104 x 159 mm^2/232 x 384 4:08 min/240
T2*SWI: 7T-Resolution	23/15 ms 105 x 160 mm^2/302 x 512 6:08 min/128	23/14.2 ms 118 x 180 mm^2/302 x 512 6:08 min/128
T2* SWI: 3T-Resolution	23/15 ms 118 x 180 mm^2/227 x 384 4:42 min/128	23/14.2 ms 118 x 180 mm^2/227 x 384 4:42 min/128

4.3.2.5 MRI (Non-contrast) Angiography: Figure. 4.10 shows not only first and second order arteries (superficial palmar and deep palmar arch) but also the smaller proper palmar digital arteries in the fingers and pulps. Figure. 4.10A1 is a cross-sectional transmetacarpal view highlighting the intrinsic muscles, the flexor and extensor tendon (T) apparatus with synovial sheaths (S) as well as ligamentous structures (L), and the intermetacarpal vasculature (V). Figure. 4.10A2 is a minimum intensity projection and Figure. 4.10A3 a 3D texture reconstruction of the hand. Figure. 4.10B1 presents an excellent depiction of all of the proper palmer digital arteries, digital tendons and synovial sheaths on a transverse view with the fingers towards the palm. Figure. 4.10B2 shows a transverse slice close to the finger tips showing capillaries (red circles) branching out. Figure. 4.10B3 demonstrates capillaries in the finger pulps utilizing volume rendering and minimum intensity projection.

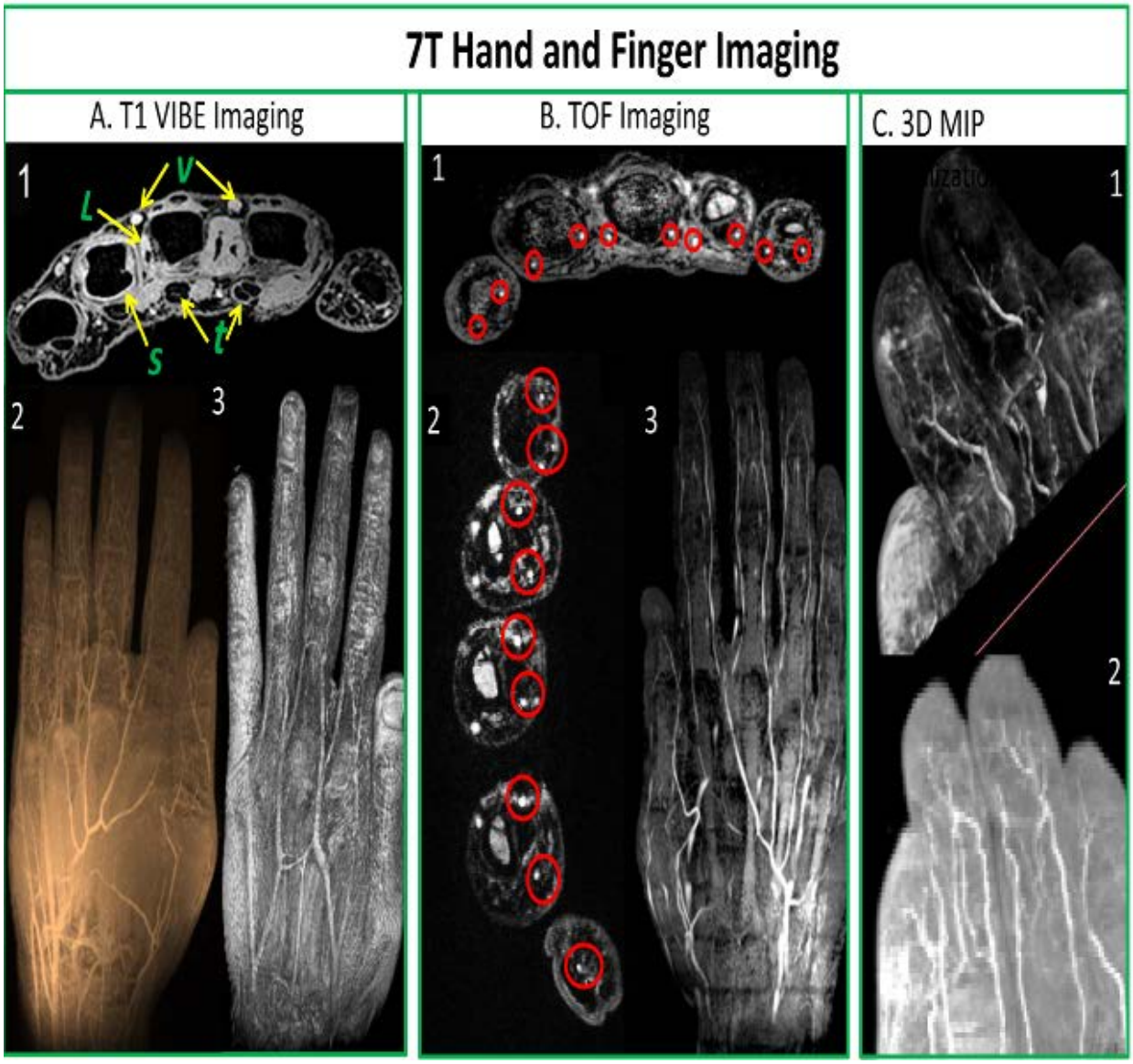

Figure 4.10: 7T Hand and Finger imaging.

4.4 DISCUSSION AND CONCLUSION

4.4.1 RF Coil

This is the first successful demonstration of a homogeneous volume resonator in conjunction with an eight-channel receive-only array for a targeted field of view UHF upper extremity imaging. This RF coil system was optimized for the human forearm but can be utilized to image the hand, wrist, arm or even elbow as there is no significant change in tuning properties required. With a small filling factor, the use of a combined transmit and receive coil is ideal to detect the incoming signal with nearly homogeneous excitation [149-152]. Furthermore, the Tx coil's B_1^+ field homogeneity can be further improved with more elements. It is also noted that there are other designs like a smaller loop [153] or a birdcage coil [154] that could be used in a transmit–receive design for specific applications like for the wrist or joint.

Since the receive array does not significantly affect the distribution/intensity of the B_1^+ field [155], the receive coil could possibly be replaced with higher density designs that have acceptable decoupling/isolations (12-16 channels given satisfactory isolation between receive elements, as shown in 32-ch head arrays [156]). This could further improve the SNR of RF coil system. In addition to overlapping geometry and inductive decoupling, preamp decoupling is also extremely important to achieve the desired operation as ionic currents in the tissues can induce electromagnetic force in the Rx array, which can cause correlated noise in the coil and reduction in SNR values [141, 157].

The Tx coil and Rx-only insert sizes were chosen to accommodate for anthropometric parameters consistent with bigger forearms. These sizes help the coil to be positioned comfortably anywhere from the arm (shoulder) to the hand (including digits). The coil placement allows the patient to lay comfortably on a padded MRI table in prone (superman or statue of liberty) position with arm or forearm in extension for the duration of the study. In order to make safe use of the coil, 1) the Preamplifiers were kept close to the matching circuit and balun, and 2) extra consideration was given to the cable arrangement by keeping the cables away from the patient.

4.4.2 3T vs. 7T

Visualization of small forearm vessels and nerves in both the superficial and deep soft tissues at high and low resolution 7T imaging is clearly superior to that of 3T imaging (as marked by yellow circles in Figure. 4.8). Delineation of muscle fibers/fascial plane interfaces as well as cortical bone/soft tissue interfaces is significantly enhanced at 7T, illustrating the benefit of higher CNR. Figure. 4.8 also shows superior delineation of the radial and median nerves, small vessel detail without the use of contrast agents, higher delineation of muscle planes, and details of osseous trabecular when compared those at to 3T. Specifically, the superior eminence of small vessels (and finer details of soft tissues) is the result of overall less noise at 7T compared to the 3T images. Noting that two different coil designs were utilized at 3T and 7T but both with 8 receive channels, the overall clarity of the 7T images as compared to 3T demonstrates the advantage of having a high SNR ratio associated with higher field strength.

4.4.3 Characterization of 7T Images

According to Musculoskeletal radiologists, AFs = 0, 1 and 2 (Figure. 7C) provide excellent quality to depict various anatomical structures (nerves, macro-and-micro vasculature, cartilage, synovial fluidic areas between cartilage, tendons, ligaments, osseous bone anatomy). On the other hand, AF = 4 results in poor image quality (Figure. 7C).

MR Diffusion imaging accesses water diffusion parameters like fiber anisotropy (FA) and the apparent diffusion coefficient (ADC) in nerves. This can be a non-invasive and non-disruptive strategy for sequential assessment of pre- and post-surgeries, including post-surgical nerve regeneration repair or transplantation related outcomes. As a result, reconstructive surgeries and/or evaluation of transplantations [133, 158] may use i) volume (and texture)-based rendering and ii) 3D depiction of the course of the peripheral nerves (as shown Figure. 4.9D). As shown in Figure. 4.9, 7T provides superior delineation of the radial and median nerves, without the use of contrast agents.

Contrast-enhanced MR angiography using commercial MR scanners (≤ 3T) have been extensively used in imaging of intracranial vessel diseases [159, 160] and 7T imaging has also been explored [161]. Limited, if any, imaging with 7T MRI has been reported of the extremities, except that specifically focusing on wrist [162] or hand [163] and limited to the palmer vasculature. The current work goes beyond the wrist and palmer region to high resolution non-contrast enhanced imaging of the digital arteries in the fingers and their pulps, as shown in Figure. 4.10 (TOF). The fact that this may be accomplished without the use of intravenous contrast is

invaluable in patients with vasculitis associated with either autoimmune disorders or diabetes, as these diseases often have concomitant renal vasculitis and renal insufficiency.

Moreover, detection of small vessel anatomy using high resolution 7T imaging has a potential in preoperative planning [164] of neovascularity associated with both soft tissue as well as osseous tumors. 7T TOF imaging also allows for excellent depiction of the microvascularity of the hand, forearm, and hand (wrist), which may be invaluable in upper extremity surgery and/or monitoring the microvascularity integrity as it relates to certain vascular disease processes [165, 166]. In addition, SWI (Figures. 4.9C2) could be especially useful in various micro-vascular conditions like vascular trauma, abnormalities, visualizing blood products and the vascularization of tumors, and high-resolution MR venography [9, 167, 168]

In conclusion, an in-house built TEM volume resonator in conjunction with an eight channel receive only array was designed, built and successfully evaluated at 7T to confirm the potential for next generation UHF imaging in upper extremity applications. A wide variety of outstanding images with high spatial resolution, SNR, and CNR were achieved and fovorably compared to those acquired at 3T.

5.0 EVALUATING THE CLINICAL FEASIBILITY OF UPPER EXTREMITY IMAGING AT 7T MRI.

5.1 ULTRA-HIGH FIELD UPPER EXTREMITY PERIPHERAL NERVE AND NON-CONTRAST ENHANCED NEURO-VASCULAR IMAGING.

5.1.1 INTRODUCTION

As we explored coil design in an earlier chapter, this chapter will provide background as to MRI use in clinical imaging and discuss in-vivo imaging in detail. Ultra-high field (UHF) (≥ 7T) human magnetic resonance imaging (MRI) typically provides superior SNR and CNR ratios when compared to lower field (≤ 3T) MRI [21, 137]. Although commercially (1.5T/3T) MRI is routinely used in upper extremity imaging (shoulder, forearm, hand, and wrist), the resolution achieved can be limited. UHF MRI could significantly improve the resolution capabilities of conventional MRI [18, 169]. However, 7T human MRI is fraught with technical challenges, mainly related to radiofrequency (RF) field inhomogeneity and safety concerns for neurologic and whole-body imaging applications [21, 37, 170-172]. The upper extremity offers the advantage of a compact isolated anatomy with relatively smaller electric size (when compared to the head/abdomen). Therefore, it can be relatively easier to generate uniform and safer RF field

distributions for 7T in upper extremity imaging. As a result, significantly higher anatomical resolution and further improvements in the contrast of tissue interfaces can potentially be achieved at 7T for upper extremity applications without increased scanning times and/or considerable compromise in overall image quality.

Higher SNR/CNR can be useful in providing intricate detail in neural [173], vascular [174], cartilage [175], tendon [176] and joint [177] imaging. As described in [158, 178, 179], 2D and 3D multi planar high resolution T1 weighted (T1) volumetric interpolated breath-hold exam (VIBE) imaging produces optimal anatomic detail and reveals high resolution structures. Nerves demonstrate a signal similar to adjacent soft tissue [178, 180]. High resolution T2 weighted (T2) double-echo steady state (DESS) can achieve excellent SNR/CNR for discriminating nerves from muscle, fascia, cartilage and synovial tissue in the forearm and joint structures [181]. According to [182], susceptibility weighted imaging (SWI) is particularly useful for visualization of vasculature since it is highly sensitive to deoxyhemoglobin in venous blood, making it useful in imaging vascular trauma and abnormalities and in visualizing neovascularization of tumors. Diffusion-based sequences specifically monitor the random movement of water molecules in anisotropic tissue [183, 184].

One of the major obstacles in UHF MRI remains the limited availability of custom-designed coils [185] optimized for musculoskeletal applications. Some prior studies have demonstrated the utility and feasibility of customized coil designs for high-resolution wrist imaging at 7T [18, 153, 154, 186]. Our group has recently developed a custom-designed forearm/hand MRI RF coil system [187-189] for 7T UHF imaging. The combination of such a

coil system in conjunction with 7T UHF MRI and many of the aforementioned sequences could hold significant potential in upper extremity imaging applications. Some of these applications include 1) sequential monitoring of regeneration after peripheral nerve (PN) repair, which is critical for evaluation of re-innervation and in planning treatment strategies [133, 190] and 2) monitoring vascular pathology or outcomes after vascular interventions without the need for potentially nephrotoxic or anaphylotoxic contrast agents [165, 191].

In this study utilizing a custom-designed RF coil system, we present the results and findings from various MR sequences (T1 VIBE, T2 DESS, SWI, time-of-flight (TOF), diffusion tensor imaging (DTI), and diffusion spectrum imaging (DSI)) that were optimized for 7T upper extremity imaging while keeping scanning times similar to or lesser than those used at 3T. We show detailed SNR and CNR comparisons of 3T vs. 7T for T1 VIBE and T2 DESS sequences. Furthermore, we show nerve tractography (diffusion imaging), vessel segmentation (nCE magnetic resonance angiography), and imaging of cartilage, synovial fluid, bone marrow and joint anatomy in the forearm, hand, and elbow at 7T.

5.1.2 MATERIALS AND METHODS

5.1.2.1 MR Hardware and Study Participants

Briefly, a shielded design of an actively detuned transverse electromagnetic TEM resonator [187, 188] with two ports driven by a quadrature hybrid was used in this study. An in-house finite difference time domain (FDTD) package was utilized [37, 113] in order to calculate the B_1^+ field (transmit field responsible for excitation) and SAR [192] parameters. An eight-channel receive-only insert array was designed and utilized with the TEM coil [187]. The array consisted of eight inductively decoupled surface loops [106] (each loop 18x8 cm^2 in size) distributed evenly to fit inside the structure of the Tx coil and cover the region of interest. The 7T RF coil system (Tx and Rx) covers 18 cm (in length) of anatomy (hand, forearm or elbow).

This prospective MRI study of upper extremity (forearm, hand, and elbow) was approved by the University of Pittsburgh Investigational Review Board (IRB). It was performed on three volunteers with appropriate written informed consent approved by above-mentioned IRB protocol. Volunteers were screened to exclude those with musculoskeletal disease, upper extremity trauma, surgery, and/or comorbidities associated with musculoskeletal abnormalities (neuropathies, rheumatoid syndromes etc.)

5.1.2.2 MR Examination

Imaging was performed using a 7T whole-body MRI system (Magnetom, Siemens Healthcare, Erlangen, Germany) and 3T whole-body MRI system (Tim Trio, Siemens Healthcare, Erlangen, Germany) at the University of Pittsburgh. The above-mentioned RF coil system was utilized at 7T. [187-189]. A dedicated eight-channel extremity coil (Siemens, Erlangen, Germany) was used at 3T. The coils were positioned in the center of the magnet bore during all imaging sessions. Subjects were positioned prone within the coil with the hands (forearm, and elbow) placed over the head and immobilized with cushions, pads and sandbags to avoid discomfort.

5.1.2.3 MR Imaging

The five imaging sequences (T1 VIBE, T2 DESS, SWI, DTI, DSI, and TOF) were optimized by a highly experienced MR application scientist using a clinical MRI protocol for upper extremity pathologies. 3T and 7T protocols were optimized for the same scanning time comparing a i) Higher Resolution (HR) protocol (optimized for best 7T quality/resolution, with the same scans acquired at 3T) and ii) Lower Resolution (LR) protocol (optimized for best 3T quality/resolution, with the same scans acquired at 7T). This study compares T1 VIBE and T2 DESS qualitatively and quantitatively (SWI was only qualitatively compared). 3T vs. 7T diffusion and TOF comparisons were not performed for this study. All of the sequence parameters are documented in Tables 5.1 and 5.2. In the case of the 7T diffusion sequences, the specific b-values were optimized by balancing b-field directions (64) with higher b–values (DTI: 0 to 1300; DSI: 0 to 2000) while obtaining 1) smaller voxel resolution, and 2) acceptable time of acquisition (183) and

SAR. 7Ts with a parallel imaging factor of 2 and 3 were utilized to achieve the results shown (Tables 5.1 and 5.2).

Table 5.1 7T and 3T T1VIBE, T2 DESS and T2* SWI Forearm protocols for HR: higher and LR: lower resolution sequences. These sequences cover Figure. 5.1.1, 5.1.2, 5.1.3 and 5.1.4.

MR Sequences (Forearm)	**T1 VIBE (Figure. 5.1)**		**T2 DESS (Figure. 5.2)**		**T2* SWI (Figure. 5.4)**	
Field Strength	7T HR	3T HR	7T HR	3T HR	7T HR	3T HR
TR/TE (ms)	12/4.49	12/5.21	18/5.22	18/5.22	23/15	23/14.2
Slice	288	288	238	288	128	128
FOV (mm^2)	95x160	95x160	105 x 160	105 x 160	105 x 160	118 x180
Acquisition Matrix	277x512	277x512	270x448	270x448	302x512	302x512
Pixel Res(mm^3)	0.3	0.3	0.4	0.4	0.8	0.8
Voxel Size (mm^3)	0.31x0.31 x0.30	0.34x0.31 x0.30	0.36x0.36 x0.40	0.36x0.36x 0.40	0.31x0.31x 0.80	0.35x0.35x0.80
FA	10	10	25	25	20	20
Acceleration factor	2	2	2	2	2	2
Bandwidth(hz/px)	150	150	169	169	119	119
Acquisition time (min)	5:34	5:34	4:43	4:43	6:08	6:08

Table 5.1 (Continued)

Field Strength	**7T LR**	**3T LR**	**7T LR**	**3T LR**	**7T LR**	**3T LR**
TR/TE (ms)	12/4.47	12/5.14	18/5.22	18/5.22	23/15	23/14.2
Slice	288	288	176	240	128	128
Fov(mm^2)	93x100	95x160	91 x 140	105 x 160	118 x180	118 x 180
Acquisition Matrix	273x320	191x352	193 x 320	232 x 384	227 x 384	227 x 384
Pixel Res(mm^3)	0.4	0.3	0.5	0.4	0.8	0.8
Voxel Size (mm^3)	0.31x0.31 x0.41	0.49x0.45 x0.30	0.44x0.44 x0.50	0.42x0.42x 0.40	0.47x0.47x 0.80	0.47x0.47x0.80
FA	10	10	25	25	20	20
Acceleration factor	2	2	2	2	2	2
Bandwidth(hz/px)	150	150	195	194	119	119
Acquisition time (min)	4:36	4:01	3:36	4:08	4:42	4:42

Table 5.2 7T in-vivo imaging protocols for Elbow, Forearm, and Hand (Figures. 5.1.3, 5.1.5-5.1.8; T1VIBE, T2 DESS, T2* SWI, DTI, and TOF).

MR Sequences	**T1 VIBE (Elbow)**	**T2 DESS (Elbow)**	**DTI (Forearm, Dir:64, b=0,1300)**	**DSI (Forearm, b=0 to 2000)**	**TOF (Hand)**
Orientation	Coronal	Coronal	Axial	Axial	A/S/C
FOV (mm^2)	93 x 100	91 x 140	70 x 62	70 x 62	85 x 208
Acquisition matrix	273 x 320	193x320	490x434	490x434	236x640
TR (ms)	12	18	7000	8000	12
TE (ms)	4.49	5.22	83	80	4.5
Slices	240	176	65	65	254 (single slab)
Bandwidth	150	195	-	-	163
Acquisition time	5:34	3:36	27	45	-
FA	10	25	180	90	19
Acceleration factor	2	2	2	2	3
Voxel Size (mm^3)	0.34 x 0.31 x 0.41	0.44x0.44x0.5	1.43x1.43x3	1.72x1.72x1.7	0.33x0.3x0.4

5.1.2.4 MR Data Analysis

5.1.2.4.1 Quantitative Analysis

Quantitative 3T and 7T SNR and CNR were measured for T1 VIBE, and T2 DESS sequences over the complete volume of the forearm (presented in Figures. 5.1 and 5.2). Specifically, SNR was measured by calculating average signal intensity over a selected circular region (approximately encapsulates the forearm area excluding the skin) in each slice divided by the mean standard deviation (SD) of the background noise going from slice 1 (starting from the dorsal aspect) to slice 5 (close to the volar aspect). The CNR was defined as the difference in mean signal intensity between the bright tissue (vessel) and the adjacent bone signals (and /or background noise). Two musculoskeletal radiologists with over thirty-five years of combined clinical experience blindly evaluated the images and sequences. All measurements were performed by the same researcher and verified by the MR application scientist and both musculoskeletal radiologists.

5.1.2.4.2 Qualitative Analysis

Criteria for Evaluation of Image Quality: Contrast resolution, sharpness and clarity were the criteria considered in the evaluation of image quality using the following scale: 1-nondiagnostic, 2- poor, 3-fair, 4-good and 5-excellent (Table 5.3).

Evaluation of Imaging Artifacts: Presence of chemical shift, susceptibility artifacts and motion artifacts were considered in evaluation of the artifacts using the following scale: 1-absent, 2-present but not affecting anatomic detail and 3-present and severely affecting image interpretation.

Evaluation of image quality and artifacts were both carried out for 3T and 7T T1 VIBE, T2 DESS, and T2* SWI images (Figures. 5.1, 5.2, 5.3-5.6). The sequences were evaluated retrospectively and independently by two musculoskeletal radiologists who were blinded to the imaging parameters.

Table 5.3 3T/7T MRI Analysis (Image Quality Scale: 1-nondiagnostic, 2- poor, 3-fair, 4-good and 5-excellent; Artifacts scale: 1-absent, 2-present but not affecting anatomic detail and 3-present and severely affecting image interpretation).

Qualitative Analysis	**Image Quality factor**		**Artifact factor**	
Field Strength	**3T**	**7T**	**3T**	**7T**
T1 VIBE Lower Resolution (Figure. 5.1-Left)	3	3.5	1	1.5
T1 VIBE Higher Resolution (Figure. 5.1-Left)	3.5	4	2	2
T2 DESS Lower Resolution (Figure. 5.2-Left)	2.5	3	2.5	1.5
T2 DESS Higher Resolution (Figure. 5.2-Left)	2	3	1	1
T2* SWI Lower Resolution(Figure. 5.4)	1.5	2	2.5	2.5
T2* SWI Higher Resolution(Figure. 5.4)	1.5	2	3	2.5

5.1.2.5 MR Image Processing

For post-processing, diffusion-weighted images were used to perform a fiber tractography of the peripheral nerves in the forearm, and the principal fiber directions were used to conduct streamline fiber tracking. After the DTI data were transferred to a local computer, FSL (FMRIB,

Oxford, UK) and DSI Studio (CMU, Pittsburgh, PA) were used for distortion correction and fiber tracking, respectively. Geometric distortion in different acquisition directions may be induced by an eddy current. This eddy current is produced in the conductive materials/parts of an RF coil by the MRI gradient coils [183, 193, 194]. Combined with subject/patient motion, it can severely damage the diffusion estimation due to a pixel mismatch in the temporal image series [183]. Using the eddy-correct library available in FSL [194], eddy current and motion correction were implemented where the input reference image was a non-diffusion weighted image (b=0). Then T1 and T2 weighted images with DTI derived maps (Figures. 5.7C-F as later discussed in the Results Section) were utilized to locate the forearm nerves. Circular regions of interest (ROIs) were placed in the anatomic location of the nerves from the FA (Figure. 5.7D) and color-coded maps (Figure. 5.7F).

The fiber trajectories generated by an orientation distribution function–streamlined version of the Fiber Assignment by Continuous Tracking algorithm [148, 195, 196] were used to sample the FA and apparent diffusion coefficient (ADC) maps. Using a random seeding approach, we initiated tracking from each random position within the seed mask in the direction of the most prominent fiber. The following parameters were optimized in order to distinguish nerves from the surrounding various anatomical structures: an anisotropy threshold of 0.25, a step size of 0.35 to 0.5 mm, minimum fiber length of 0 to 20 mm, and a turning angle threshold of 60 degrees. The tracking was terminated when the relative fractional anisotropy for the incoming direction dropped below a preset threshold of ~0.2 (heavily dependent on SNR of the specific subject's scan data) or the turning angle exceeded 60 degrees. Each trajectory generated one profile, and all profiles were averaged to obtain the trend of the index along the fiber orientation. After anatomic confirmation

of the nerve tract, mean FA and ADC values were calculated as discussed later in the results section.

Non-contrast Enhanced (nCE) Angiographic Imaging and vessel segmentation: nCE MRA (TOF) techniques were utilized to image the digital proper palmar arteries at 7T. In order to extract the three dimensional structure of the vasculature in the forearm, the T1 VIBE DICOM images were exported in DICOM format to MIPAV [197]. A mask was created manually using the paint grow segmentation method in MIPAV, which utilizes the concept of voxel aggregation by grouping the seed points within the volume of interest (selected manually by minimum intensity projection (MIP)). The vasculature structures were manually traced in order to avoid errors in identifying the arteries and venous structure. After masking each segment (without skeletonizing or dilating to preserve structural vessel information), a surface and texture volume-rendering module was used to enable 3D visualization of the anatomy and segmented structures.

5.1.3 RESULTS

5.1.3.1 3T vs 7T

5.1.3.1.1 Quantitative Analysis: Figures. 5.1, 5.2, 5.3, and 5.4 demonstrate quantitative SNR and CNR measurements over the complete volume of the forearm in the T1 VIBE and T2 DESS images. For the HR protocol, the minimum SNR gain at 7T is ~ 1.8 (T1 VIBE) and ~ 2.2 (T2 DESS) times that of 3T; and the minimum CNR gain at 7T is ~ 2.2 (T1 VIBE) and ~ 2.2 (T2DESS)

times that of 3T. For the LR protocol, the minimum SNR gain at 7T is ~ 1.4 (T1 VIBE) and ~ 1.8 (T2 DESS) times that of 3T; and the minimum CNR gain at 7T is ~ 1.3 (T1 VIBE) and ~ 1.7 (T2 DESS) times that of 3T. As slices close to the dorsal part of the forearm do not have anatomic structures suitable for measuring CNR, some slices were excluded.

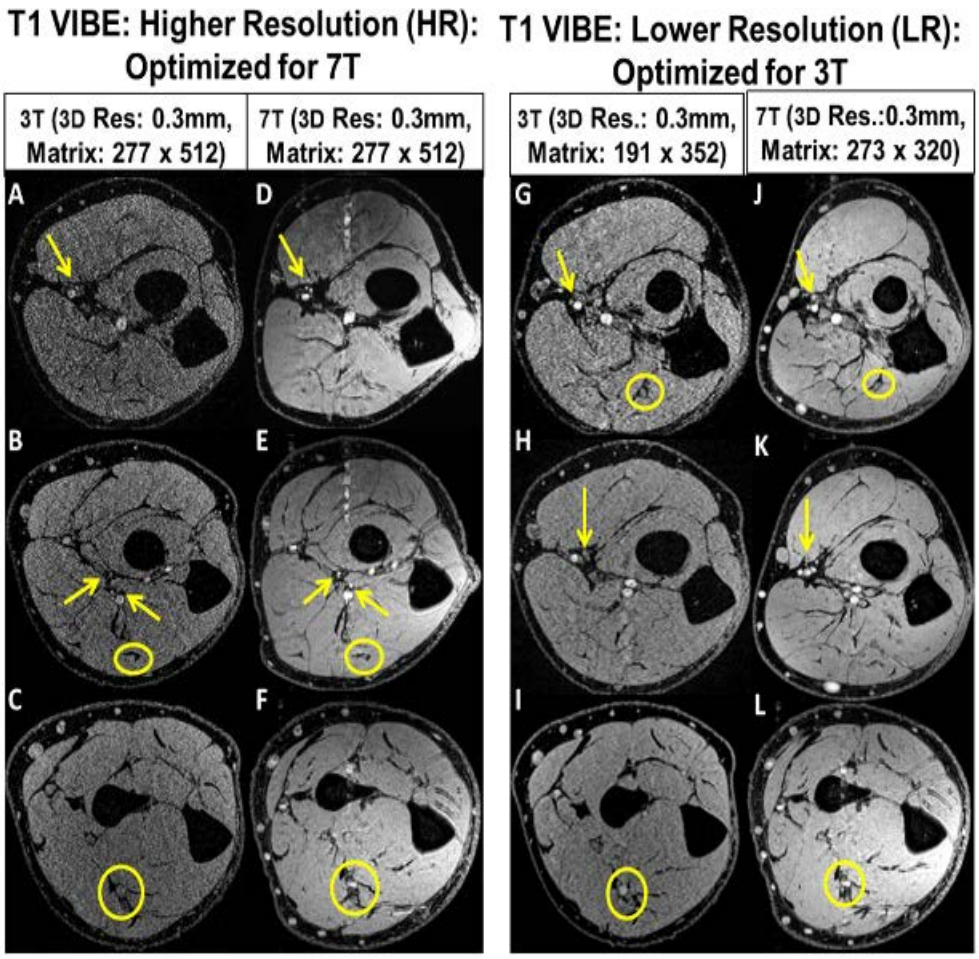

Figure 5.1 T1 VIBE (Higher and Lower Resolution) imaging.

3T vs. 7T T1 VIBE images on both higher (HR, which is optimized for 7T) and lower (LR, which is optimized for 3T) resolutions (as described in Table 5.1). In the 3T images (A, B, C, G, H and I), smaller order vessels as indicated by arrows are barely visible while in the 7T images they are well detected (D, E, F, J, K and L). Yellow arrows indicate micro-vessel branches and yellow ellipses delineate nerves from the surrounding muscle plane. Note that there are motion and pulsatile flow artifacts (bands of bright points) from the median artery in the anterior to posterior phase encoding direction.

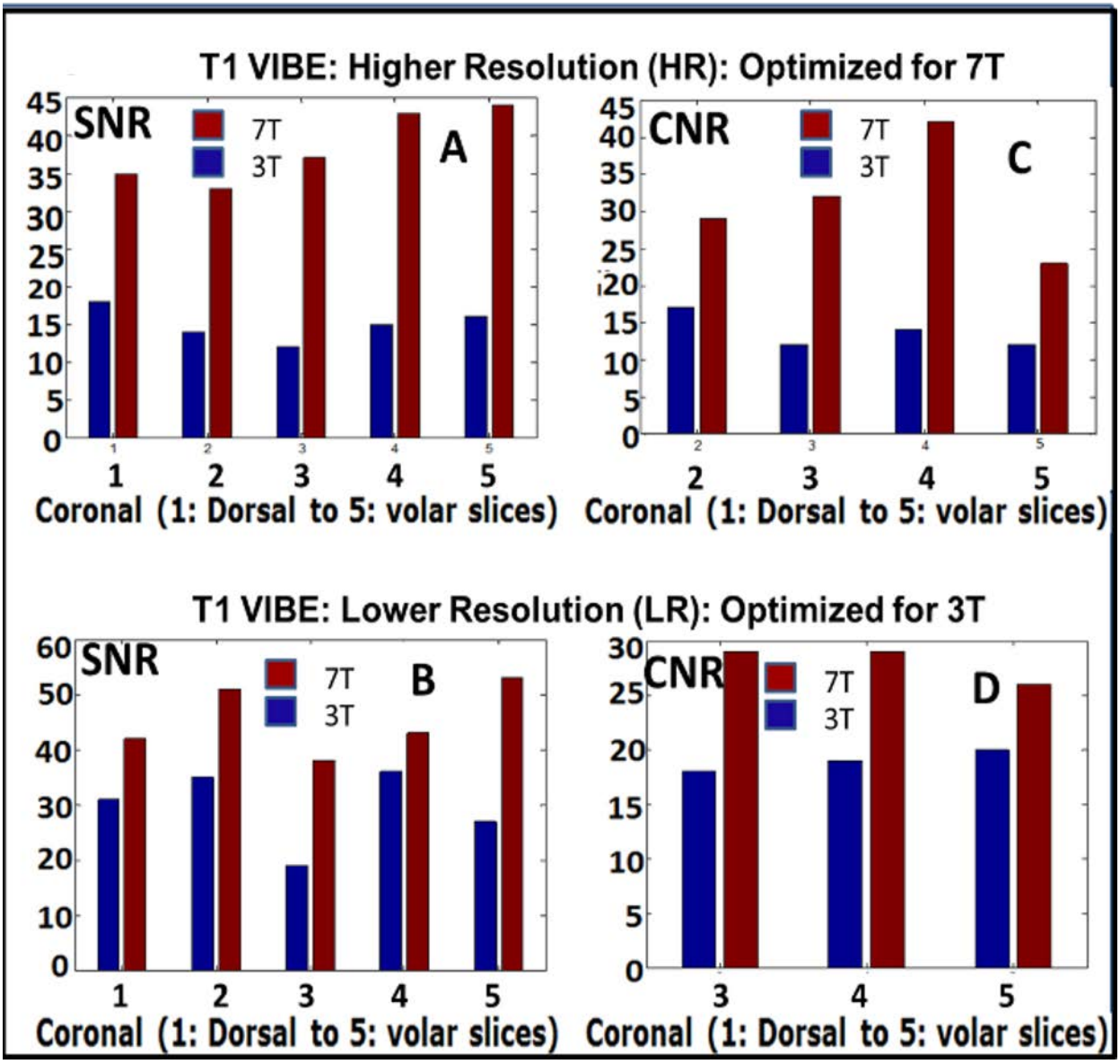

Figure 5.2: SNR and CNR charts for T1 VIBE images (Right).

(A and B) and (C and D) represent SNR and CNR, respectively. The 7T SNR and CNR were ~ 2/1.5 times that of 3T for the HR/LR scans, respectively.

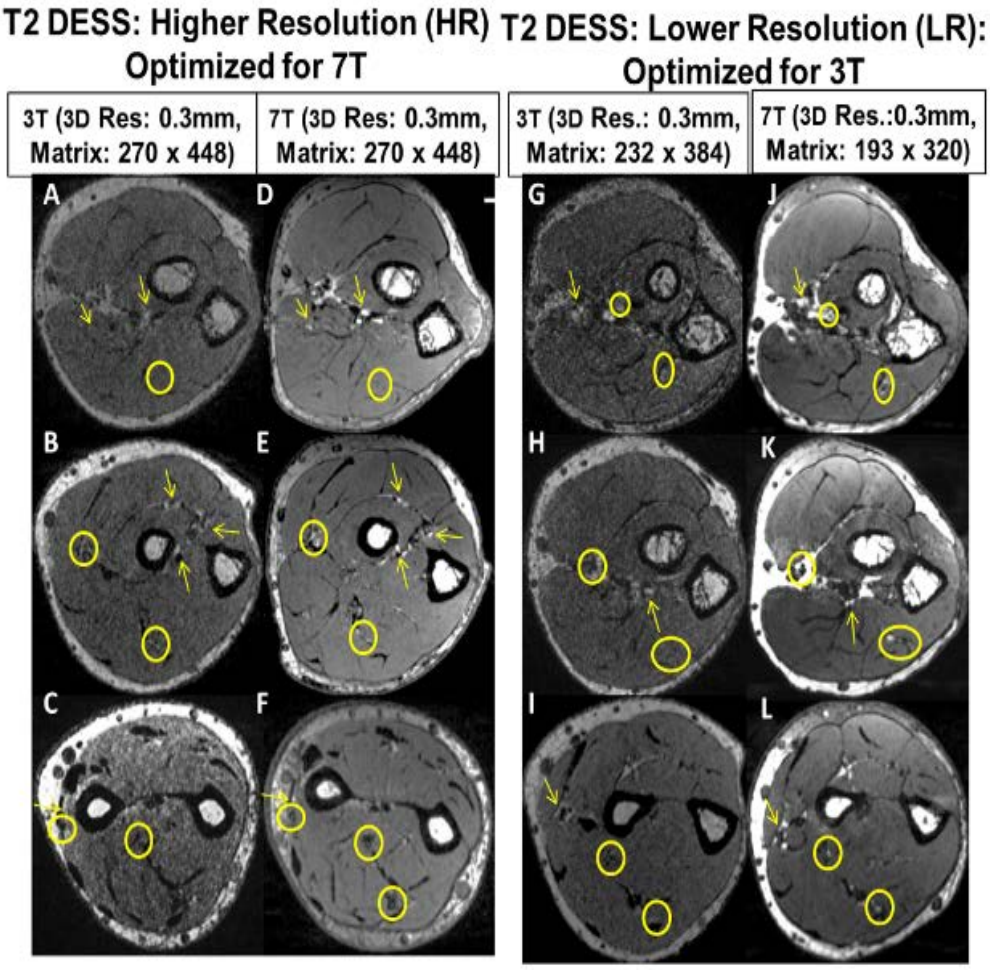

Figure 5.3 T2 DESS (Higher and Lower Resolution) imaging.

3T vs. 7T T2 DESS images on both higher (HR, which is optimized for 7T) and lower (LR, which is optimized for 3T) resolutions (as described in Table 5.1). Small order vessels [yellow arrows] and nerve [yellow circles] signals as indicated by circles are difficult to identify on the 3T (A, B, C, G, H and I) images but are well delineated on the 7T (D, E, F, J, K, L) images.

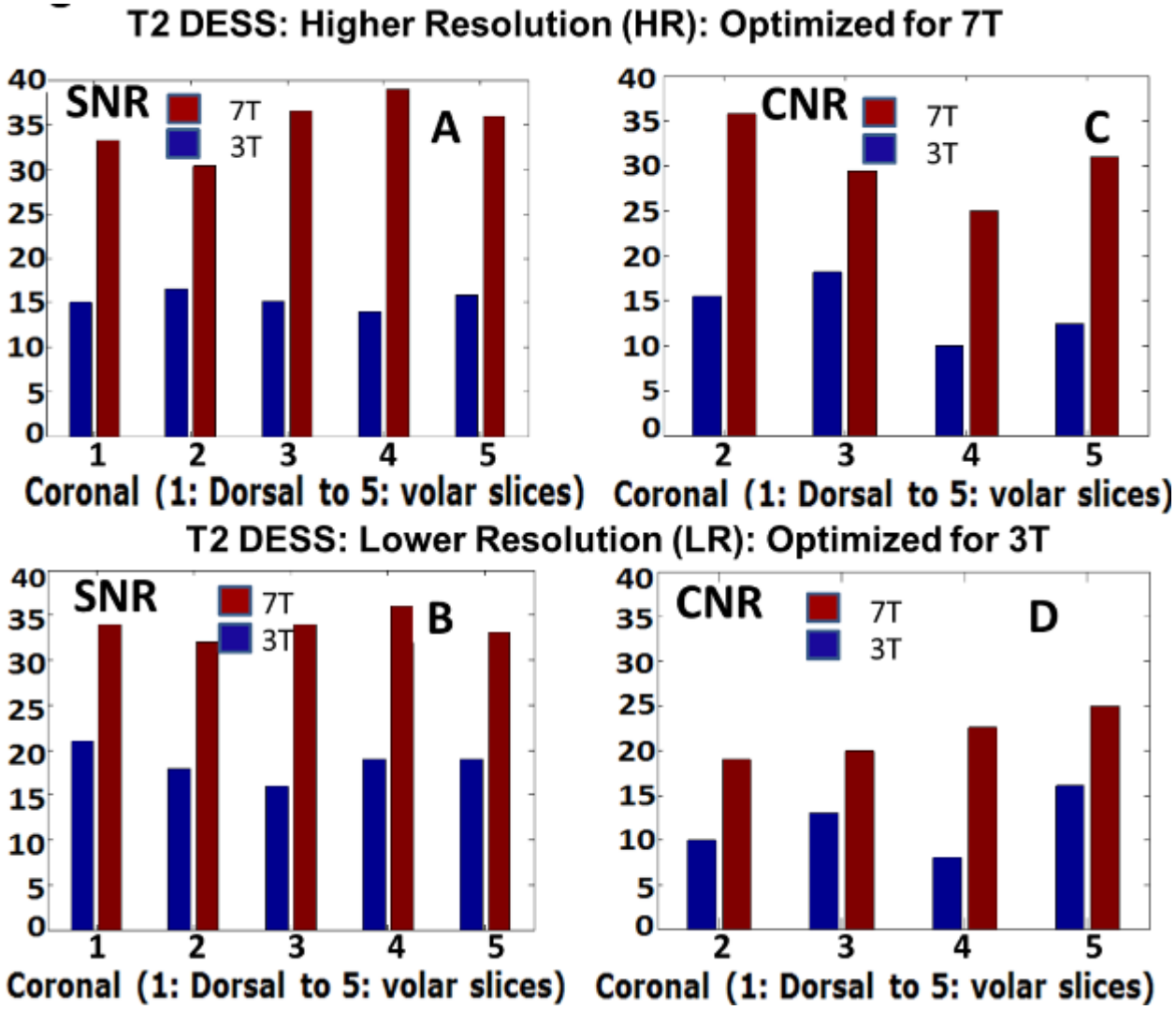

Figure 5.4 SNR and CNR charts for T1 VIBE images.

(A and B) and (C and D) represent SNR and CNR, respectively. The 7T SNR and CNR were ~ 2/1.5 times that of 3T for the HR/LR scans, respectively.

In terms of RF homogeneity (a significant issue [37] at 7T), the T1 VIBE and T2 DESS images (Figure. 5.5) demonstrate uniform excitation in the axial, coronal and sagittal planes, covering the complete volume of the forearm. On the 1st subject, the uniformity was optimized by iteratively fine tuning the RF Tx coil utilizing the experimentally measured B_1^+ field inside the coil's volume of interest. That tune was then utilized for all the remaining subjects. The B_1^+ field homogeneity demonstrated by COV (Coefficient of variation) was calculated to be 21% in the forearm (encapsulated within the coil's volume) [187]. Also, IEC guidelines were followed and the SAR was numerically calculated using an in-house FDTD method [37, 113]. Based on a continuous 1.97μT (averaged over the volume of the arm inside the TEM coil), the average SAR was 2.02 W/Kg and peak SAR was 8.98 W/Kg/10g [187] as IEC 60601-2-33 specifically states that MRI systems must limit locally deposited RF power to under 20 W/kg/10g. In order to demonstrate the comprehensiveness of the 7T RF coil system in upper extremity imaging, the volunteers were scanned in three different regions -- hand, forearm and elbow -- as shown in Figures. 5.1-5.11 and discussed below.

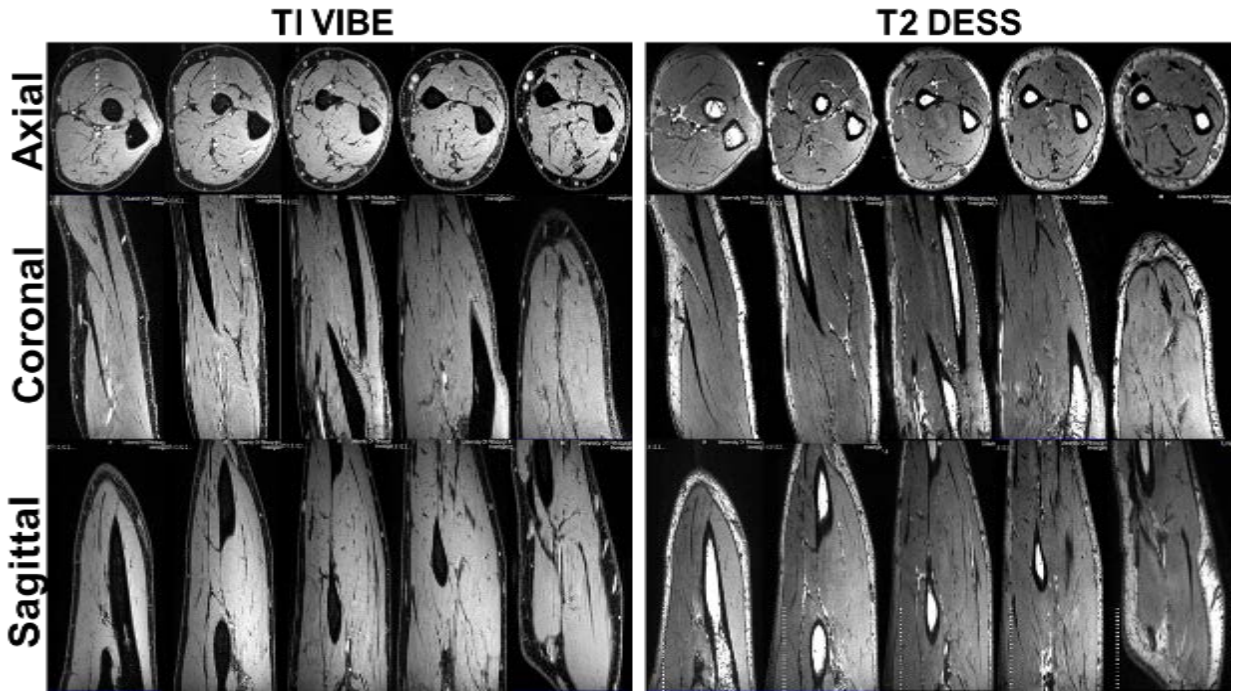

Figure 5.5 7T T1 VIBE and T2 DESS showing homogeneous excitation.

7T T1 VIBE and T2 DESS images of the forearm demonstrating homogeneous excitation in the axial (elbow to wrist), coronal and sagittal planes. The B_1^+ field coefficient of variation was calculated to be 21% in the forearm (encapsulated within the coil volume).

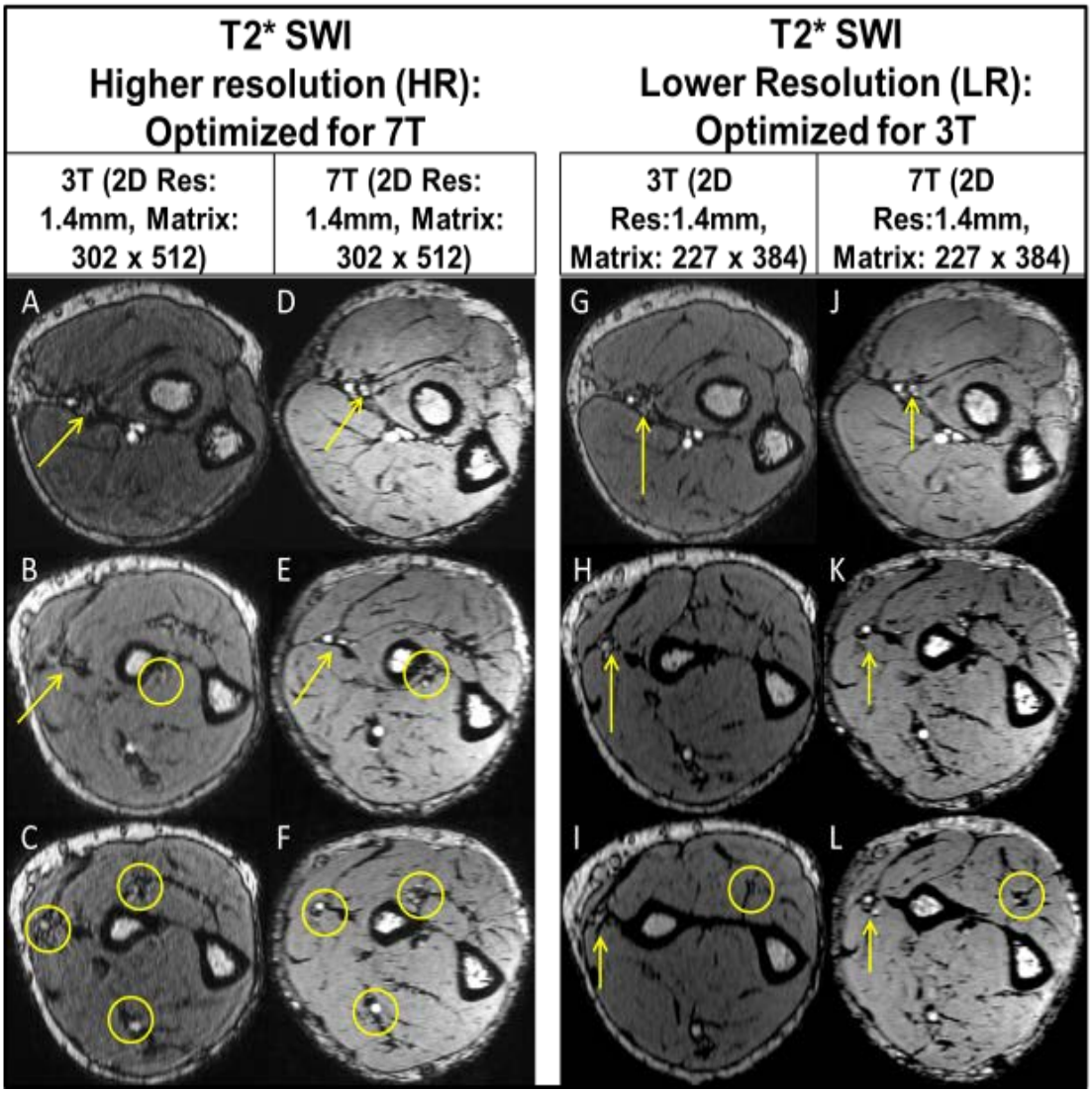

Figure 5.6 T2* SWI (Higher and Lower Resolution) imaging.

3T/7T T2* SWI: Intramuscular vascular branches (off the radial artery) are shown on the HR/LR 3T (A, B, C, G, H and I) images, but are significantly more delineated on the 7T (D, E, F, J, K and L) images. The yellow arrows and circles indicate micro-vessel branches. The above data is from a single volunteer.

5.1.3.1.2 Qualitative Analysis: Figures. 5.1, 5.2, 5.3, 5.4 and 5.6 compare three sequences (T1 VIBE, T2 DESS and T2* SWI) for 3T vs 7T for two cases: i) HR (Optimized for 7T) and ii) LR (Optimized for 3T). Resolution of the small forearm vessels and nerves in both the superficial and deep soft tissues at HR and LR 7T imaging is shown and compared to those at 3T. Delineation of the muscle fibers/fascial plane interfaces as well as the cortical bone/soft tissue interfaces is enhanced at 7T, illustrating the benefit of higher CNR.

5.1.3.1.3 Image Quality and Artifacts Evaluation: Table 5.3 lists all of the results of the qualitative analysis regarding image quality and artifacts. The overall image quality of T1, T2 and T2* images at 7T is significantly higher when compared to that at 3T. The overall total of artifacts increased from 3T to 7T, but these did not impact the image quality.

5.1.3.2 In-vivo Imaging

5.1.3.2.1 T1 VIBE and T2 DESS: Figure. 5.7 shows high resolution forearm and elbow T1 VIBE and T2 DESS 7T images. The elbow images show the median, radial and ulnar nerves as smaller branches of the median nerves. Three T1 and T2 comparison images show various anatomical structures (close to the hand, middle of the forearm, and the elbow). These include fine delineated fascial planes, nerve fiber bundles, major arteries and smaller branches, fine cartilagenous boundaries with a bright signal showing synovial fluid in between, and joint anatomy and bones (radiohumeral with trabecular detail and trochlea of ulna in the forearm).

A1 (T1 VIBE): Radial and Median nerve delineation;

A2 (T2 DESS): It shows the ulnar nerve (arrow);

B1-B3 (T1 VIBE) and corresponding T2 DESS (B4-B6): show three axial slices (close to elbow, forearm, and close to wrist) that depict radial, median and ulnar nerves (yellow arrows, circles) in addition to the major arteries (red arrows); Note that there are motion and pulsatile flow artifacts (band of bright points) from the median artery in the anterior to posterior phase encoding direction;

C1-C2: (T1 VIBE) and C3-C4: (T2 DESS) show joint anatomy depicting bone, cartilage, and synovial fluid.

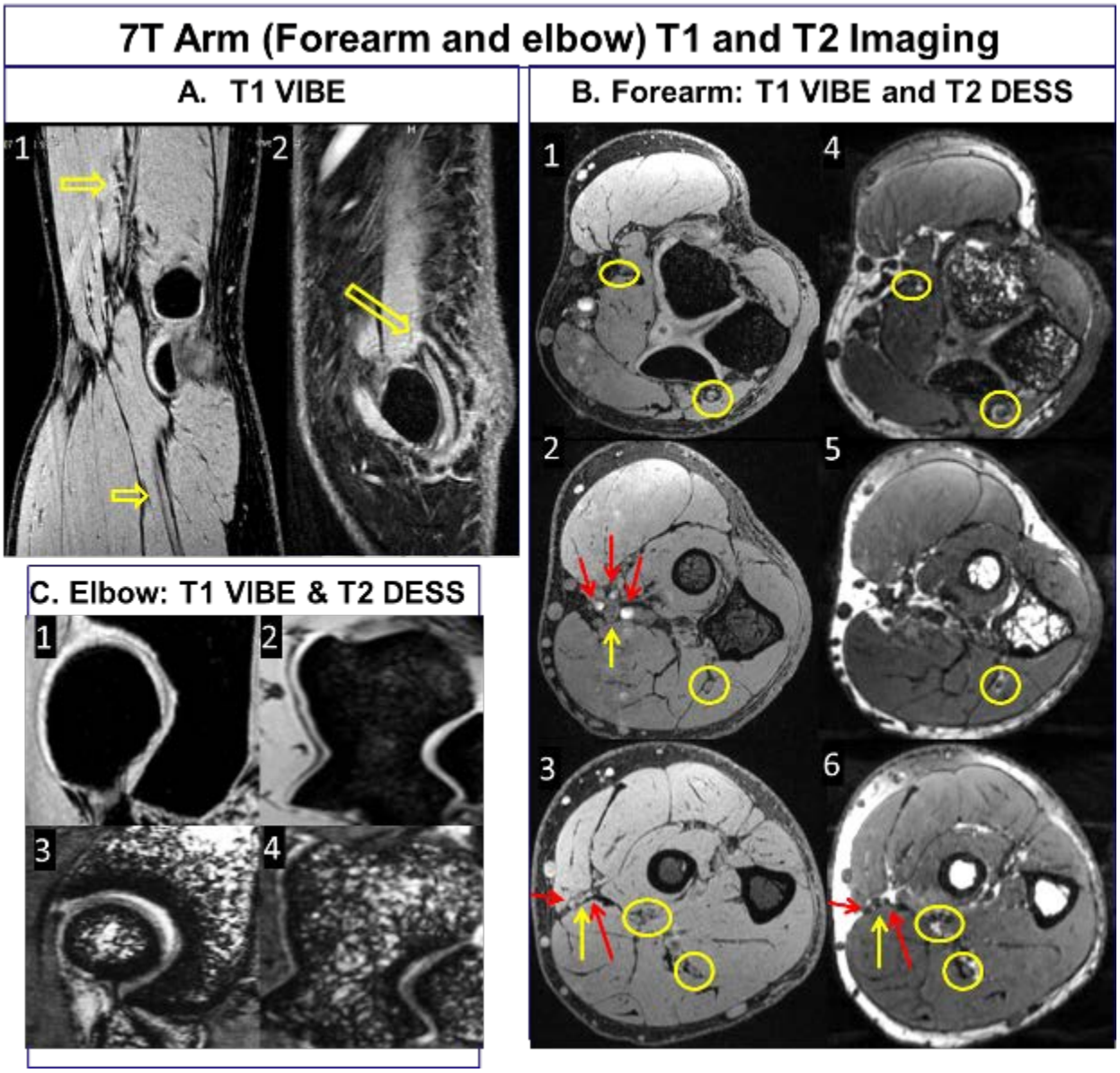

Figure 5.7 7TArm (Forearm and elbow) T1 and T2 imaging.

5.1.3.2.2 Susceptibility Weighted Imaging (SWI): Figure. 5.8 displays SWI [199] images which show macro and micro vessels in addition to vessel walls without the use of any kind of contrast dye/liquid. In comparison to the T1 VIBE slices in the top row, the SWI in the bottom row clearly depicts the arterial vascular pattern and muscular perforators, highlighting the importance of SWI at ultra-high fields.

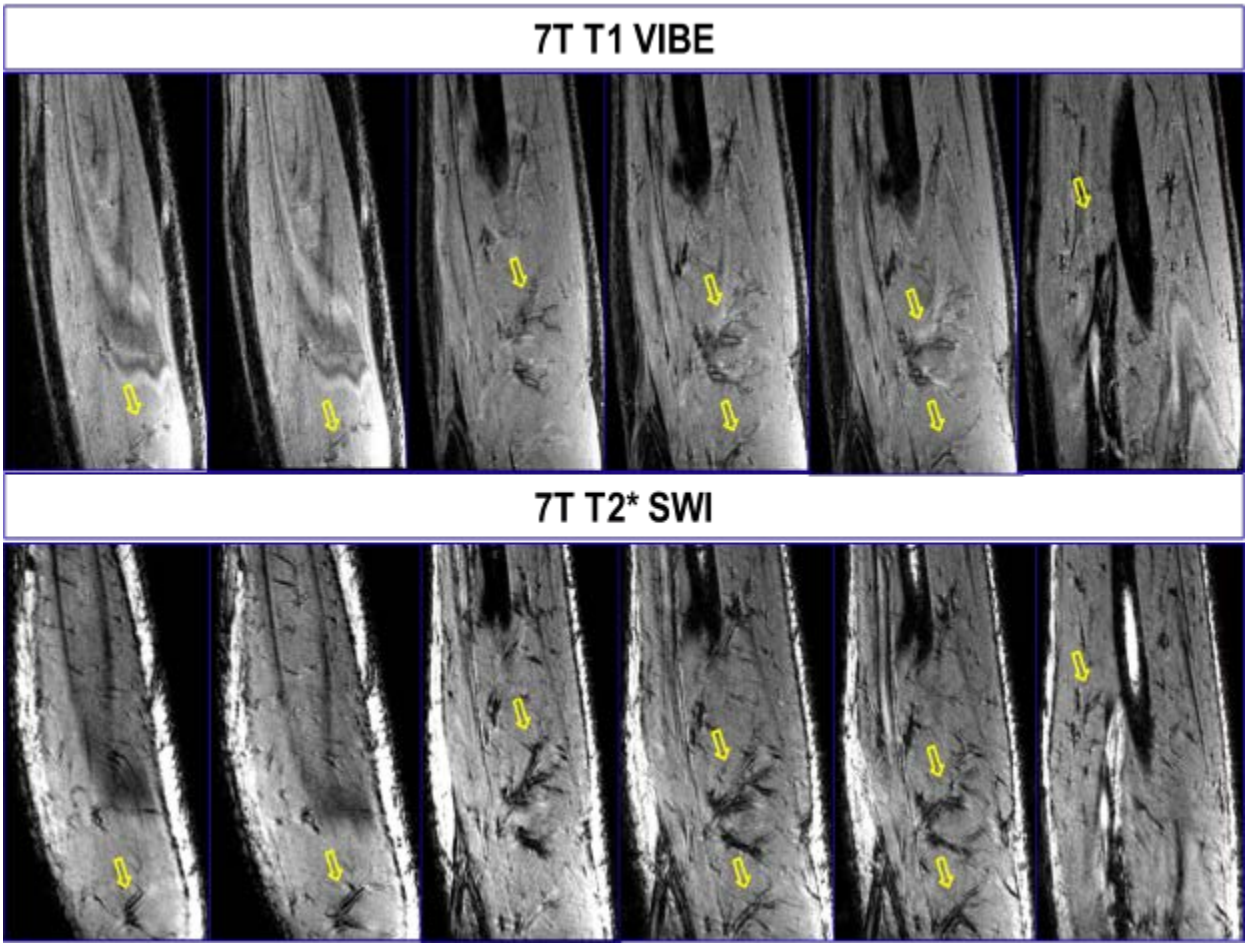

Figure 5.8 Comparison of T1 VIBE and T2* SWI.

7T T2* SWI (bottom row) show marked enhancement of vascular patterns of arteries, veins and muscular perforators (marked with yellow arrows) when compared to the T1 VIBE images (top row).

5.1.3.2.3 Diffusion Tensor Imaging (DTI): Figure 5.9 presents forearm nerves where 3D volume rendering and fiber tractography are shown. The quantitative track analysis results are shown in Table 5.4. The hand and forearm nerves correspond to the known anatomic distribution of the radial, ulnar and median nerves. Figure 5.9 shows Top (A to I) and bottom (1 to 5) row representing 7T DTI with T1 VIBE and T2 DESS validation, and 7T fiber tractography, respectively.

A and B: It shows T1 VIBE and T2 DESS respectively demonstrating all three nerves for validation of the locations of the forearm nerves (yellow circles);

C, D, E and F: It represent ADC, FA, TRACEW, and color-coded DTI map identifying forearm nerves, respectively (Note: The rotation of the T1 VIBE and T2 DESS images to match the DTI images);

G and H: An FA map in sagittal view showing median (m) and radial (r) nerves using multiple intensity projection (MIP);

I: It demonstrates multiple intensity projection (MIP) of combined m and r nerves;

1, 2 and 3: It shows DTI FA maps demonstrating separate forearm nerves with anatomical validation (yellow rectangles) side by side;

4 and 5: It demonstrate 3D DTI and DSI rendering showing forearm nerves tractography, respectively.

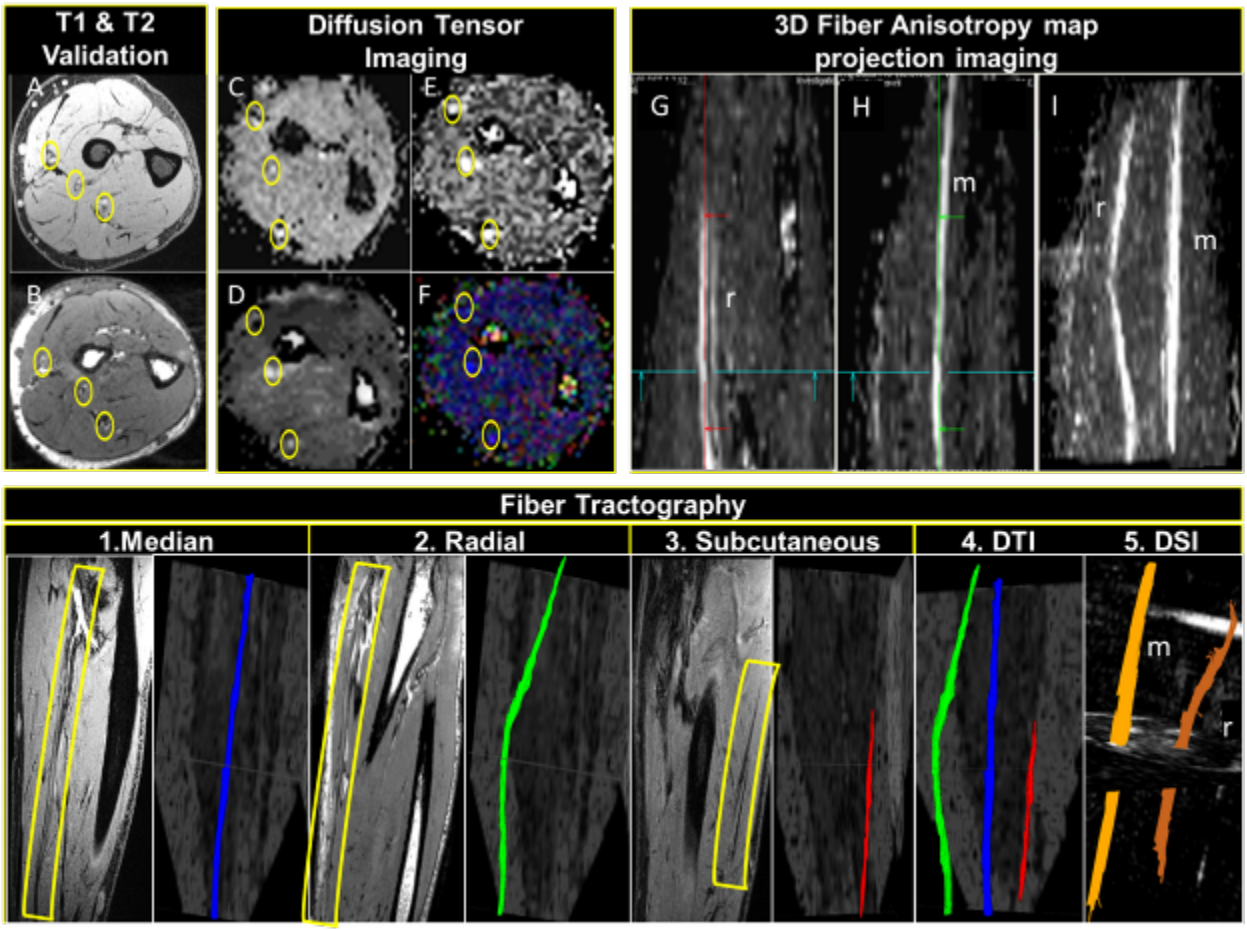

Figure 5.9 DTI imaging.

Table 5.4 Quantitative DTI track analysis values for forearm nerves as shown in Figure. 5.9 (FA: Fiber Anisotropy, ADC: Apparent diffusion coefficient, Ax: Axial/Longitudinal, Diff: Diffusivity, sd: standard deviation, and Rad: Radial).

Tract	Nerve 3	RN_Nerve1	MN_Nerve2
FA mean	0.41	0.79	0.62
FA sd	0.07	-	0.12
ADC mean	0.95	0.95	0.92
ADC sd	0.15	0.25	0.19
Ax_diff_mean	1.33	1.59	1.53
Ax_diff_sd	0.19	0.63	0.31
Rad_diff_mean	0.71	0.57	0.59
Rad_diff_sd	0.12	0.10	0.19

5.1.3.2.4 Time of Flight (TOF) Imaging: Figure 5.10 demonstrates not only more highly anatomical structural hand and finger images but also non-contrast enhanced angiography images. The hand and finger images depict first and second order arteries (superficial palmar and deep palmar arch), smaller proper palmar digital arteries (fingers), and fine arterial branches (finger tips).

A (TOF): It demonstrates eight proper palmar digital arteries (two of them are yellow circled), digital tendons and synovial sheaths in axial view;

B (T1 VIBE): shows proper palmer arteries and two proper palmer digital arteries in thumb and cross-sectional transmetacarpal view, highlighting intrinsic muscles, flexor digitorum superficialis and profundus tendons apparatus with synovial sheaths, ligamentous structures, and inter-metacarpal vasculature.

C demonstrates multiple intensity projection (MIP) of the hand vasculature;

(D, E and F): It shows TOF (non-contrast enhanced MR angiographic) images of the palmar and digital microvasculature in the hand;

G demonstrates a 3D view of volume rendering texture.

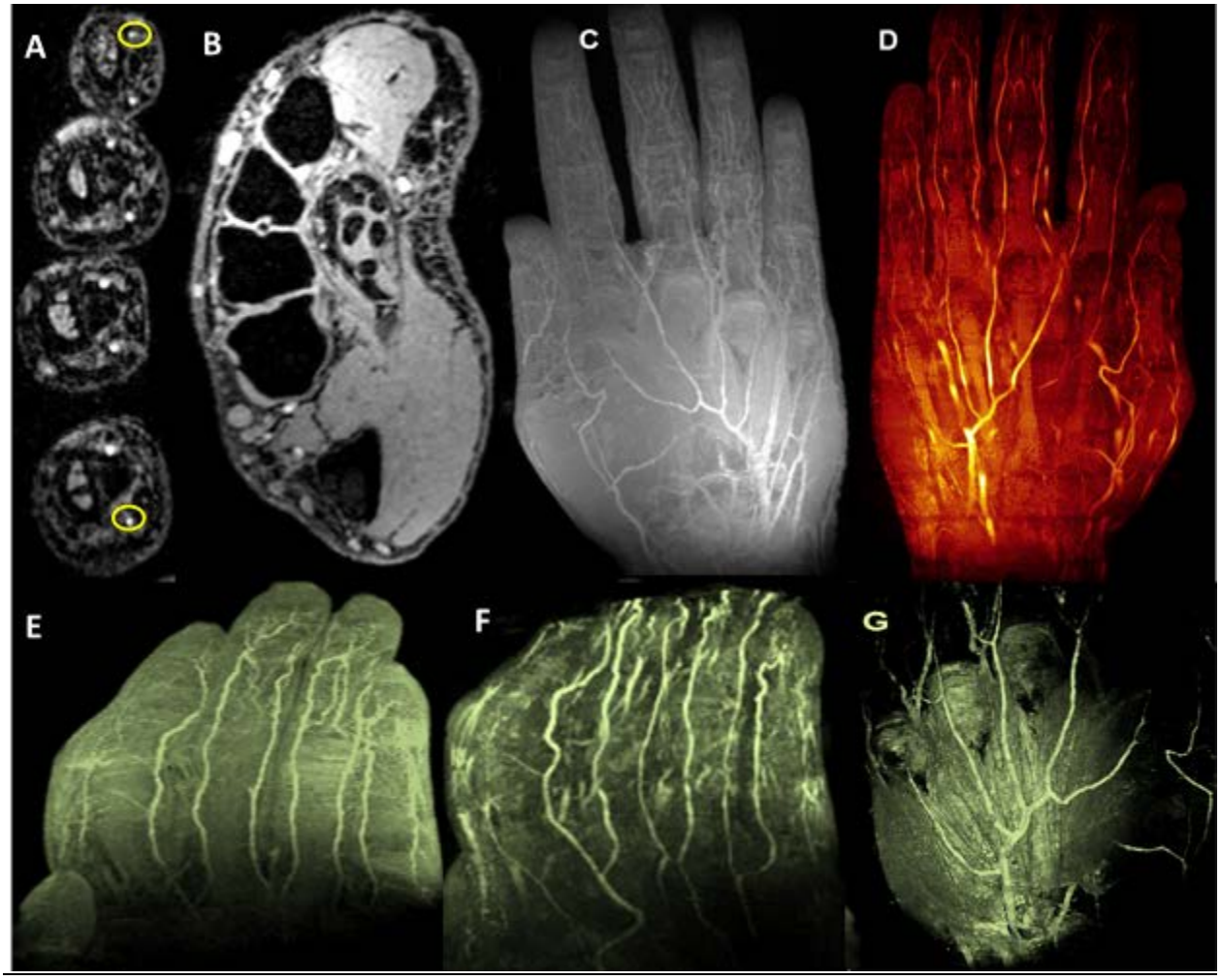

Figure 5.10 7T Hand imaging.

5.1.3.2.5 Vasculature segmentation: Figure. 5.11 shows the selected area of interest and the whole segmented forearm vasculature from T1 VIBE multiple intensity projection images. Figure. 5.11 also shows the major artery (ulnar) and part of the brachial bifurcation

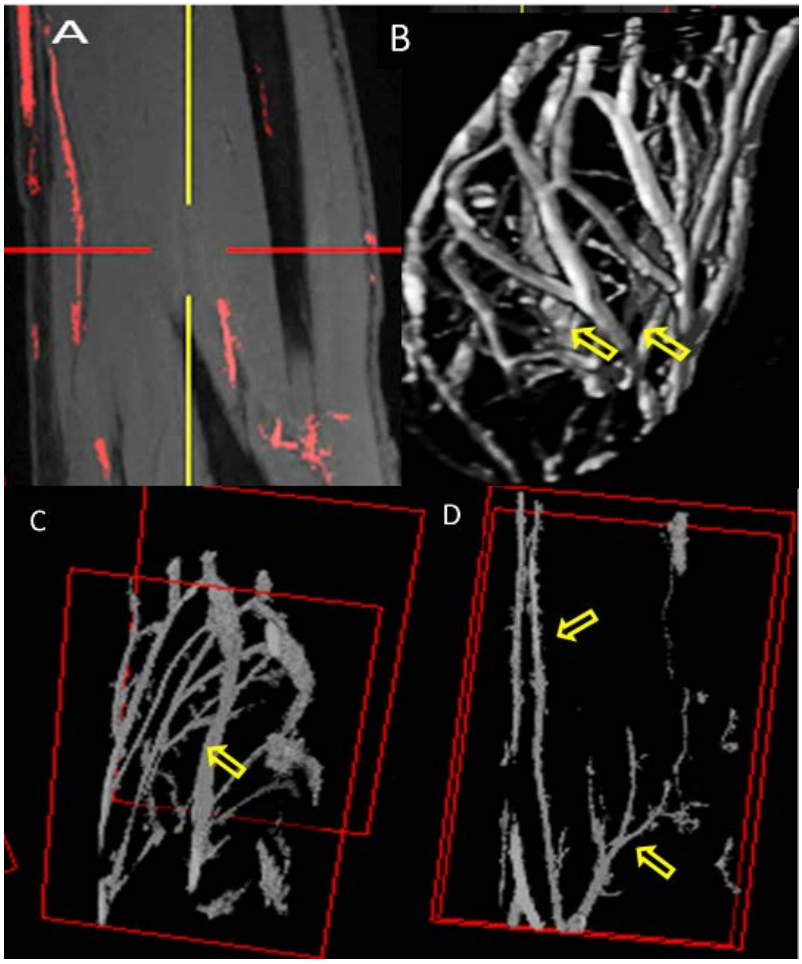

Figure 5.11 7T Vasculature segmentation.

A presents a coronal image as an example of the paint grows segmentation method using T1 VIBE images. B displays forearm vasculature segmentation (3D view) showing the brachial artery and its branches [198] as well as the venae comitans and superficial arteriovenous networks. C shows the complete ulnar artery (arrow) and D presents the radial (arrow) and brachial bifurcation (arrow) in the forearm.

5.1.4 DISCUSSION

While there are no upper extremity commercial coils available at 7T (except [185]), a customized 7T RF coil was built and compared with available extremity coils at 3T with similar receive elements and comparable dimensions. The use of a combined transmit and receive coil with a small filling factor would be favorable to detect receive signals from a homogeneously excited zone of anatomy of interest. A few studies [150, 152, 201, 202] have shown that the SNR obtained from a combined transmit and receive only system could be higher even with a limited FOV. In parallel imaging, the noise distribution is heterogeneous throughout the images, so SNR calculation is approximate but won't be exactly accurate using the ROI method (signal mean in anatomy of interest and noise standard deviation in background). One detailed coil analysis study [203] covers the noise pre-scan method (pseudo-replica method). When comparing a birdcage coil to a TEM coil, the current produced in end rings of the birdcage coil can generate a considerably high magnetic field component, which is coaxially aligned with the B_0 static field, and therefore does not result in spin excitation. Such a component can increase Ohmic loss by inducing conduction currents in tissue [204]. Other groups have developed birdcage-based commercial coils and HEM-mode-based resonators demonstrating promising imaging capabilities limited to the wrist [185, 186, 205]. In contrast, and to our knowledge, our current study is the first to explore the utility and relevance of 7T UHF MRI for the upper extremity encompassing the hand, wrist, forearm and elbow.

The quantitative analysis performed on the T1 VIBE and T2 DESS images (Figures. 5.1, 5.2, 5.3, and 5.4) demonstrates that higher SNR/CNR were achieved at 7T, almost twice those of 3T (most especially in the HR protocol). As with parallel imaging, the noise distribution is heterogeneous throughout the images, therefore SNR calculation could be a crude approximation using the ROI method: signal mean in anatomy of interest over standard deviation of the noise in background. Additionally, Figure. 5.5 shows that homogenous excitation (a typical hurdle for 7T imaging) is quite possible for the forearm with coverage that extends from wrist to elbow. As a part of the qualitative analysis seen in Figure. 5.1, the T1 VIBE images at 7T have less overall noise when compared to the 3T images as the conspicuity of small vessels is superior. T2 DESS imaging (Figure. 5.3) shows improvement in nerve signal and better contrast between muscle planes and visualization of finer osseous trabecular detail at 7T when compared to 3T. In Figure. 5.6, there is greater contrast and delineation of cortical bone and improved detection of small vessel detail at 7T. The high resolution obtained with 7T is clearly not achievable when utilizing 3T, as demonstrated in Figures. 5.1, 5.2, 5.3, 5.4 and 5.6.

Diffusion-based MRI is utilized as a non-invasive, non-disruptive strategy for sequential assessment of forearm nerves. It is quantified by water diffusion parameters (FA and ADC) as indirect correlates or surrogates of neuroregeneration after transection repair or transplant related nerve outcomes. In order to increase the reliability and interpretation of results, DTI derived maps [FA, ADC, and color-coded] are defined in conjunction with T1 and T2 anatomical validation. High resolution imaging of peripheral nerves may have application in the detection of neuropathy and monitoring to assess disease progression or response to appropriate therapy [133, 158] [125]. Moreover, volume rendering and 3D depiction of the course of the

forearm nerves (as shown Figure. 5.9) may prove useful in the broader realm of reconstructive surgical or vascularized composite allotransplantation (VCA) applications. While comparison to 3T (in terms of DTI) was outside of the scope of this study, the presented 7T images show very good delineation of the forearm nerves without the use of contrast agents.

7T TOF imaging (shown Figure. 5.10) and the corresponding vascular segmentation (shown in Figure. 5.11) allow depiction of the macro and microvascular anatomy of the hand, forearm, and palmer region (and wrist) in 2D monitoring of microvascular integrity as it relates to certain vascular disease processes [165, 206]. In addition, SWI (Figure. 5.8) could be especially useful in visualizing various macro or micro-vascular pathologies secondary to vascular trauma, thrombotic/embolic occlusion, and neovascularization of tumors, and in high-resolution MR venography [165, 167, 182]. While contrast enhanced imaging is utilized extensively [200], the fact that 7T high quality vascular imaging can be accomplished without the use of intravenous contrast is invaluable in patients with organ transplantation, autoimmune vasculitis or diabetic peripheral vascular disease as these conditions often have concomitant renal vasculitis and/or renal insufficiency.

MR angiography using 1.5T imaging has been previously described in evaluating neuropathic leg pain [207] and other diabetic vasculopathy [208]. 3T imaging has been reported in evaluation of the brachial plexus [209, 210]. In addition, 3T MR angiography has also been used in imaging of intracranial vessel disease/vasculitis [159, 160]. 7T MR angiography has also been explored [161], specifically in the upper extremity focusing on wrist [211] or hand [205] but

limited to the palmar vasculature. The work presented here expands higher resolution MRA to other, including the digital vasculature and capillary networks in the pulps of fingers.

The choice of CT Angiography (CTA) vs MRA or vice versa for specific indications is still a debatable issue [212-214]. The choice of CTA usually depends upon the region of interest -- involved in either neuro[215-217], coronary [192, 218-221] or rest of the body [222, 223] related applications. However, the merits of MRA over CTA cannot be ignored especially in the case of UHF 7T MRA. Work in 7T TOF, nCE MRA, SWI, and other MR based methods (DCE_MRA, MRV, DTI, etc.) could open new possibilities for nCE vascular imaging, as confirmed by our study and validated by other research studies [161, 182, 223-227]. While CTA faces contrast-agent related nephrotoxic or anaphylotoxic risks, it has the advantage of a faster scan time. which could be important in emergent clinical indications such as pulmonary embolism or acute cerebrovascular disease [217]. Earlier work, however, has shown that the diagnostic performance of 3T CE whole-heart coronary MR angiography approaches the diagnostic performance of 64-section CT [228]. In addition, 7T UHF MRI and parallel imaging with a higher number of receive channels could produce highly improved SNR/CNR, faster scanning time, and a significant advantage for repeated or longitudinal/sequential imaging applications [228-230]. Furthermore, the avoidance of radiation by MR offers a critical advantage in pediatric imaging, especially of the craniofacial skeleton (in concussion or traumatic brain injury) [231]. When compared to MR related research studies, a significant growth in research utilization of CT has been observed [232]. However, there is need for more MRA studies (especially utilizing UHF MRI) [161, 182, 223-227]. Non-invasive methods like nCE MRA, TOF, SWI, and diffusion related methods have very high potential in safe, non-radiation, nCE detection of high-signal-intensity plaque, coronary

arterial wall disease [218], and atherosclerotic vascular disease [233, 234] as well as in a host of other indications [161, 182, 215-219, 222-224, 235]. UHF 7T imaging can alleviate and overcome several imaging challenges encountered in imaging neurovascular disease at lower field strengths (1.5T and 3T), such as venous contamination obscuring underlying arterial architecture or delineation of contextual anatomical structures [217] .

5.1.5 CONCLUSION

High quality non-contrast enhanced ultra-high resolution neuro-vascular upper extremity imaging is possible at 7T. High quality 7T images were obtained using T1 VIBE, T2 DESS and T2* SWI sequences as well as TOF, DTI, and DSI sequences in conjunction with a custom-designed RF coil system. Analyses demonstrate that 1) CNR/SNR at 7T are almost two fold (for T1 VIBE and T2 DESS sequences) of that achieved at 3T for upper extremity applications and 2) broader clinical potential is present for 7T imaging in musculoskeletal applications.

5.2 CASE REPORT: ULTRA-HIGH FIELD (7T) MAGNETIC RESONANCE MUSCULOSKELETON IMAGING IN UPPER EXTREMITY ALLOTRANSPLANTATION – PRELIMINARY RESULTS IN VASCULAR COMPOSITE ALLOTRANSPLANTATION (VCA).

5.2.1 INTRODUCTION

Reconstructive arm transplantation is a clinical reality, with more than a dozen countries across the world performing unilateral and bilateral transplantation [236]. Statistics indicate that upper extremity [UE] trauma constitutes 39% of combat injuries [237-239]. As of 2005, 1.6 million civilians suffer from limb loss in the US alone. Of these, 34,000 had major loss of an UE [237]. These numbers are expected to go up to 3.6 million by 2050 [236, 237]. If only 1% of this population qualifies to undergo transplant surgery, that mandates the need for additional transplant infrastructure in addition to standardized pre and post-surgical evaluation and monitoring methods. Over the past 15 years, 17 patients have undergone Upper Extremity Transplantation (UET) in the United States alone. Multiple conventional imaging modalities have been used to screen patients as well as monitor outcomes after UET. These include X-ray [lungs, respiratory tract, bone

density], CT angiogram [vasculature, adjacent bone and soft tissue (injecting IV through blood vessel], and MRI [fMRI pre and post-transplant brain assessment]. MRI is the undisputed choice of imaging modality when it comes to monitoring and evaluating soft tissue conditions. These can include peripheral neuropathy, dystrophic lesions, nonosseus structures, avascular necrosis, occult fractures, nerve and joint diseases, carpel tunnel release hamartomas, rare neoplastic lesions, sports-related injuries, orthopedic and a variety of pathological hand conditions, and vastly growing pre and post-transplant applications [28, 127, 240-244]. Commercially (<=3T) available MR scanners lack the capability to provide critical anatomical resolution when compared to ultrahigh (UHF) field scanners (>=7T), which enable significantly superior SNR, higher image resolution, and reduced scan time [6].

An early detection of vascular abnormalities and other irregularities [connective tissue disorders, collagen accumulation, vascular wall injuries, extreme micro vessels damage, including endothelial impairment, lumen narrowing and fibrosis of the microvasculature, typically characterized by pathobiology [245] can be extremely useful to investigate the pathogenesis in neuropathy and transplant applications. Intra-arterial digital subtraction angiography [28] is still considered the reference standard for the diagnosis of vascular pathologies of the fingers. As an invasive procedure, the inherent limitations have made it not so widely used in practice. Recent years have seen the clinical implementation of magnetic resonance angiography (MRA) with and without the use of contrast material as a reliable and accurate modality for evaluation of vascular pathologies of the hand and fingers [28, 243]. Imaging the small vessels of the finger, however, faces specific challenges. Specifically, high resolution is necessary to accurately depict the digital vessels, which are often < 1mm in diameter. To our knowledge, the current study is the first ever

case report of 7T imaging after UET. We present results from a bilateral UET subject 4 years after surgery as part of a post–transplant clinical MR assessment.

5.2.2 MATERIALS AND METHODS

All of the 7T MR experiments were performed on a 7T Siemens Magnetom scanner. A 38-year-old subject (female) with a bilateral hand transplant was recruited under a university approved IRB, and informed consent was obtained from the participant. In-vivo images were acquired using an actively detuned TEM resonator (with a two-port quadrature hybrid drive) in conjunction with an inductively decoupled eight channel receive only insert array (each one is 18x8 cm^2) custom designed for UE (description is provided in Chapter 4). The subject was positioned in a comfortable prone position with the coil being in the center of the magnet. Imaging parameters were optimized to achieve high resolution, SNR, CNR, and minimal scan time.

The selection of an in-house made UE RF coil was made based on the high SNR/CNR it exhibited compared with a 3T commercial extremity coil when used on the same volunteer (same anatomical region with similar orientation). 3D T1VIBE, T2DESS, and TOF MRI were optimized to utilize multi-planar capabilities for evaluating and identifying the size, location, and 3D contextual anatomy of interest. T1VIBE was optimized to provide high-resolution spatial anatomical detail. T2DESS was optimized to improve higher spatial resolution and CNR/SNR. A

non-contrast enhanced TOF MR Angiography technique was used to provide the advantage of a longer T1 relaxation constant at 7T.

3T imaging was performed on the bilateral hand transplant patient using a 3T whole-body MRI system (Tim Trio, Siemens Healthcare, Erlangen, Germany) at New Jersey Hackensack University Medical Center. The 3T parameters were optimized to approximately match the 7T parameters for the purpose of comparison and are listed in Table 5.5. A dedicated eight-channel extremity coil (Siemens, Cleveland, OH, USA) was used at 3T.

Both coils (for 3T and 7T) were positioned in the center of the magnet bore during all imaging sessions. The subject was positioned prone within the coil, with the hands (forearm, and elbow) placed over the head and immobilized with cushions, pads and sandbags to avoid discomfort.

Table 5.5 7T and 3T MR Sequence Parameters.

Field Strength	7T	3T
T1VIBE	TR/TE: 12/4.42 ms Slices: 288 Pixel Res: 0.3 X 0.3 X 0.3 mm^3 FA: 10 Slice Thickness: 0.3 mm Acquisition time: 5:34 min	TR: 12/4.69 ms Slices: 128 Pixel Res: 0.3 X 0.3 X 0.3 mm^3 FA: 10 Slice Thickness: 0.3 mm Acquisition time: 5:27 min
T2 DESS HR	TR: 18/5.22 ms Slices: 238 Pixel Res: 0.34 X 0.34 X 0.4 mm^3 FA: 25 Slice Thickness: 0.4 mm Acquisition time: 6:38 min	TR: 18/5/22 ms Slices: 160 Pixel Res: 0.4 X 0.4 X 0.4 mm^3 FA: 25 Slice Thickness: 0.4 mm Acquisition time: 6:39 min
TOF	TR/TE: 12/4.5 ms Slices: 128 Pixel Res: 0.3 X 0.3 X 0.4 mm^3 FA: 19 Slice Thickness: 0.4 mm Acquisition time: 6:08 min	TR/TE: 27/6 ms Slices: 160 Pixel Res: 0.3 X 0.3 X 0.4 mm^3 FA: 19 Slice Thickness: 0.4 mm Acquisition time: 7:13 min

5.2.3 RESULTS

A primary MR image reviewer and a peer reviewer, both with more than twenty years of experience in radiology and blinded to the status of the subject, independently reviewed all MR images. Images were primarily displayed on Siemens Syngo software and post-processed using a custom written image-processing software package, MIPAV[197].

Double amputee transplant patient 7T imaging data (RH: right hand, LH: left Hand) is shown in Figure 5.12. T1VIBE 7T imaging depicts (A (axial), B, C, E (coronal)), (O (axial- veins and arteries), and (P, Q, R, S (sagittal)) slices. The left hand shows exquisite high resolution anatomy for assessing phalangeal, metacarpal and carpal bone edema, erosion, cartilage, tendon and other soft tissue anatomy in patients, as well as the neurovascular anatomy (proper palmar digital (PPD) arteries) and its branches (including capillaries on finger pulps (B,C,E)). T2DESS imaging (F, G, and H) and (T-W) shows more contrast in identifying the vessels and nerves. TOF imaging ((I-K, X-Z: axial), (L-N, Z1-Z2: 3D volume rendering from Siemens software) clearly shows not only digital arteries but the branches and capillary bed all the way towards the finger tips.

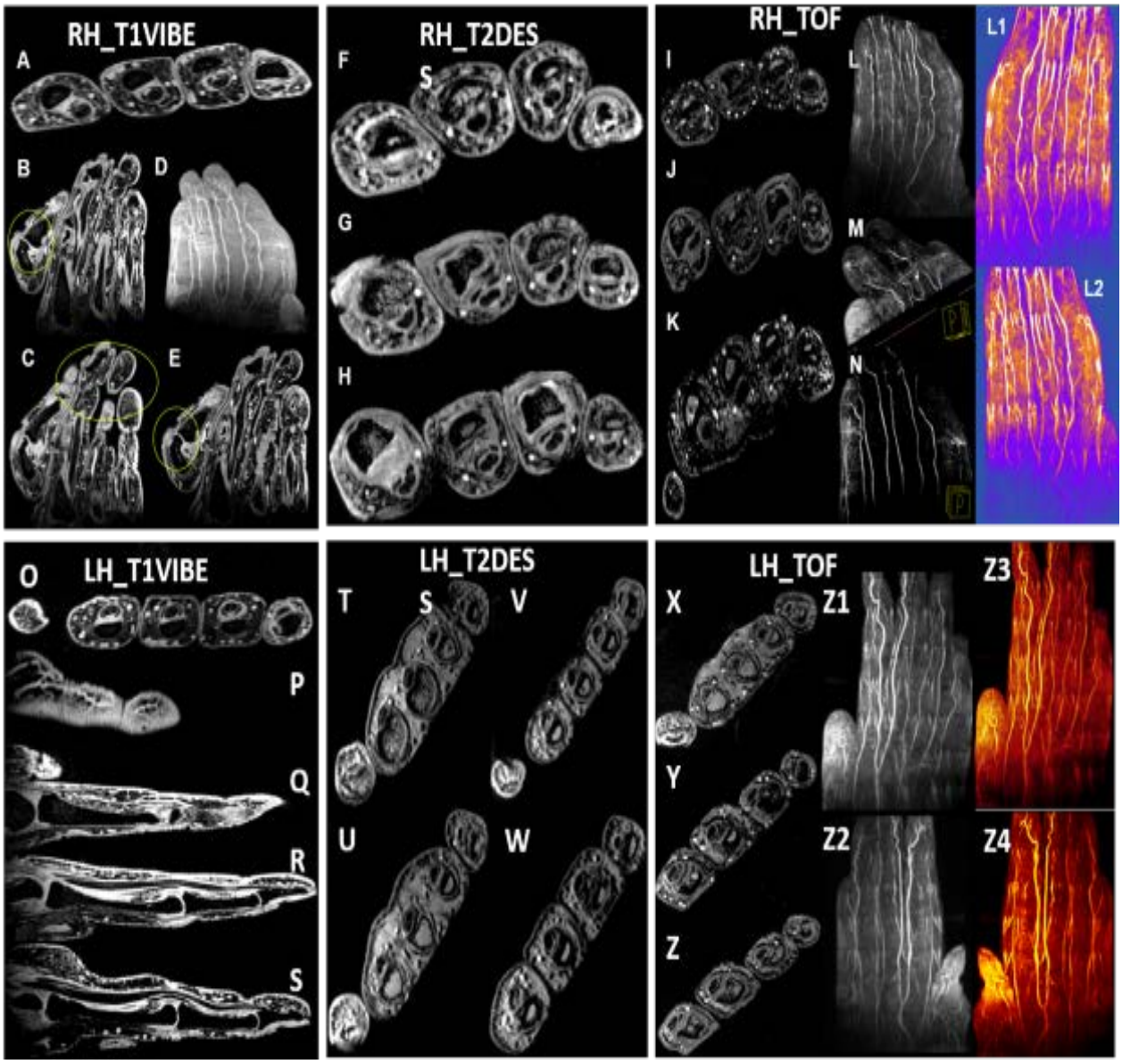

Figure 5.12: 7T left and right hand images of double-amputee transplant patient data (RH: right hand; LH: left hand).

Healthy volunteer data is shown in Figure 5.13. 7T T1VIBE imaging (A (axial), E (volume rendering) for the right hand; C, D (Axial) for the left hand) shows high resolution anatomical detail and smaller vasculature. Volume rendering and intensity projection were performed as shown in Figure 5.13; (F, J) show the right hand (ventral) deep-palmer arch whereas (G, K, L) show the right hand (dorsal) and the superficial palmer arch. (H, M) show maximum intensity projection of the vasculature. TOF imaging (I, M) shows the ulnar artery, common palmer arteries, proper palmer arteries, and digital palmer arteries.

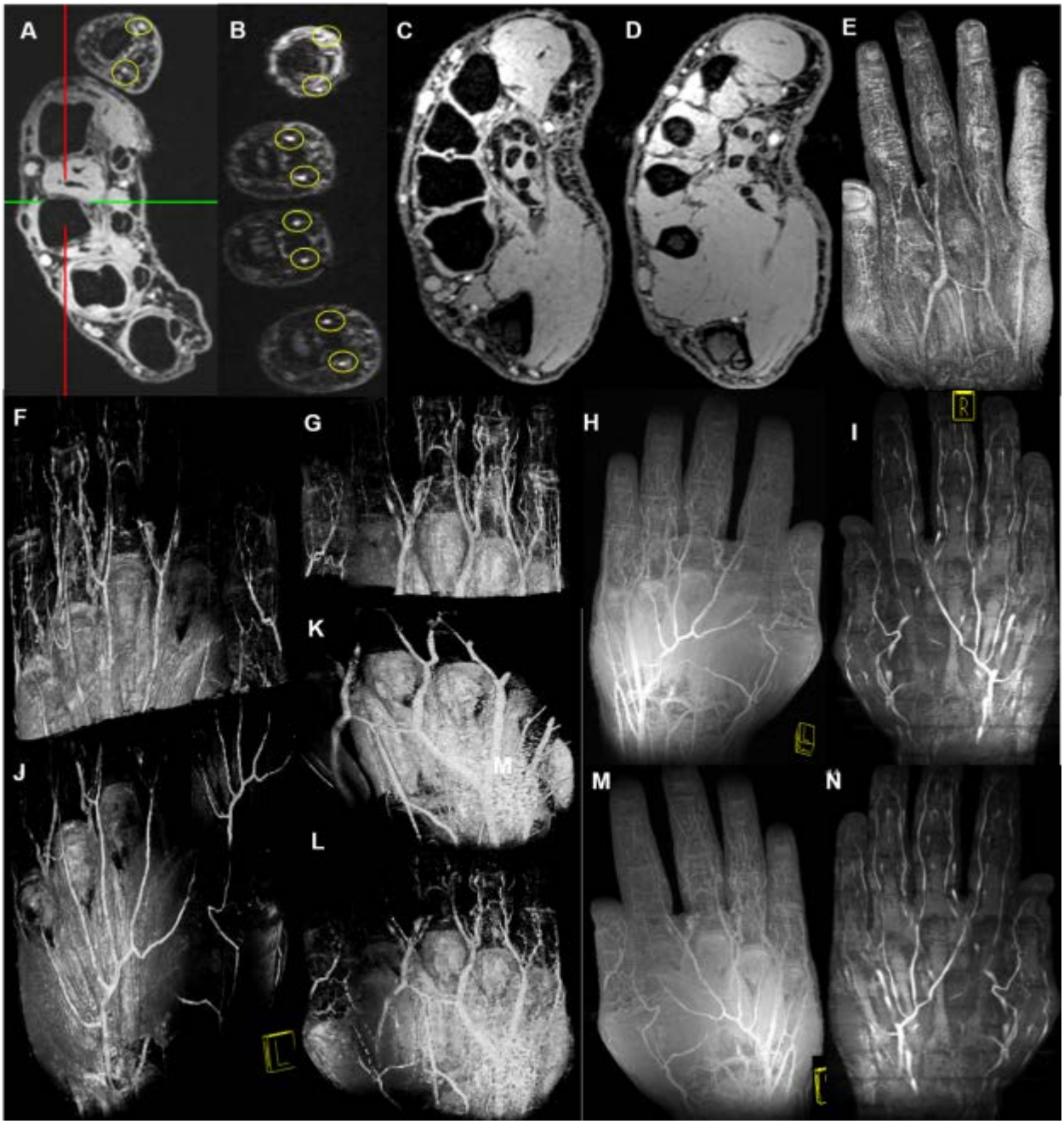

Figure 5.13: T1 VIBE, TOF and volume rendering of healthy volunteer 7T images.

Figure 5.14 shows a comparison of the vessel diameters of the PPD artery of the volunteer and patient's index (I) and middle finger (M). The mean diameters for all four fingers are: Ring finger: 2 ± 0.6 mm (volunteer: V), and 1 ± 0.4 mm (patient: P); Middle Finger: 2.6 ± 0.6 mm (V), and 1.55 ± 0.4 mm (P); Index finger: 1.4 ± 0.4 mm (V), and 0.97 ± 0.4 mm (P); and little finger: 1.55 ± 0.6 mm (V), and 1.23 ± 0.4mm (P).

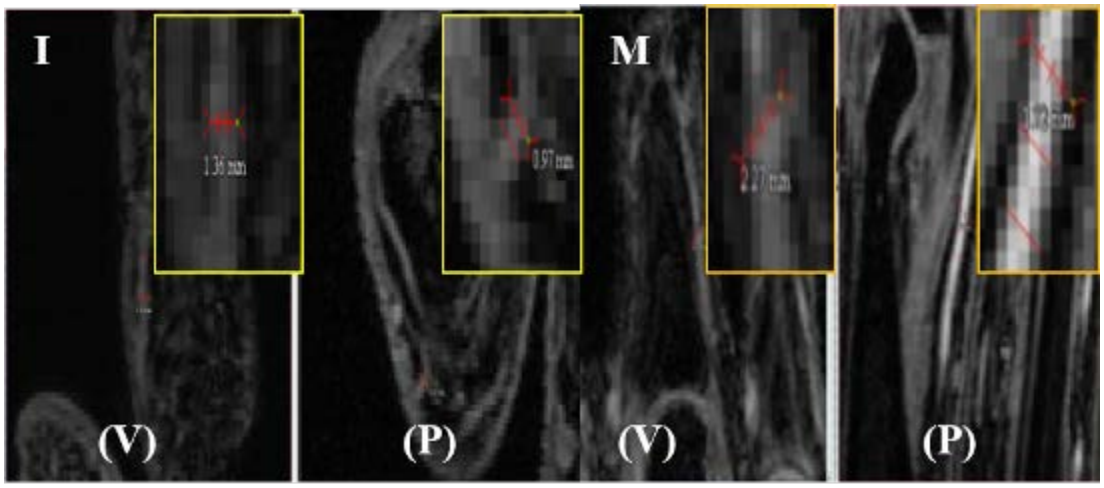

Figure 5.14: 7T Comparison of vessel diameter of PPD artery of volunteer (V) and patient (P) index (I) and middle fingers (M).

5.2.3.1 3T vs 7T

5.2.3.1.1 Time of Flight (Non-Contrast Enhanced) Imaging: Figure 5.15 shows 3T (left hand: A) vs 7T (left hand: B) data. The left hand comparison shows that proper digital palmer arterial branches are clearly visible in the index and middle finger at 7T (yellow arrows). TOF Imaging of the left hand (C, D) images of the double-amputee transplant patient data shows proper digital palmer arterial branches clearly visible in the index and middle finger at 7T (D) when compared to 3T (C), as shown by the yellow oval and circles. TOF Imaging of the left hand (E, F) of the double-amputee transplant patient data shows that proper digital palmer arterial branches, the synovial sheath, and the ligamentous structures are clearly visible in the index and middle finger at 7T (F) when compared to 3T (E), as demonstrated by the yellow oval and arrows.

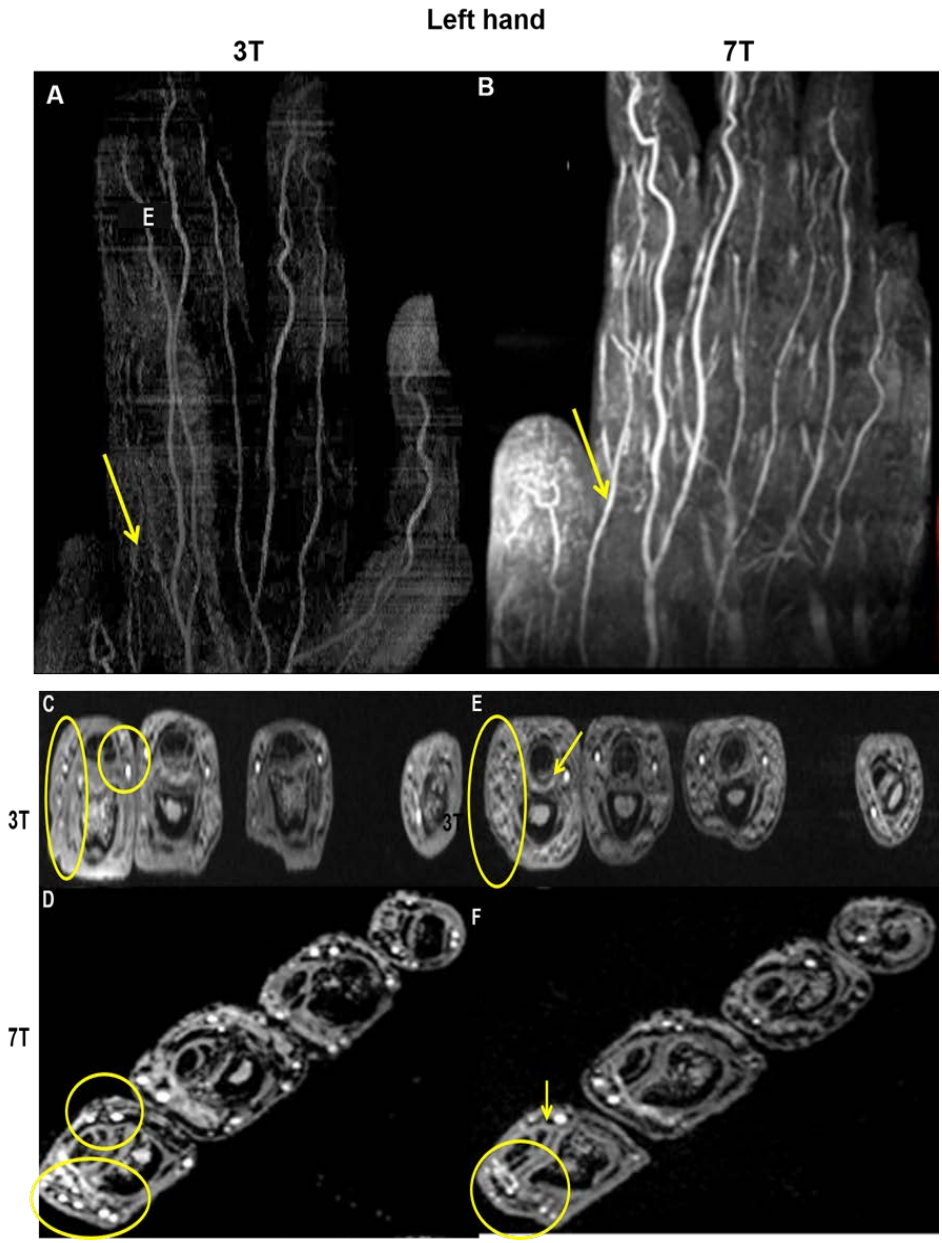

Figure 5.15. 3T vs 7T TOF imaging of left hand images of double-amputee transplant patient data.

Figure 5.16 shows 3T (right hand: A) vs 7T (right hand: B) data. Similar observations to those in Figure 5.15 can be seen.

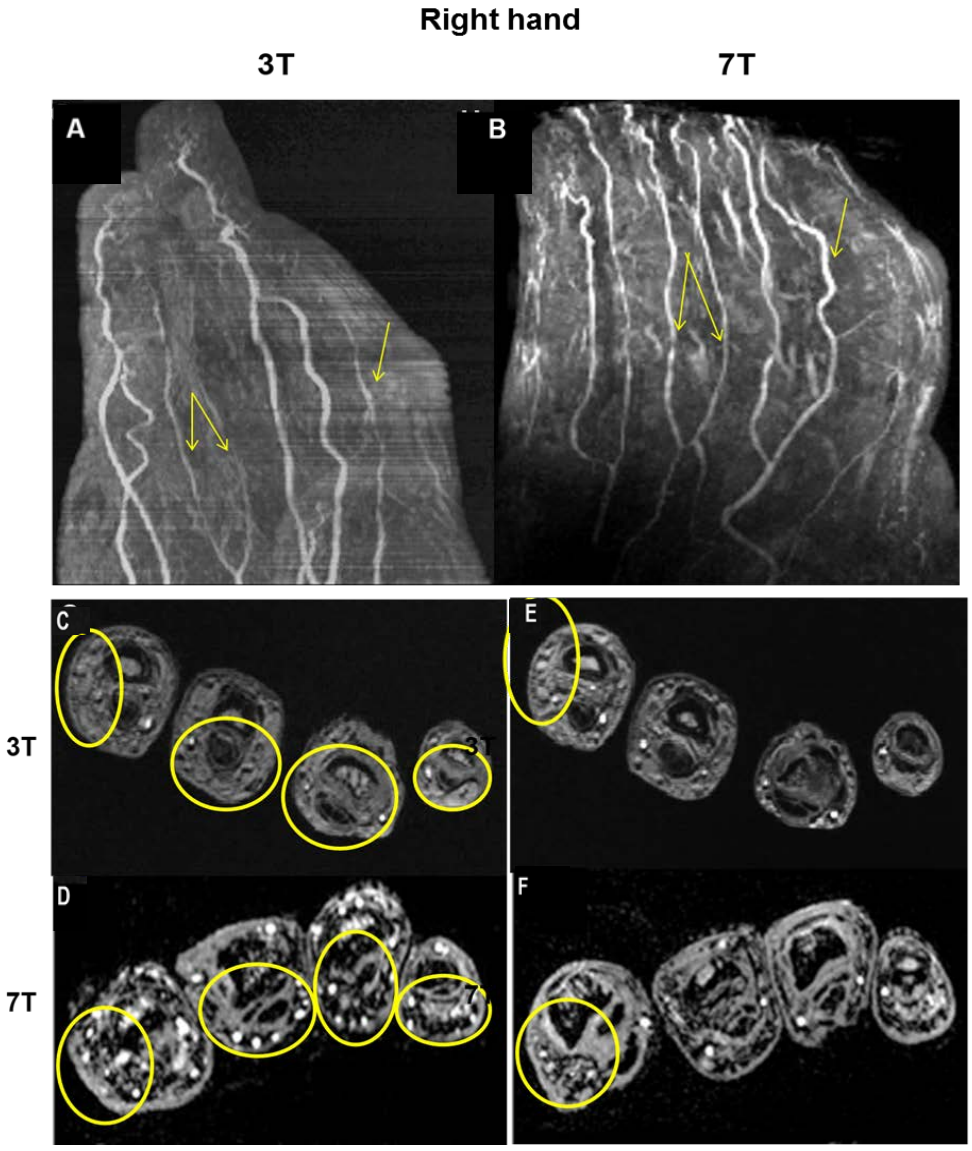

Figure 5.16. 3T vs 7T TOF Imaging of right hand of double-amputee transplant patient data.

5.2.3.1.2 T2DESS imaging: Figure 5.17 shows the comparison of T2DESS images for 3T (left hand : O) and 7T (left hand: P). It demonstrates a very fine delineation of palmer ligament plates (arrow), fibrous sheaths (circle), and bone structures (arrow) in detail, with much higher contrast at 7T. T2DESS imaging of the right hand (Q, R) of the double-amputee transplant patient shows a comparison of 3T (right hand : Q) and 7T (right hand: R). It shows a very fine delineation of tendons, fibrous sheaths, arteries, and bone structures in detail, with much higher contrast at 7T. T2DESS imaging of the right hand (S, T) of the double-amputee transplant patient shows a very fine delineation of fibrous sheaths, tendons, arteries and bone structures with a much higher contrast in 7T.

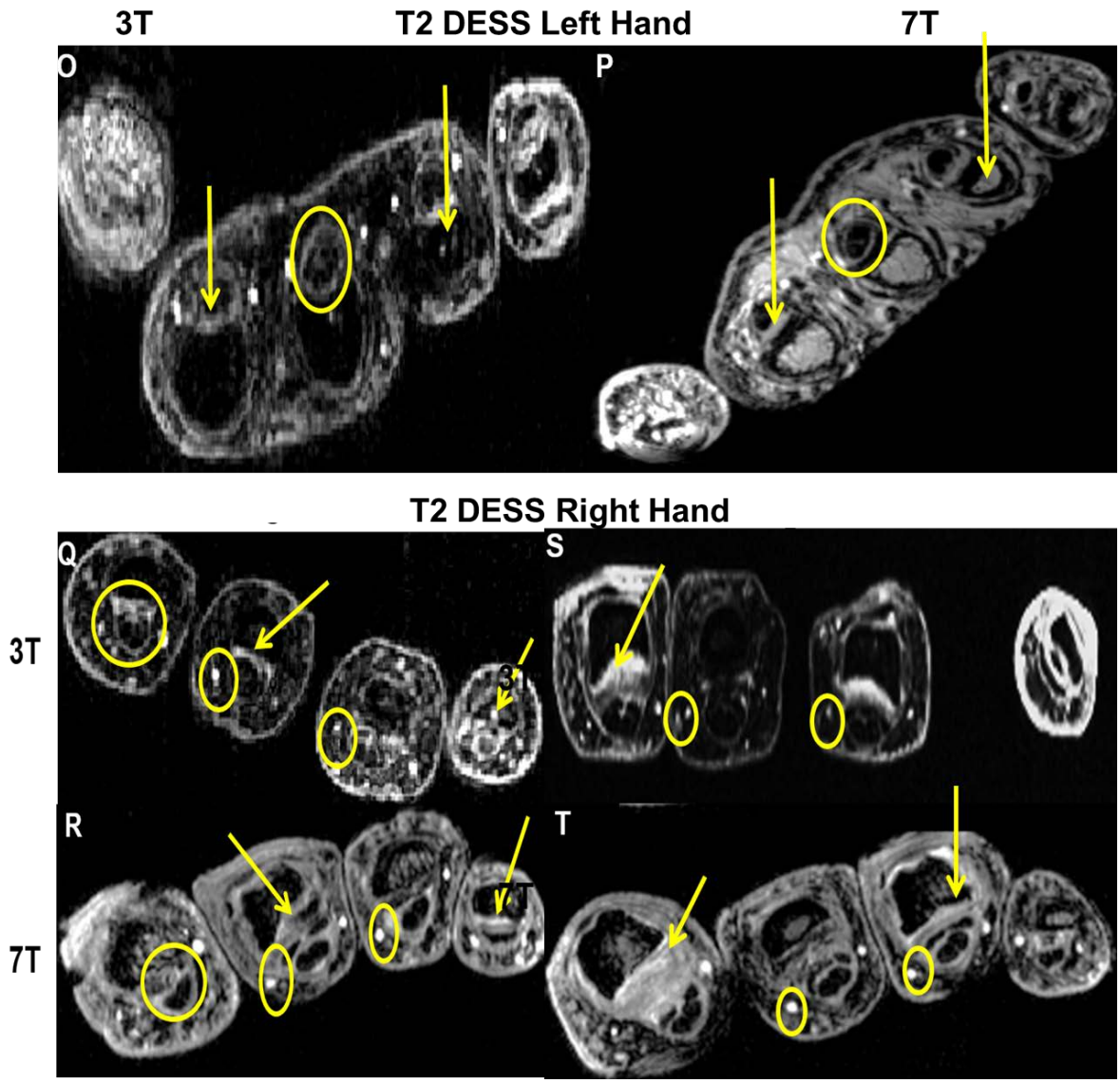

Figure 5.17. 3T vs 7T T2DESS imaging of left hand (O, P) and right hand (Q-T) of the double-amputee transplant patient.

5.2.3.1.3 T1VIBE imaging: Figure 5.18 shows a T1VIBE imaging (left hand) comparison of 3T (U) and 7T (V), demonstrating the various anatomical details viewable at high resolution. V shows a clear distinction between the fibrous and synovial (tendon) sheaths of the finger and flexor digitorum superficialis (profundus) tendon (yellow circles). T1VIBE (left hand: W, X) imaging of the double-amputee transplant patient data is also shown. X shows a clearer distinction of the volar branches of the proper palmer digital branches of the digital arteries, proper palmer artery, capillaries and minute branches of the digital artery at the finger pulps. T1VIBE (Y, Z) imaging of the double-amputee transplant patient data also shows high resolution details of various anatomical structures. Z depicts the palmer ligament plates (yellow circles), annular parts of the fibrous sheath over (synovial) flexor tendon sheaths (red ovals), and the tendons of the flexor digitorum superficialis and profundus muscles (yellow arrows). The 7T right hand images (1, and 2) also depict a fine delineation of digital arterial branches, tendon, and ligaments when compared to its counterparts at 3T.

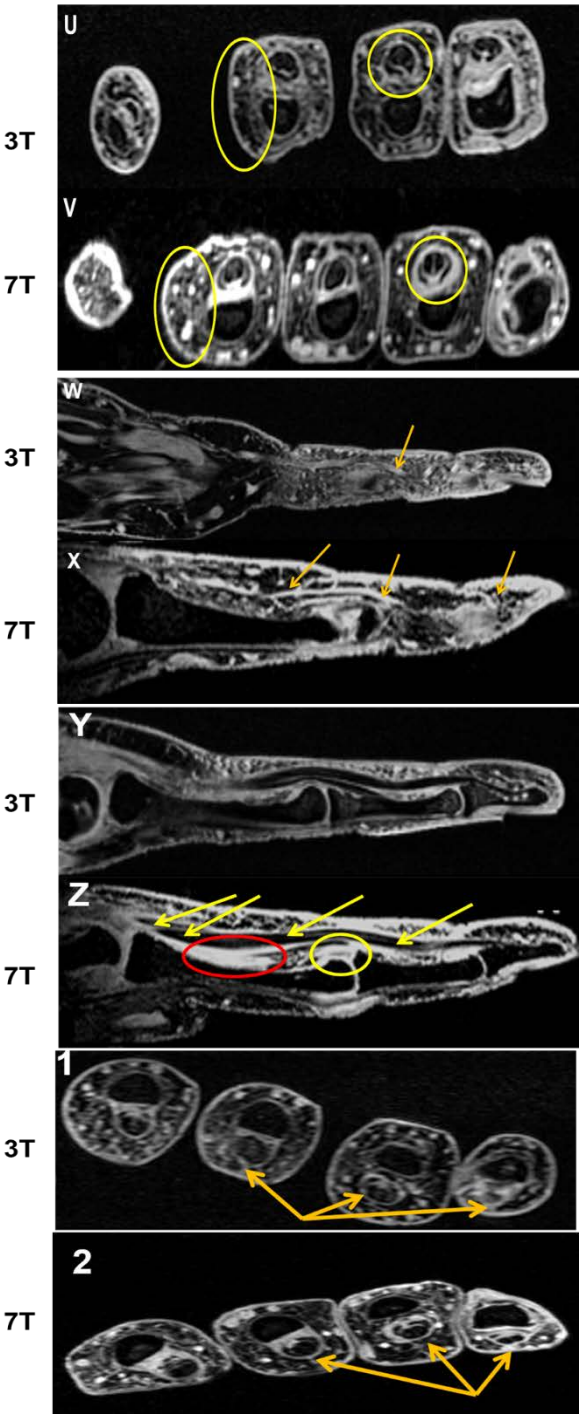

Figure 5.18: 3T vs 7T T1VIBE imaging of double-amputee transplant patient data.

5.2.4 CONCLUSION

This study shows the potential of using UHF MRI in post-transplant evaluation after UET and potentially in hand surgery practice, including in the diagnosis and interpretation of scaphoid fractures, avascular necrosis, carpal dislocations, triangular cartilage tears, connective tissue disorders, and other micro-vascular disease conditions.

6.0 CONCLUSION AND FUTURE WORK

6.1 SUMMARY AND CONTRIBUTION

6.1.1 Development of multi-channel transmit only whole body coil

A newly in-house built thirty-two channel Tx coil with parametric coupling design approach was developed to target and excite the nuclei utilizing the B_1^+ field in a circularly polarized arrangement for whole body imaging at 7T while keeping acceptable SAR limits as per FDA guidelines. This study presents a numerically developed RF Tx array which was also evaluated experimentally at 7T MRI. This RF system was built without the Rx-only insert, thus SNR/contrast was compromised. Results from preliminary studies indicate that the presented RF Tx coil can generate CP mode in simulation as well as experimentally in the outlined body phantom images using the modular highly coupled multichannel transmit coil.

6.1.2 Evaluation and in-vivo imaging of whole body transmit and receive only coil

The combined thirty-two channel Tx – sixteen-channel Rx only coil was designed and developed. This configuration has increased SNR approximately 3 to 3.5 times using a

multichannel Rx-only array in conjunction with the Tx coil design as discussed earlier in Chapter 3 in detail. Also, the clinical feasibility of parallel imaging was shown by G-factor measurements, which also show that R=3, 4 and above affects image quality. The noise correlation matrix provides good isolation between all the Rx channels. The in-vivo images show excellent anatomical detail in the liver and abdomen where the Rx coil is located. The stomach region doesn't benefit from Rx as much as the liver because the Rx coil only covers a limited region, not the entire circumference. Thus, utilizing a thirty-two channel TTT Body coil at UHF shows excellent potential for whole body imaging at ultra-high field (7T) within acceptable SAR limits.

6.1.3 Development of a TEM transmit and receive only array for upper extremity application

This study presents the first successful demonstration of a homogeneous volume resonator in conjunction with an eight-channel Rx only array for a targeted field of view UHF upper extremity imaging. This RF system was optimized for the human forearm but can be utilized to image the hand, wrist, arm or even elbow in extension as there is no significant change in tuning properties. With a small filling factor, the use of combined Tx and Rx coil is ideal to detect the incoming signal with nearly homogeneous excitation [149-152]. The in-house built TEM volume resonator in conjunction with an eight-channel Rx only array was successfully evaluated at 7T to confirm the potential for next generation UHF imaging in upper extremity applications. In-vivo images and a nearly homogenous B_1^+ field (shown in simulation, and experiment) demonstrate excellent coverage over the desired anatomy of interest with high SNR and CNR, revealing exquisite structures like nerve branches and fascicles, vessel lumens and walls, and cartilage and

synovial fluid delineation with the precise detail and resolution required for various extremity diseases and pre and post-surgery applications. A wide variety of images with high spatial resolution, SNR, and CNR were achieved and compare favorably to those aquired at 3T.

6.1.4 In-vivo feasibility evaluation of 7T upper extremity RF coil and non-contrast enhanced neuro-vascular imaging

A customized 7T RF coil was built and compared with available extremity coils at 3T with similar dimensions and the same number of elements. High SNR and CNR were achieved at 7T, with image quality significantly exceeding that at 3T, most especially in the HR protocol. Additionally, it shows that homogenous excitation (a typical hurdle for 7T imaging) is quite possible for the forearm with coverage that extends from wrist to elbow. T1W VIBE images at 7T have less overall noise when compared to the 3T images as the conspicuity of small vessels is superior. T2W DESS imaging shows improvements in nerve signal and better contrast between muscle planes at 7T when compared to 3T, with visualization of finer osseous trabecular detail. Moreover, there is greater contrast and delineation of cortical bone and improved detection of small vessel detail at 7T. Such resolution is clearly not available when utilizing 3T. Extended coverage (forearm, elbow and wrist) and exquisite image quality utilizing optimized pulse sequences (T1W VIBE, T2W DESS, DTI and TOF) in conjunction with custom-designed RF coil demonstrate the potential of 7T imaging for upper extremity applications.

6.2 FUTURE WORK

The TTT coil [26] presented here is a distinctive design to be used with 7T UHF body imaging in combination with a decoupled Rx-only-insert to reduce noise to provide excellent SNR [106]. This TTT design has never been applied in body imaging before. Few research groups have published work on RF shimming in different parts of the human body [12-15, 17, 19, 246]. The complex interaction (loading) between the biological tissue and the coil has been problematic due to the variation in electromagnetic properties as well as geometrical properties [37-39, 42, 43]. Future work will implement RF shimming techniques reliably. The transmission field (B_1^+) should be correctly measured from the ROI being imaged every time, which is unfeasible and time consuming [25]. The TTT RF coil is inherently highly coupled (higher RF transmission properties associated with highly coupled coils), which in turn enables it to negate the aforementioned loading effects (ultra-high field electromagnetic effects), and that helps overcome the loading dependency [20, 25, 26] which in turn will help in implementing circularly polarized B_1^+ field reliably without the need for frequent measurement of transmission field (B_1^+).

In the case of extremity coil, we focused on forearm/elbow imaging. Also, due to the small electrical size of the load, the TEM resonator was almost load insensitive and the Rx array didn't affect the tuning significantly, so the Rx coil was replaceable. In cases of high density design (ex: twelve or sixteen channels) being used instead of eight channels without affecting Tx performance SNR would be boosted even further, or a different geometrical/structural Rx design could be used (i.e. future work includes various geometrical design for extremity (wrist, finger joints, hand)

imaging). Furthermore, the TEM's B_1^+ field homogeneity could be further improved by adding more strut elements. In addition to developing hardware, we plan to concentrate our efforts on developing and applying optimized sequences to various clinical applications utilizing on-site and post-processing software to benefit from the advantages offered by 7T.

REFERENCES

1. Posin, J.P., et al., *Hydrogen Mr Imaging of the Head at 0.35-T and 0.7-T - Effects of Magnetic-Field Strength.* Radiology, 1985. **157**(3): p. 679-683.

2. Bottomley, P.A., et al., *Anatomy and Metabolism of the Normal Human-Brain Studied by Magnetic-Resonance at 1.5 Tesla.* Radiology, 1984. **150**(2): p. 441-446.

3. Robitaille, P.M.L., A.M. Abduljalil, and A. Kangarlu, *Ultra high resolution imaging of the human head at 8 Tesla: 2K x 2K for Y2K.* Journal of Computer Assisted Tomography, 2000. **24**(1): p. 2-8.

4. Vaughan, T., et al., *9.4T human MRI: Preliminary results.* Magnetic Resonance in Medicine, 2006. **56**(6): p. 1274-1282.

5. P-M.L., R., et al., *Human Magnetic Resonance Imaging at Eight Tesla. .* NMR Biomed, 1998. **11**: p. 263-265.

6. Vaughan, J.T., et al., *7T vs. 4T: RF power, homogeneity, and signal-to-noise comparison in head images.* Magnetic Resonance in Medicine, 2001. **46**(1): p. 24-30.

7. *Translate 7T research power into clinical care*, Siemens, Editor. 2015, Siemens Healthcare Headquarters: Siemens Healthcare GmbH, Henkestraße 127, 91052 Erlangen, Germany.

8. Robitaille , P.M. and L. Berliner, *Ultra High Field Magnetic Resonance Imaging: 26 (Biological Magnetic Resonance)*. 2007: Springer US.

9. Haacke, E.M., et al., *Susceptibility-Weighted Imaging: Technical Aspects and Clinical Applications, Part 1.* American Journal of Neuroradiology, 2009. **30**(1): p. 19-30.

10. Jacobs, M.A., T.S. Ibrahim, and R. Ouwerkerk, *AAPM/RSNA physics tutorial for residents - MR imaging: Brief overview and emerging applications.* Radiographics, 2007. **27**(4): p. 1213-U65.

11. Smith-Bindman, R., D.L. Miglioretti, and E.B. Larson, *Rising Use Of Diagnostic Medical Imaging In A Large Integrated Health System.* Health Affairs, 2008. **27**(6): p. 1491-1502.

12. Vaughan, J.T., et al., *Whole-body imaging at 7T: preliminary results.* Magn Reson Med, 2009. **61**(1): p. 244-8.

13. Metzger, G.J., et al., *Performance of External and Internal Coil Configurations for Prostate Investigations at 7 T.* Magnetic Resonance in Medicine, 2010. **64**(6): p. 1625-1639.

14. Snyder, C.J., et al., *Initial Results of Cardiac Imaging at 7 Tesla.* Magnetic Resonance in Medicine, 2009. **61**(3): p. 517-524.

15. Vossen, M., *A radiofrequency coil configuration for imaging the human vertebral column at 7 T.* Journal of Magnetic Resonance Imaging, 2011: p. 291-297.

16. Metzger, G.J., et al. *Initial Experiences with Non-Contrast Enhanced Renal Angiography at 7.0 Tesla*. in *International Society of Magnetic resonance in Medicine*. 2010. Stockholm. Sweden

17. Pang, Y., et al., *Numerical Analysis of Human Sample Effect on RF Penetration and Liver MR Imaging at Ultrahigh Field.* Concepts in Magnetic Resonance Part B-Magnetic Resonance Engineering, 2011. **39B**(4): p. 206-216.

18. Regatte, R.R. and M.E. Schweitzer, *Ultra-high-field MRI of the musculoskeletal system at 7.0T.* Journal of Magnetic Resonance Imaging, 2007. **25**(2): p. 262-269.

19. Umutlu, L., et al., *Renal imaging at 7 Tesla: preliminary results.* European Radiology, 2011. **21**(4): p. 841-849.

20. Ibrahim, T. *5 Decoupled Sets of Coupled Coils: An 8-20 Channel Subject-Insensitive Array for 7T Applications.* in *ISMRM*. 2010.

21. Vaughan, J.T., et al., *7T vs. 4T: RF power, homogeneity, and signal-to-noise comparison in head images.* Magnetic Resonance in Medicine, 2001. **46**(1): p. 24-30.

22. Zhao, Y., et al., *Dual optimization method of radiofrequency and quasistatic field simulations for reduction of eddy currents generated on 7T radiofrequency coil shielding.* Magn Reson Med, 2014.

23. Brown, R., et al., *Design of a nested eight-channel sodium and four-channel proton coil for 7T knee imaging.* Magnetic Resonance in Medicine, 2013. **70**(1): p. 259-268.

24. Pakin, S.K., et al., *Ultra-high-field MRI of knee joint at 7.0T: Preliminary experience.* Academic Radiology, 2006. **13**(9): p. 1135-1142.

25. Ibrahim, T. *In-Vivo RF Power-Controlled B1 Shimming with Tx/Rx array and with Tx array Combined Rx only coil without B1 measurements.* . in *ISMRM*. 2007.

26. Ibrahim, T. *Tic-Tac-Toe: Highly-Coupled, Load Insensitive Tx/Rx Array and a Quadrature Coil without Lumped Capacitors.* in *ISMRM*. 2008.

27. Zhao, Y., et al., *Dual optimization method of radiofrequency and quasistatic field simulations for reduction of eddy currents generated on 7T radiofrequency coil shielding.* Magn Reson Med, 2014.

28. Garcia, J. and S. Bianchi, *Diagnostic imaging of tumors of the hand and wrist.* European Radiology, 2001. **11**(8): p. 1470-1482.

29. Stafford, R.J., *High Field MRI: Technology, Applications, Safety, and Limitations.* AAPM, 2004. **32**(6).

30. Hoult, D.I. and R.E. Richards, *The signal to noise ratio of the nuclear magnetic resonance experiment.* J. Magn. Reson., 1976. **24**: p. 71-85.

31. Gruetter, R., et al., *Resolution improvements in in vivo 1h nmr spectra with increased magnetic field strength.* J. Magn. Reson., 1998. **135**: p. 260-264.

32. Abduljalil, A.M. and P.-M.L. Robitaille, *Macroscopic susceptibility in ultra high field MRI.* J. Comp. Assist. Tomogr., 1999(23): p. 832–841, .

33. Abduljalil, A.M., et al., *Macroscopic susceptibility in ultra high field MRI II J Comp Assist Tomogr.* J. Comp. Assist. Tomogr., 1999. **23**: p. 842–844.

34. Gati, J.S., et al., *Experimental determination of the BOLD field strength dependence in vessels and tissue.* Magn. Reson. Med., 1997. **38**: p. 296–302.

35. Bottomley, P.A. and E.R. Andrew, *Rf Magnetic-Field Penetration, Phase-Shift and Power Dissipation in Biological Tissue - Implications for Nmr Imaging.* Physics in Medicine and Biology, 1978. **23**(4): p. 630-643.

36. Roschmann, P., *Radiofrequency Penetration and Absorption in the Human-Body - Limitations to High-Field Whole-Body Nuclear-Magnetic-Resonance Imaging.* Medical Physics, 1987. **14**(6): p. 922-931.

37. Ibrahim, T.S., Y.K. Hue, and L. Tang, *Understanding and manipulating the RF fields at high field MRI.* Nmr in Biomedicine, 2009. **22**(9): p. 927-936.

38. Ibrahim, T.S., *Analytical approach to the MR signal.* Magnetic Resonance in Medicine, 2005. **54**(3): p. 677-682.

39. Collins, C.M., et al., *Combination of optimized transmit arrays and some receive array reconstruction methods can yield homogeneous images at very high frequencies.* Magnetic Resonance in Medicine, 2005. **54**(6): p. 1327-1332.

40. Tang, L., Y.K. Hue, and T.S. Ibrahim, *Studies of RF Shimming Techniques with Minimization of RF Power Deposition and Their Associated Temperature Changes.* Concepts in Magnetic Resonance Part B-Magnetic Resonance Engineering, 2011. **39B**(1): p. 11-25.

41. Ibrahim, T.S. and L. Tang, *Insight into RF power requirements and B-1 field homogeneity for human MRI via rigorous FDTD approach.* Journal of Magnetic Resonance Imaging, 2007. **25**(6): p. 1235-1247.

42. Schick, F., *Whole-body MRI at high field: technical limits and clinical potential.* European Radiology, 2005. **15**(5): p. 946-959.

43. Doty, F.D., et al., *Radio frequency coil technology for small-animal MRI.* Nmr in Biomedicine, 2007. **20**(3): p. 304-325.

44. Vernickel, P., et al., *Eight-channel transmit/receive body MRI coil at 3T.* Magnetic Resonance in Medicine, 2007. **58**(2): p. 381-389.

45. Pound, R.V., *From radar to nuclear magnetic resonance.* Reviews of Modern Physics, 1999. **71**(2): p. S54-S58.

46. Purcell, E.M., H.C. Torrey, and R.V. Pound, *Resonance Absorption by Nuclear Magnetic Moments in a Solid.* Physical Review, 1946. **69**(1-2): p. 37-38.

47. Ginsberg, D.M. and M.J. Melchner, *Optimum geometry of saddle shaped coils for generating a uniform magnetic field.* Rev. Sci. Instrum.,, 1970. **44**: p. 122–123.

48. Schneider, H.J. and P. Dullenkopf, *Slotted tube resonator: A new NMR probe head at high observing frequencies.* Rev. Sci. Instrum, 1977. **48**: p. 68-73.

49. Alderman, D.W. and D.M. Grant, *An efficient decoupler coil design which reduces heating in conductive samples in superconducting spectrometers.* Magn. Reson.,, 1979. **36**: p. 447–451.

50. Hayes, E.C., et al., *An efficient highly homogeneous radiofrequency coil for whole-body NMR imaging at 1.5 T.* J. Magn. Reson, 1985. **63**: p. 622-628.

51. Leifer, M.C., *Theory of the quadrature elliptic birdcage coil.* Magn Reson Med, 1997. **38**(5): p. 726-32.

52. Bobroff, S. and M.J. McCarthy, *Variations on the slotted-tube resonator: rectangular and elliptical coils.* Magn Reson Imaging, 1999. **17**(5): p. 783-9.

53. Hayes, E.C., *An endcap birdcage resonator for quadrature head imaging.* Magn. Reson. Med., 1986. **5**: p. 39–40.

54. Ballon, D., et al., *A 64 MHz Halfbirdcage resonator for clinical imaging.* Journal of Magnetic Resonance 1990. **90**(1): p. 131-140.

55. Foo, T.K., C.E. Hayes, and Y. Kang, *Reduction of RF penetration effects in high field imaging.* Magn. Reson. Med., 1992. **23**: p. 287-301.

56. Roschmann, P., *HIGH-FREQUENCY COIL SYSTEM FOR A MAGNETIC RESONANCE IMAGING APPARATUS U.S.1988 Nov. 3, 1986.* 1986, U.S. Philips Corporation, Tarrytown, N.Y. : US.

57. Bridges, J.F., *Cavity resonator with improved magnetic field uniformity for high frequency ooperation and reduced dielectric heating in NMR imaging devices*, U.S.P.a.T. Office, Editor. 1988: US.

58. Vaughan, J.T., et al., *Detunable transverse electromagnetic (TEM) volume coil for high-field NMR.* Magnetic Resonance in Medicine, 2002. **47**(5): p. 990-1000.

59. Bogdanov, G. and R. Ludwig, *Coupled microstrip line transverse electromagnetic resonator model for high-field magnetic resonance imaging.* Magnetic Resonance in Medicine, 2002. **47**(3): p. 579-593.

60. Vaughan, J.T., et al., *High-Frequency Volume Coils for Clinical Nmr Imaging and Spectroscopy.* Magnetic Resonance in Medicine, 1994. **32**(2): p. 206-218.

61. Morich, M.A., et al., *Short element TEM coil for ultra-high field MR*. 2009, Google Patents.

62. Adriany, G. *Shielded Surface Coils and Halfvolume Cavity Resonators for Imaging and Spectroscopy Applications at 7 Tesla.* . in *8th Annual meting of International Society of magnetic Resonance in Medicine.* 2000. Denver, CO.

63. Ong, K.C., *Radiofrequency shielding of surface coils at 4.0 T. .* J Magn Reson Imaging, 1995. **5**(6): p. 773-7.

64. Keltner, J.R., *Electromagnetic fields of surface coil in vivo NMR at high frequencies. .* Magn Reson Med,, 1991. **22**(2): p. 467-80.

65. Adriany, G., et al., *Transmit and receive transmission line arrays for 7 Tesla parallel imaging.* Magn Reson Med, 2005. **53**(2): p. 434-45.

66. Wang, C. and G.X. Shen, *B1 field, SAR, and SNR comparisons for birdcage, TEM, and microstrip coils at 7T..* J Magn Reson Imaging, 2006: p. 439-43.

67. Li, M., et al., *In vivo sensitivity estimation and imaging acceleration with rotating RF coil arrays at 7 Tesla.* J Magn Reson, 2015. **252**: p. 29-40.

68. Raaijmakers, A.J.E., et al., *The Fractionated Dipole Antenna: A New Antenna for Body Imaging at 7 Tesla.* Magn Reson Med, 2015. **75**(3): p. 1366-1374.

69. Raaijmakers, A.J.E., P.R. Luijtena, and C.A.T. van den Berg, *Dipole antennas for ultrahigh-field body imaging: a comparison with loop coils.* NMR Biomed., 2016. **29**(9): p. 1122-30.

70. Zhang, B., et al., *Whole Body Traveling Wave Magnetic Resonance Imaging at High Field Strength: Homogeneity, Efficiency, and Energy Deposition as Compared With Traditional Excitation Mechanisms. .* Magnetic Resonance in Medicine, 2012. **67**: p. 1183–1193.

71. Lynch, D.R., K.D. Paulsen, and J.W. Strohbehn, *Finite element solution of maxwell's equations for hyperthermia treatment planning.* J. Comp. Physics, 1990. **58**: p. 246–269.

72. Wang, C.Q. and O.P. Gandhi, *Numerical simulation of annular phased arrays for anatomically based models using the FDTD method.* IEEE Trans. Microwave Theory Tech, 1989. **37**: p. 118-126.

73. Chen, J.Y. and O.P. Gandhi, *Numerical Simulation of annular-phased arrays of dipoles for hyperthermia of deep-seated tumors.* IEEE Trans. Biomed. Eng., 1992. **39**(209-216).

74. Jansen, M.A. and Y. Rahmat-Samii, *EM interaction of handset antennas and a human in a personal communications.* Proc. IEEE, January 1996. **83**: p. 7-17.

75. Tinniswood, A.D., C.M. Furse, and O.P. Gandhi, *Computation of SAR distribution for two anatomically based models of human head using CAD files of commercial telephones and the parallelized FDTD code.* IEEE Trans. Antennas Propagation, January 1998. **AP-46**: p. 829-833.

76. Vetter, J., G. Ries, and A. Reichert, *A 4-Tesla superconducting whole-body magnet for MR imaging and spectroscopy.* IEEE Trans. Magnetics, 1988. **24**: p. 1285–1287,.

77. Langkowski, J.H., et al., *Pre-operative localized in vivo proton spectroscopy in cerebral tumors at 4 Tesla-first Results.* Magn. Reson. Imaging, 1989. **7**(547-555).

78. Robitaille, P.-M.L., et al., *Human magnetic resonance imaging at 8T.* NMR in Biomed, 1998. **11**: p. 263-265.

79. Ibrahim, T.S., et al., *Effect of RF coil excitation on field inhomogeneity at ultra high fields: a field optimized TEM resonator.* Magn. Reson. Imaging, 2001. **19**: p. 1339-1347.

80. Ibrahim, T.S., et al., *Application of finite difference time domain method for the design of birdcage RF head coils using multi-port excitations.* Magnetic Resonance Imaging, 2000. **18**(6): p. 733-742.

81. Ibrahim, T.S. *Optimized radiofrequency resonators for high field NMR clinical imaging. IEEE International Symposium on Antennas and Propagation*. in *IEEE*. 2000. Salt Lake City, Utah.

82. Han, Y. and S.M. Wright. *Analysis of RF penetration effects in MRI using finite-difference time-domain method*. in *12th Annual Meeting of the Society of Magnetic Resonance*. 1993. NY.

83. Taylor, H.C., M. Bur, and J.W. Hand, *Phy. Med. Biol.* Experimental verification of numerically predicted electric field distributions by a radio frequency coil,, 1997. **42**(1395-1402).

84. Jin, J.M., et al., *Computation of electromagnetic fields for high-frequency magnetic resonance imaging applications.* Phy. Med. Biol.,, 1996. **41**: p. 2719-2738.

85. Collins, C.M., S.L. Li, and M.B. Smith, *SAR and B1 field distributions in a heterogeneous human head model within a birdcage coil.* Magn. Reson. Med., 1998. **40**: p. 846-856.

86. Chen, J., Z.M. Feng, and J.M. Jin, *Numerical simulation of SAR and B-1-field inhomogeneity of shielded RF coils loaded with the human head (vol 45, pg 650, 1998).* Ieee Transactions on Biomedical Engineering, 1998. **45**(7): p. 949-949.

87. Jin, J.M. and J. Chen, *On the SAR and field inhomogeneity of birdcage coils loaded with human head.* Magn. Reson. Med., 1997. **31**: p. 953–963.

88. Simunic, D., et al., *Spatial distribution of high-frequency electromagnetic energy in human head during MRI: numerical results and measurements.* IEEE Trans. Biomed. Eng.,, 1996. **43**: p. 88-94.

89. Ibrahim, T.S., et al. *Finite difference time domain simulations for high-field MRI*. in *6th Annual Meeting of the International Society of Magnetic Resonance in Medicine*. 1998. Sydney, Australia.

90. Ibrahim, T.S., et al., *Computational analysis of the high pass birdcage resonator: Finite difference time domain simulations for high-field MRI.* Magn. Reson. Imaging, 2000. **18**: p. 835-843.

91. Ibrahim, T.S., et al. *On the physical feasibility of achieving linear polarization at high-field: a study of the birdcage coil*. in *7th Annual Meeting of the International Society of Magnetic Resonance in Medicine*. May 1999. Philadelphia, Pennsylvania, USA.

92. Yee, K.S., *Numerical Solution of Initial Boundary Value Problems Involving Maxwells Equations in Isotropic Media.* Ieee Transactions on Antennas and Propagation, 1966. **Ap14**(3): p. 302.

93. Nehrbass, J.W., *Advances in finite differences methods for electromagnetics modelling*, in *Electrical Engineering*. 1996, Ohio State University, OH.

94. Chia, T.T., *Application of FDTD in hybrid methods for EM scattering analysis of cavity with complex terminations*, in *Electrical Engineering*. 1994, Ohio State University, OH.

95. Balanis, C.A., *Advanced engineering electromagnetics.* 1989: John Wiley and Sons.

96. Ibrahim, T.S., *Modelling ground penetration radar dipole antenna using finite difference time domain*, in *Electrical Engineering*. 1996, Ohio State University.

97. Christ, A., et al., *The Virtual Family-development of surface-based anatomical models of two adults and two children for dosimetric simulations.* Physics in Medicine and Biology, 2010. **55**(2): p. N23-N38.

98. Society, A.c., *American Cancer Society: Cancer Facts and Figures 2017*. 2017: Atlanta, GA.

99. Howlader, N., *SEER Cancer Statistics Review, 1975-2011*. 2014, National Cancer Institute. : Bethesda, MD.

100. Wu, X., et al., *Comparison of radiofrequency body coils for MRI at 3 Tesla: a simulation study using parallel transmission on various anatomical targets* NMR Biomed. , Oct 2015. **28**(10): p. 1332–1344.

101. Tian, J., et al., *Searching for the Optimal Body Coil Design for 3T MRI.* Proc. Intl. Soc. Mag. Reson. Med. , 2013. **21**: p. 2746.

102. Abraham, R. and T.S. Ibrahim, *Proposed Radiofrequency Phased-Array Excitation Scheme for Homogenous and Localized 7-Tesla hole-Body Imaging Based on*

Full-Wave Numerical Simulations. Magnetic Resonance in Medicine 2007. **57**: p. 235–242.

103. Orzada, S., et al., *7 Tesla Abdominal Imaging using TIAMO.* Proc. Intl. Soc. Mag. Reson. Med. , 2011. **19**: p. 594.

104. Hezel, F., et al., *Initial Results of Abdominal MRI at 7T Using a 16 channel Transmit/Receive Coil. .* Proc. Intl. Soc. Mag. Reson. Med. , 2011. **19**: p. 595.

105. Snyder, C.J., et al., *Comparison Between Eight- and Sixteen-Channel TEM Transceive Arrays for Body Imaging at 7 T.* Magnetic Resonance in Medicine, 2012. **67**(4): p. 954-964.

106. Roemer, P.B., et al., *The Nmr Phased-Array.* Magnetic Resonance in Medicine, 1990. **16**(2): p. 192-225.

107. T. S. Ibrahim, Y.Z., T. Zhao, N. Krishnamurthy, S. Wood, S. Raval and H. Kim. *20-to-8 Channel Tx Array with 32-channel Adjustable Receive-Only Insert for 7T Head Imaging*. in *The 21st International Society of Magnetic Resonance in Medicine Annual Meeting*. 2013. Salt Lake City, Utah.

108. Y. Zhao, N.K., S. Wood, T. Zhao, S. B. Raval, and T. S. Ibrahim. *3D Eigenmodes Optimizations for 3D Imaging at 7T*. in *The 23nd International Society of Magnetic Resonance in Medicine Annual Meeting*. 2015 Toronto, Canada.

109. Y. Zhao, T.Z., N. Krishnamurthy and T. S. Ibrahim. *On the E-Field Construction/Deconstruction and B1+ Efficiency/Homogeneity with Transmit Array Eigen Modes*. in *The 22nd International Society of Magnetic Resonance in Medicine Annual Meeting*. 2014. Milan, Italy.

110. Tang L, Hue YK, and Ibrahim TS, *Studies of RF Shimming Techniques with Minimization of RF Power Deposition and Their Associated Temperature Changes.* Concepts in Magnetic Resonance Part B-Magnetic Resonance Engineering, 2011. **39B**(1): p. 11-25.

111. Collins CM, et al., *Combination of optimized transmit arrays and some receive array reconstruction methods can yield homogeneous images at very high frequencies.* Magnetic Resonance in Medicine, 2005. **54**(6): p. 1327-1332.

112. Ibrahim, T.S., et al., *Analysis of B1 field profiles and SAR values for multi-strut transverse electromagnetic RF coils in high field MRI applications.* Phys Med Biol, 2001. **46**(10): p. 2545-55.

113. Ibrahim, T.S., et al., *Effect of RF coil excitation on field inhomogeneity at ultra high fields: a field optimized TEM resonator.* Magn Reson Imaging, 2001. **19**(10): p. 1339-47.

114. Berenger, J.P., *Three-dimensional perfectly matched layer for the absorption of electromagnetic waves.* Journal of Computational Physics, 1996. **127**(2): p. 363-379.

115. Berenger, J.P., *A Perfectly Matched Layer for the Absorption of Electromagnetic-Waves.* Journal of Computational Physics, 1994. **114**(2): p. 185-200.

116. Christ, A., et al., *The Virtual Family--development of surface-based anatomical models of two adults and two children for dosimetric simulations.* Phys Med Biol, 2010. **55**(2): p. N23-38.

117. MD, H., *Radiative losses of a birdcage resonator.* Magn Reson Med, 1993. **29**: p. 713-16.

118. Roschmann, P., *High-frequency coil system for a magnetic resonance imaging apparatus*. 1986, U.S. Philips Corporation.

119. Fautz, H., et al., *Extending the sensitivity range for transmit array B1 mapping using relative B1 maps.* Proc. Intl. Soc. Mag. Reson. Med., 2012. **20**: p. 3363.

120. NITRC, *MRIcron*. Aug 19, 2008, Neuroimaging Informatics Tools and Resources Clearinghouse (NITRC) University of South Carolina.

121. Schneider, C.A., W.S. Rasband, and K.W. Eliceiri, *NIH Image to ImageJ: 25 years of image analysis.* Nature methods 2012. **9**(7): p. 671-675.

122. Dieringer, M.A., et al. *4CH TX/RX SURFACE COIL FOR 7T: DESIGN, OPTIMIZATION AND APPLICATION FOR CARDIAC FUNCTION IMAGING*. in *ISMRM*. 2010. Stockholmsmässan AB: ISMRM.

123. Vaughan, J.T., et al., *7 T Whole Body Imaging: Preliminary Results.* Magn Reson Med, 2009. **61**(1): p. 244-248.

124. Alon, L., *Radio'Frequency Energy Quantification in Magnetic Resonance Imaging*, in *Basic Medical Science*. 2014, NYU: NYU. p. 401.

125. Du, R., et al., *Magnetic resonance neurography for the evaluation of peripheral nerve, brachial plexus, and nerve root disorders Clinical article.* Journal of Neurosurgery, 2010. **112**(2): p. 362-371.

126. Cox, F.M., et al., *Magnetic resonance imaging of skeletal muscles in sporadic inclusion body myositis.* Rheumatology, 2011. **50**(6): p. 1153-1161.

127. Kuo, G.P. and J.A. Carrino, *Skeletal muscle imaging and inflammatory myopathies.* Curr Opin Rheumatol, 2007. **19**(6): p. 530-5.

128. Miller, T.T. and W.R. Reinus, *Nerve Entrapment Syndromes of the Elbow, Forearm, and Wrist.* American Journal of Roentgenology, 2010. **195**(3): p. 585-594.

129. Steinbach, L.S. and D.K. Smith, *MRI of the wrist.* Clin Imaging, 2000. **24**(5): p. 298-322.

130. Shindle, M.K., et al., *Magnetic resonance imaging of cartilage in the athlete: Current techniques and spectrum of disease.* Journal of Bone and Joint Surgery-American Volume, 2006. **88A**: p. 27-46.

131. Eshed, I., et al., *MRI of enthesitis of the appendicular skeleton in spondyloarthritis.* Annals of the Rheumatic Diseases, 2007. **66**(12): p. 1553-1559.

132. Aagaard, B.D., et al., *High-resolution Magnetic Resonance Imaging Is a Noninvasive Method of Observing Injury and Recovery in the Peripheral Nervous System.* Neurosurgery, 2003. **53**(1): p. 199-204.

133. Takagia, T., M. Nakamuraa, and M. Yamadae, *Visualization of peripheral nerve degeneration and regeneration: Monitoring with diffusion tensor tractography.* NeuroImage, 2009. **44**(3): p. 884-892.

134. Robinson, S.P., et al., *Tumor Vascular Architecture and Function Evaluated by Non-Invasive Susceptibility MRI Methods and Immunohistochemistry.* JMRI, 2003. **17**: p. 445-54.

135. Wiggins, G.C., et al., *Eight-channel phased array coil and detunable TEM volume coil for 7 T brain imaging.* Magnetic Resonance in Medicine, 2005. **54**(1): p. 235-240.

136. Avdievich, N.I., et al., *7T Head Volume Coils: Improvements for Rostral Brain Imaging.* Journal of Magnetic Resonance Imaging, 2009. **29**(2): p. 461-465.

137. Juras, V., et al., *Comparison of 3 T and 7 T MRI clinical sequences for ankle imaging.* European Journal of Radiology, 2012. **81**(8): p. 1846-1850.

138. Pakin, S.K., et al., *Ultra-high-field MRI of knee joint at 7.0T: Preliminary experience.* Academic Radiology, 2006. **13**(9): p. 1135-1142.

139. Moon, C.H., et al., *Quantitative Na-23 MRI of Human Knee Cartilage Using Dual-Tuned H-1/Na-23 Transceiver Array Radiofrequency Coil at 7 Tesla.* Journal of Magnetic Resonance Imaging, 2013. **38**(5): p. 1063-1072.

140. Avdievich, N.I. and H.P. Hetherington, *High-field head radiofrequency volume coils using transverse electromagnetic (TEM) and phased array technologies.* Nmr in Biomedicine, 2009. **22**(9): p. 960-974.

141. Roemer, P.B., et al., *The Nmr Phased-Array.* Magnetic Resonance in Medicine, 1990. **16**(2): p. 192-225.

142. Ibrahim, T.S., et al., *Electromagnetic Perspective on the Operation of RF Coils at 1.5–11.7 Tesla.* MRM, 2005. **54**: p. 683-690.

143. Taflove, A. and S.C. Hageness, *Computational electrodynamics: the finite-difference time-domain method.* 3rd Edition ed. 2005, Boston: Artech House.

144. Christ, A., et al., *The Virtual Family-development of surface-based anatomical models of two adults and two children for dosimetric simulations.* Physics in Medicine and Biology, 2010. **55**(2): p. N23-N38.

145. S., I.T., *A numerical analysis of radio-frequency power requirements in magnetic resonance imaging experiment.* IEEE Trans Microwave Theory Tech, 2004. **52**(8): p. 1999-2003.

146. Food and Drug Administration, U.S., *Guidance for industry and FDA staff: criteria for significant risk investigations of magnetic resonance diagnostic devices.* June, 2014, U.S. Department of Health and Human Services: MD.

147. Commission, I.E., *Medical Electrical Equipment - Part 2-33:Particular requirements for the basic safety and essential performence of magnetic resonance equipment for medical diagnosis, in IEC 60601-2-33. 2010*. 2010: Geneva.

148. Yeh, F., *DSI Studio*. 2010, Carnegie Mellon University: Department of Psychology,CMU,Pittsburgh,PA.

149. Boskamp, E.B., *Improved Surface Coil Imaging in Mr - Decoupling of the Excitation and Receiver Coils.* Radiology, 1985. **157**(2): p. 449-452.

150. Edelstein, W.A., C.J. Hardy, and O.M. Mueller, *Electronic Decoupling of Surface-Coil Receivers for Nmr Imaging and Spectroscopy.* Journal of Magnetic Resonance, 1986. **67**(1): p. 156-161.

151. Barberi, E.A., et al., *A transmit-only/receive-only (TORO) RF system for high-field MRI/MRS applications.* Magnetic Resonance in Medicine, 2000. **43**(2): p. 284-289.

152. Chen, C.N. and D.I. Hoult, *Biomedical Magnetic Resonance Technology.* 1st edition ed. 1989, Bristol, NewYork: CRC Press.

153. Kraff, O., et al., *An eight-channel transmit/receive multipurpose coil for musculoskeletal MR imaging at 7 T.* Medical Physics, 2010. **37**(12): p. 6368-6376.

154. Raghuraman, S., et al., *12-channel receive array with a volume transmit coil for hand/wrist imaging at 7 T.* Journal of Magnetic Resonance Imaging, 2013. **38**(1): p. 238-244.

155. Krishnamurthy, N., T. Zhao, and T.S. Ibrahim, *Effects of receive-only inserts on specific absorption rate, B1 (+) field, and Tx coil performance.* Journal of magnetic resonance imaging, 2014. **39**(2): p. 475-84.

156. Pradhan, S., et al., *Comparison of single voxel brain MRS AT 3T and 7T using 32-channel head coils.* Magnetic resonance imaging, 2015.

157. Pinkerton, R.G., E.A. Barberi, and R.S. Menon, *Noise properties of a NMR transceiver coil array.* Journal of Magnetic Resonance, 2004. **171**(1): p. 151-156.

158. Thawait, S.K., et al., *Peripheral Nerve Surgery: The Role of High-Resolution MR Neurography.* American Journal of Neuroradiology, 2012. **33**(2): p. 203-210.

159. Obusez, E.C., et al., *High-resolution MRI vessel wall imaging: spatial and temporal patterns of reversible cerebral vasoconstriction syndrome and central nervous system vasculitis.* AJNR, 2014. **35**: p. 1527 - 1532.

160. G., P.M., et al., *CNS vasculitis in autoimmune disease: MR imaging findings and correlation with angiography.* AJNR, 1999. **20**: p. 75-85.

161. Van der Kolk, A.G., et al., *Clinical applications of 7T MRI in the brain. .* Eur J Rad, 2013. **82**: p. 708-718.

162. Chang, G., et al., *MRI of the Wrist at 7 Tesla using an 8 Channel Array Coil Combined with Parallel Imaging: Preliminary Results.* JMRI, 2010. **31**(3): p. 740-6.

163. Behr, B., et al., *MR imaging of the human hand and wrist at 7 T.* Skeletal Radiology, 2009. **38**: p. 911-917.

164. Bode, A.S., et al. *Feasibility of Non-contrast-enhanced Magnetic Resonance Angiography for Imaging Upper Extremity Vasculature Prior to Vascular Access Creation*. in *ECR*. 2011. European Society of Radiology.

165. Braidy, C., et al., *Unenhanced MR Angiography of Renal Arteries: 51 Patients.* Vascular and Interventional Radiology, 2012. **199**(5): p. W629-W637.

166. Sadikin, C., et al., *The Current Role of 1.5T Non-contrast 3D Time-of-flight Magnetic Resonance Angiography to Detect Intracranial Steno-occlusive Disease.* Elsevier & Formosan Medical Association, 2007. **106**(9): p. 691-699.

167. Koopmans, P.J., et al., *MR venography of the human brain using susceptibility weighted imaging at very high field strength.* Magnetic Resonance Materials in Physics, Biology and Medicine, 2008. **21**(1): p. 149-158.

168. Budde, J., et al., *Human Imaging at 9.4 T Using T-2*-, Phase-, and Susceptibility-Weighted Contrast.* Magnetic Resonance in Medicine, 2011. **65**(2): p. 544-550.

169. Masi, J.N., et al., *Cartilage MR imaging at 3.0 versus that at 1.5T: preliminary results in a porcine model.* Radiology, 2005. **236**(1): p. 140-50.

170. Vaughan, T.T., et al., *Whole-Body Imaging at 7T: Preliminary Results.* Magnetic Resonance in Medicine, 2009. **61**(1): p. 244-248.

171. Van de Moortele1, P.F., et al., *B1 destructive interferences and spatial phase patterns at 7 T with a head transceiver array coil.* Magnetic Resonance in Medicine, 2005. **54**(6): p. 1503-1518.

172. Bottomley, P.A. and E.R. Andrew, *RF magnetic field penetration, phase shift and power dissipation in biological tissue: implications for NMR imaging.* Physics in Medicine and Biology, 1978. **23**(4).

173. Jambawalikar, S., et al., *Diffusion tensor imaging of peripheral nerves.* Skeletal Radiol, 2010. **39**(11): p. 1073-9.

174. Zhang, W., et al., *High-resolution magnetic resonance angiography of digital arteries in SSc patients on 3 Tesla: preliminary study.* Rheumatology (Oxford), 2011. **50**(9): p. 1712-9.

175. Haims, A.H., et al., *MRI in the diagnosis of cartilage injury in the wrist.* AJR Am J Roentgenol, 2004. **182**(5): p. 1267-70.

176. Bencardino, J.T., *MR imaging of tendon lesions of the hand and wrist.* Magn Reson Imaging Clin N Am, 2004. **12**(2): p. 333-47, vii.

177. Sampath, S.C., S.C. Sampath, and M.A. Bredella, *Magnetic resonance imaging of the elbow: a structured approach.* Sports Health, 2013. **5**(1): p. 34-49.

178. Chhabra, A., et al., *High-resolution 3-T MR neurography of peroneal neuropathy.* Skeletal Radiology, 2012. **41**(3): p. 257-271.

179. Chhabra, A., et al., *MR Neurography of Neuromas Related to Nerve Injury and Entrapment with Surgical Correlation.* American Journal of Neuroradiology, 2010. **31**(8): p. 1363-1368.

180. Vogelius, E.S., W. Hanna, and M. Robbin, *Magnetic resonance imaging of the long bones of the upper extremity.* Magn Reson Imaging Clin N Am, 2011. **19**(3): p. 567-79.

181. Thakkar, R., et al., *3-T MR Imaging of Cartilage Using 3D Dual-Echo Steady State Sequences.* American Journal of Roentgenology, 2012. **198**(5).

182. Haacke, E.M., et al., *Susceptibility-weighted imaging: technical aspects and clinical applications, part 1.* AJNR Am J Neuroradiol, 2009. **30**(1): p. 19-30.

183. Basser, P.J. and D.K. Jones, *Diffusion-tensor MRI: theory, experimental design and data analysis - a technical review.* NMR Biomed, 2002. **15**(7-8): p. 456-67.

184. Mori, S. and J. Zhang, *Principles of diffusion tensor imaging and its applications to basic neuroscience research.* Neuron, 2006. **51**(5): p. 527-39.

185. Biomedical, R. *16 Channel Wrist Array @ 7T*. [Investigational Device under FDA and IEC Rules and Regulation] 2015 04/2013.

186. Aussenhofer, S.A. and A.G. Webb, *Design and evaluation of a detunable water-based quadrature HEM11 mode dielectric resonator as a new type of volume coil for high field MRI.* Magnetic Resonance in Medicine, 2012. **68**(4): p. 1325-1331.

187. Raval, S.B., et al., *RF System for Ultra-High Field Upper Extremity Imaging*, in *Plastic and Reconstructive Surgery*. 2015.

188. Raval, S.B., et al. *Upper extremity neural (peripheral) and vascular (non-contrast) imaging with UHF 7T MRI*. in *International Society of Magnetic Resosnance in Medicine (ISMRM)*. 2015. Toronto, Canada.

189. Raval, S.B., et al. *Ultrahigh field (7T) magnetic resonance imaging (MRI) after upper extremity allotransplantation*. in *International Society of Magnetic Resosnance in Medicine (ISMRM)*. 2015. Toronto, Canada.

190. Aagaard, B.D., et al., *High-resolution Magnetic Resonance Imaging Is a Noninvasive Method of Observing Injury and Recovery in the Peripheral Nervous System.* Neurosurgery, 2003. **53**(1): p. 199-204.

191. Bode, A.S., et al., *Feasibility of Non-contrast-enhanced Magnetic Resonance Angiography for Imaging Upper Extremity Vasculature Prior to Vascular Access Creation.* European Society for Vascular Surgery, 2012. **43**(1): p. 88-94.

192. Anzidei, M., et al., *Diagnostic accuracy of colour Doppler ultrasonography, CT angiography and blood-pool-enhanced MR angiography in assessing carotid stenosis: a comparative study with DSA in 170 patients. .* Radiol Med, Feb 2012. **117**(1): p. 54-71.

193. Yamada, H., et al., *Efficacy of Distortion Correction on Diffusion Imaging: Comparison of FSL Eddy and Eddy_Correct Using 30 and 60 Directions Diffusion Encoding.* PLoS One, 2014. **9**(11).

194. Smith, S.M., et al., *Advances in functional and structural MR image analysis and implementation as FSL.* Neuroimage, 2004. **23**(S1): p. S208-219.

195. Basser, P.J., et al., *In vivo fiber tractography using DT-MRI data.* Magnetic Resonance in Medicine, 2000. **44**(4): p. 625-632.

196. Fernandez-Miranda, J.C., et al., *High-definition fiber tractography of the human brain: neuroanatomical validation and neurosurgical applications.* Neurosurgery, 2012. **71**(2): p. 430-53.

197. *Medical Image Processing, Analysis and Visualization(MIPAV)*. 2014, NIH: Bethasda, Maryland.

198. Hayes, E.C., et al., *Electronic Structure of a Cu(II)-Alkoxide Complex Modeling Intermediates in Copper-Catalyzed Alcohol Oxidations.* J Am Chem Soc, 2016. **138**(12): p. 4132-45.

199. Reichenbach, J.R., et al., *Small vessels in the human brain: MR venography with deoxyhemoglobin as an intrinsic contrast agent.* Radiology, 1997. **204**: p. 272-277.

200. Haider, C.R., et al., *High Temporal and Spatial Resolution 3D Time-Resolved Contrast-Enhanced MR Angiography of the Hands and Feet.* JMRI, 2011. **34**(1): p. 2-12.

201. Boskamp, E.B., *Improved surface coil imaging in MR: decoupling of the excitation and receiver coils.* Radiology, 1985. **157**(2): p. 449-452.

202. Barberi, E.A., et al., *A transmit-only/receive-only (TORO) RF system for high field MRI/MRS applications. .* Magn Reson Med, Feb 2000. **43**(2): p. 284–289. .

203. Raval, S.B., et al., *Ultra-high-field RF coil development for evaluating upper extremity imaging applications.* NMR in Biomedicine, 2016.

204. Vaughan, J.T., et al., *High-Frequency Volume Coils for Clinical Nmr Imaging and Spectroscopy.* Magnetic Resonance in Medicine, 1994. **32**(2): p. 206-218.

205. Behr, B., et al., *MR imaging of the human hand and wrist at 7 T.* Skeleton Radiology, 2009. **38**: p. 911-917.

206. Sadikin, C., et al., *The Current Role of 1.5T Non-contrast 3D Time-of-flight Magnetic Resonance Angiography to Detect Intracranial Steno-occlusive Disease.* Elsevier & Formosan Medical Association, 2007. **106**(9): p. 691-699.

207. Moore, K.R., J.S. Tsuruda, and A.T. Dailey, *The value of MR neurography for evaluating extraspinal neuropathic leg pain: a pictorial essay.* AJNR, 2001. **22**: p. 786-794.

208. Zhang, N., et al., *Non-Contrast Enhanced MR Angiography (NCE-MRA) of the Calf: A Direct Comparison between Flow-Sensitive Dephasing (FSD) Prepared Steady-State free Precession (SSFP) and Quiescent-Interval Single-Shot (QISS) in Patients with Diabetes* PLoS ONE, 2015. **10**(6).

209. Viallon, M., et al., *High-resolution and functional magnetic resonance imaging of the brachial plexus using an istotropic 3D STIR (short term inversion recovery) SPACE sequence and diffusion tensor imaging.* Eur Radiol, 2008. **18**(5): p. 1018-1023.

210. Vargas, M.I., et al., *New approaches in imaging of the brachial plexus.* Eur J Radiol, 2010. **74**: p. 403-410.

211. Chang, G., et al., *MRI of the Wrist at 7 Tesla using an 8 Channel Array Coil Combined with Parallel Imaging: Preliminary Results.* JMRI, 2010. **31**(3): p. 740-746.

212. Tipper, G., et al., *Detection and evaluation of intracranial aneurysms with 16-row multislice CT angiography. .* Clin Radiol, 2005. **60**(5): p. 565-572.

213. Karamessini, M.T., et al., *CT angiography with three-dimensional techniques for the early diagnosis of intracranial aneurysms: comparison with intraarterial DSA and the surgical findings. .* Eur J Radiol, Mar 2004. **49**(3): p. 212–223.

214. Hoh, B.L., et al., *Results of a prospective protocol of computed tomographic angiography in place of catheter angiography as the only diagnostic and pretreatment planning study for cerebral aneurysms by a combined neurovascular team.* Neurosurgery, 2004. **54**(6): p. 1329–1342; .

215. Förster, A., et al., *A comparison of CT/CT angiography and MRI/MR angiography for imaging of vertebrobasilar dolichoectasia. .* Clin Neuroradiol, Dec 2014. **24**(4): p. 347-53.

216. Todua, F.I., S.V. Chedia, and K. Nuralidze, *Computed tomography and magnetic resonance angiography of brain meningiomas.* , in *Georgian Med News* Dec 2013. p. 21-7.

217. Truwit, C.L., *CT angiography versus MR angiography in the evaluation of acute neurovascular disease. .* Radiology, 2007. **245**(2): p. 362-6.

218. Sakuma, H., *Coronary CT versus MR Angiography: The Role of MR Angiography. .* Radiology, Feb 2011. **258**(2): p. 340-9.

219. Vertinsky, A.T., et al., *Comparison of multidetector CT angiography and MR imaging of cervical artery dissection. .* AJNR Am J Neuroradiol., Oct 2008. **29**(9): p. 1753-60.

220. Lee WN, L.B., Pernot M, Tanter M *Ultrasound elastic tensor imaging: comparison with MR diffusion tensor imaging in the myocardium.* Phys Med Biol., 2012 Aug 21 **57**(16): p. 5075-95.

221. Hamdan, A., et al., *A prospective study for comparison of MR and CT imaging for detection of coronary artery stenosis.* JACC Cardiovasc Imaging, Jan 2011. **4**(1): p. 50-61.

222. Jazi, M.H., et al., *Comparing diagnostic techniques of magnetic resonance angiography (MRA) and doppler ultrasonography in determining severity of renal artery stenosis. .* ARYA Atheroscler, 2011. **7**(2): p. 58-62.

223. Bae, K.T., et al., *Dual-Echo Arteriovenography Imaging with 7 Tesla MR. .* J Magn Reson Imaging. , Jan 2010. **31**(1): p. 255–261.

224. Zhang CC, Y.Z., Giddabasappa A, Lappin PB, Painter CL, Zhang Q, Li G, Goodman J, Simmons B, Pascual B, Lee J, Levkoff T, Nichols T, and Xie Z. , *Comparison of dynamic contrast-enhanced MR, ultrasound and optical imaging modalities to evaluate the antiangiogenic effect of PF-03084014 and sunitinib. .* Cancer Med. , Jun 2014. **3** (3): p. 462–471.

225. Schmitter, S., et al., *Cerebral TOF Angiography at 7T: Impact of B1+ Shimming with a 16-Channel Transceiver Array. .* Magn Reson Med, 2014. **71**(3): p. 966-977.

226. Fischer, A., et al., *Initial evaluation of non-contrast enhanced magnetic resonance angiography in patients with peripheral arterial occlusive disease at 7T.* Investigative Radiology, 2014. **49**(5): p. 331-338.

227. Wrede, K.H., et al., *Non-enhanced magnetic resonance imaging of unruptured intracranial aneurysms at 7 Tesla: Comparison with digital subtraction angiography.* European Radiology, 2016.

228. Yang, Q., et al., *Contrastenhanced whole-heart coronary magnetic resonance angiography at 3.0-T: a comparative study with x-ray angiography in a single center. .* J Am Coll Cardiol, 2009. **54**(1): p. 69-76.

229. Nezafat, R. and W.J. Manning, *Coronary artery disease: high field strength coronary MRA— ready for prime time? .* Nat Rev Cardiol, 2009. **6**(11): p. 676 – 678.

230. Liu, X., et al., *Comparison of 3D free-breathing coronary MR angiography and 64-MDCT angiography for detection of coronary stenosis in patients with high calcium scores. .* AJR Am J Roentgenol 2007. **189**(6): p. 1326 – 1332

231. Kleinerman, R.A., *Cancer risks following diagnostic and therapeutic radiation exposure in children. .* Pediatr Radiol, 2006. **36**(2): p. 121-125.

232. Itagaki, M.W., R.D. Suh, and J.G. Goldin, *Cardiac CT research: exponential growth . .* Radiology, 2009. **252**(2): p. 468 - 476

233. Sibley, C.T. and D.A. Bluemke, ***Will 3.0-T make coronary magnetic resonance angiography competitive with computed tomography angiography?*** J Am Coll Cardiol, 2009. **54**(1): p. 77-78.

234. Kramer, C.M. and J. Narula, *Atherosclerotic plaque imaging: the last frontier for cardiac magnetic resonance.* JACC Cardiovasc Imaging 2009. **2**(7): p. 916-918.

235. Kang CK, P.C., Lee DS, Lee YB, Park CW, Kim YB, Cho ZH. , *Velocity measurement of microvessels using phase-contrast magnetic resonance angiography at 7 tesla MRI. .* Magn Reson Med, Apr 2016. **75**(4): p. 1640-6

236. Petruzzo, P., et al., *The International Registry on Hand and Composite Tissue Transplantation.* Transplantation, 2010. **90**(12): p. 1590-1594.

237. Ziegler-Graham, K., et al., *Estimating the prevalence of limb loss in the United States: 2005 to 2050.* Archives of Physical Medicine and Rehabilitation, 2008. **89**(3): p. 422-429.

238. Dougherty, A.L., et al., *Battlefield extremity injuries in Operation Iraqi Freedom.* Injury, 2009. **40**(7): p. 772-7.

239. Gorantla, V.S., et al., *Favoring the Risk-Benefit Balance for Upper Extremity Transplantation-The Pittsburgh Protocol.* Hand Clinics, 2011. **27**(4): p. 511.

240. Dong, Q., et al., *Entrapment neuropathies in the upper and lower limbs: anatomy and MRI features.* Radiol Res Pract, 2012. **2012**: p. 230679.

241. Nilsson, J., et al., *Magnetic resonance imaging of peripheral nerve tumours in the upper extremity.* Scand J Plast Reconstr Surg Hand Surg, 2009. **43**(3): p. 153-9.

242. Cox, F.M., et al., *Magnetic resonance imaging of skeletal muscles in sporadic inclusion body myositis.* Rheumatology (Oxford), 2011. **50**(6): p. 1153-61.

243. Wu, J.S. and M.G. Hochman, *Soft-tissue tumors and tumorlike lesions: a systematic imaging approach.* Radiology, 2009. **253**(2): p. 297-316.

244. Steinbach LS and Smith DK, *MRI of the wrist.* Clinical Imaging, 2000. **24**(5): p. 298-322.

245. Herrick, A.L., *Pathogenesis of Raynaud's phenomenon. .* Rheumatology (Oxford), 2005. **44**(5): p. 587-596.

246. Metzger, G.J. *Initial Experiences with Non-Contrast Enhanced Renal Angiography at 7.0 Tesla*. in *International Society of Magnetic resonance in Medicine*. 2010. Stockholm. Sweden